



저작자표시-비영리-변경금지 2.0 대한민국

이용자는 아래의 조건을 따르는 경우에 한하여 자유롭게

- 이 저작물을 복제, 배포, 전송, 전시, 공연 및 방송할 수 있습니다.

다음과 같은 조건을 따라야 합니다:



저작자표시. 귀하는 원 저작자를 표시하여야 합니다.



비영리. 귀하는 이 저작물을 영리 목적으로 이용할 수 없습니다.



변경금지. 귀하는 이 저작물을 개작, 변형 또는 가공할 수 없습니다.

- 귀하는, 이 저작물의 재이용이나 배포의 경우, 이 저작물에 적용된 이용허락조건을 명확하게 나타내어야 합니다.
- 저작권자로부터 별도의 허가를 받으면 이러한 조건들은 적용되지 않습니다.

저작권법에 따른 이용자의 권리와 책임은 위의 내용에 의하여 영향을 받지 않습니다.

이것은 [이용허락규약\(Legal Code\)](#)을 이해하기 쉽게 요약한 것입니다.

[Disclaimer](#)



Thesis for the Master of Science

Search for charged lepton flavor violation in
the top quark sector with hadronic tau final
state using CMS Run 2 data at $\sqrt{s} = 13$ TeV

Jongwon Lim

Graduate School of Hanyang University

August 2022

Thesis for the Master of Science

Search for charged lepton flavor violation in
the top quark sector with hadronic tau final
state using CMS Run 2 data at $\sqrt{s} = 13$ TeV

Thesis Supervisor: Tae Jeong Kim

A Thesis submitted to the graduate school of Hanyang
University in partial fulfillment of the requirements for
the degree of Master of Science

Jongwon Lim

August 2022

Department of Physics
Graduate School of Hanyang University

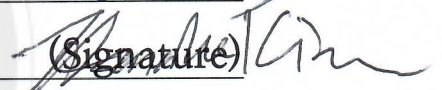
This thesis, written by Jongwon Lim,
has been approved as a thesis for the degree of
Master of Science.

August 2022

Committee Chairman: Byung Gu Cheon


(Signature)

Committee member: Hang Bae Kim


(Signature)

Committee member: Tae Jeong Kim


(Signature)

Graduate School of Hanyang University

Contents

Abstract	x
1 Introduction	1
1.1 The Standard Model	1
1.2 The CMS Detector	1
1.3 Lepton Flavor Violation	3
2 Lepton Flavor Violation in Top Quark using EFT	5
2.1 Effective Field Theory Interpretation	5
2.2 Generator Level Study	7
2.3 Signal Cross Sections	12
3 Samples	13
3.1 Data	13
3.2 MC Simulation Samples	15
3.3 Pileup	18
4 Object and Event Selections	19
4.1 Object Selections	19
4.1.1 Muon	19
4.1.2 Electron	20
4.1.3 Hadronic Tau	20
4.1.4 Jet	21
4.1.5 Missing Transverse Energy (MET)	22
4.2 Event Selections	23
5 Data and MC Comparison	24
5.1 Comparison for the Category 1 (ST LFV enriched region)	25
5.2 Comparison for the Category 2 (TT LFV enriched region)	32
5.3 Cutflow Table for Run2	39
6 Top Mass Reconstruction	42

7	Signal Extraction	46
7.1	Model Training	46
7.2	Evaluation	54
8	Systematic Uncertainties	54
8.1	Systematic Sources	54
8.2	Systematic Variations on DNN Output Distribution	56
9	Results	56
10	Conclusion	61
	References	62
	Appendix I. Control Plots for Run 2 data and MC	68
	Appendix II. DNN Train Results – Train Accuracy and Loss	93
	국문요지	95
	Acknowledgement	96
	Declaration of Ethical Conduct in Research	97
	연구윤리서약서	98

List of Figures

1	The Standard Model Particles with mass (upper in a box) and charge (lower in a box) properties of particles.	2
2	The CMS Detector and the sub-layers of the Detectors [7].	3
3	HFLAV average results of $R(D)$ and $R(D^*)$ measurement [14].	4
4	Feynman diagrams for the ST LFV (upper row) and $t\bar{t}$ LFV (lower row) processes.	7
5	Generator-level p_T (upper row) and η (lower row) distributions of a muon (left column) and tau (right column) from the LFV top decay.	8
6	Generator-level distributions of ΔR (left) and mass (right) reconstructed with a muon and a tau from LFV top decay.	9
7	Generator-level p_T (upper row) and η (lower row) distributions of a muon (left column) and tau (right column) from the LFV top decay.	9
8	Generator-level distributions of ΔR (left) and mass (right) reconstructed with a muon and tau from LFV top decay.	10
9	Generator-level p_T (upper row) and η (lower row) distributions of a muon (left column) and tau (right column) from LFV top interaction with vector-like operator.	11
10	Generator-level distributions of ΔR (left) and mass (right) reconstructed with a muon and a tau from LFV top interaction with vector-like operator.	11
11	Comparison of Pileup distributions for data and MC in run 16APV (upper left), run 16 (upper right), run 17 (lower left) and run 18 (lower right)	18
12	Data/MC comparison histograms in the category 1 after S2. ΔR (left) and mass (right) reconstructed with a muon and tau.	25
13	Data/MC comparison histograms in the category 1 after S3. p_T (left column) and η (right column) distributions for muon (upper row) and tau (lower row). . . .	26
14	Data/MC comparison histograms in the category 1 after S3. ΔR (left) and mass (right) distributions reconstructed with the muon and tau.	27
15	Data/MC comparison histograms in the category 1 for jet multiplicity distribution (left) after S3 and b-tagged jet multiplicity distribution (right) after S4. . . .	27

16	Data/MC comparison histograms in the category 1 after S4. p_T (upper row) and η (lower row) distributions of the leading (left column) and sub-leading jets (right column).	28
17	Data/MC comparison histograms in the category 1 after S5 (final). p_T (left column) and η (right column) distributions for muon (upper row) and tau (lower row).	29
18	Data/MC comparison histograms in the category 1 after S5 (final). ΔR (left) and mass (right) distributions reconstructed with the muon and tau.	30
19	Data/MC comparison histograms in the category 1 after S5 (final). p_T distributions of the leading (left) and sub-leading jets (right).	30
20	Data/MC comparison histograms in the category 1 after S5 (final). η (upper row) and b-tagging discriminator (lower row) distributions of the leading (left column) and sub-leading jets (right column).	31
21	Data/MC comparison histograms in the category 2 after S2. ΔR (left) and mass (right) reconstructed with a muon and tau.	32
22	Data/MC comparison histograms in the category 2 after S3. p_T (left column) and η (right column) distributions for muon (upper row) and tau (lower row).	33
23	Data/MC comparison histograms in the category 2 after S3. ΔR (left) and mass (right) distributions reconstructed with the muon and tau.	34
24	Data/MC comparison histograms in the category 2 for jet multiplicity distribution (left) after S3 and b-tagged jet multiplicity distribution (right) after S4.	34
25	Data/MC comparison histograms in the category 2 after S4. p_T (left column) and η (right column) distributions of the leading (upper row) and sub-leading jets (lower row).	35
26	Data/MC comparison histograms in the category 2 after S6 (final). p_T (left column) and η (right column) distributions for muon (upper row) and tau (lower row).	36
27	Data/MC comparison histograms in the category 2 after S6 (final). ΔR (left) and mass (right) distributions reconstructed with the muon and tau.	37
28	Data/MC comparison histograms in the category 2 after S6 (final). p_T distributions of the leading (left) and sub-leading jets (right).	37

29	Data/MC comparison histograms in the category 2 after S6 (final). η (upper row) and b-tagging discriminator (lower row) distributions of the leading (left column) and sub-leading jets (right column).	38
30	Voigt fitting results for mass of LFV top quark (top), SM top quark (middle), and W boson (bottom) from the left.	43
31	Distributions of χ^2 score from top reconstruction in the category 1 (left) and 2 (right).	44
32	Distributions of SM top mass from top reconstruction in the category 1 (left) and 2 (right).	45
33	Distributions of W boson mass from top reconstruction in the category 1 (left) and 2 (right).	45
34	Distribution of LFV top mass from top reconstruction in the category 2. . . .	46
35	Correlation matrix for signal (upper) and background (lower) input variables in the category 1.	49
36	Correlation matrix for signal (upper) and background (lower) input variables in the category 2.	50
37	Normalized confusion matrix for training models in the category 1 (upper) and 2 (lower).	52
38	DNN output distributions of signals and backgrounds showing agreements in train and test for the category 1 (upper) and 2 (lower). X-axis: Probability, Y-axis: Arbitrary Unit	53
39	DNN output distribution for run 2 evaluation in the category 1 (left) and 2 (right)	54
40	JES systematic variation distributions for p_T of the leading jet (upper row) and E_T^{miss} (lower row) in the category 1 (left column) and 2 (right column). . . .	55
41	Systematic variations for Run II on DNN output distribution in the category 1 (left) and 2 (right).	56
42	Combined run 2 impact of systematic sources when setting limits for scalar-like operators in $t\bar{c}\mu\tau$ (upper) and $t\bar{u}\mu\tau$ (lower) interaction.	58
43	Combined run 2 impact of systematic sources when setting limits for vector-like operators in $t\bar{c}\mu\tau$ (upper) and $t\bar{u}\mu\tau$ (lower) interaction.	59

44	Combined run 2 impact of systematic sources when setting limits for tensor-like operators in $t c \mu \tau$ (upper) and $t u \mu \tau$ (lower) interaction.	60
45	Control plots for p_T (left) and η (right) of selected muon (S1) in the category 1.	68
46	Control plots for p_T (left) and η (right) of selected muon (S2) in the category 1.	68
47	Control plots for p_T (left column) and η (right column) of selected muon (top row) and tau (middle row), and m_T reconstructed with the selected muon and MET (bottom row) (S2) in the category 1.	69
48	Control plots for p_T (left column) and η (right column) of selected muon (upper row) and tau (lower row)(S3) in the category 1.	70
49	Control plots for ΔR (upper left) and $mass$ (upper right) reconstructed with the selected muon and tau (S3) in the category 1. Plots of m_T reconstructed with the selected muon and MET (lower left) and the number of jets (lower right) (S3) in the category 1.	71
50	Control plots for p_T of the leading (upper left), sub-leading (upper right), and third jets (lower) (S4) in the category 1.	72
51	Control plots for η of the leading (upper left), sub-leading (upper right), and third jets (lower left), and the number of b-tagged jet (lower right) (S4) in the category 1.	73
52	Control plots for p_T (left column) and η (right column) of selected muon (upper row) and tau (lower row) (S5) in the category 1.	74
53	Control plots for ΔR (upper left) and mass (upper right) reconstructed with the selected muon and tau and m_T (lower) reconstructed with the selected muon and MET (S5) in the category 1.	75
54	Control plots for p_T of the leading (upper left), sub-leading (upper right), and third jet (lower) (S5) in the category 1.	76
55	Control plots for η of the leading (upper left), sub-leading (upper right), and third jet (lower) (S5) in the category 1.	77
56	Control plots for b-tagging discriminator of the leading (upper left), sub-leading (upper right), and third jet (lower) (S5) in the category 1.	78
57	Control plots for p_T (upper left) and η (upper right) of the b-tagged jet, and MET (lower left) and ϕ of MET (lower right) (S5) in the category 1.	79

58	Control plots for p_T (left) and η (right) of selected muon (S1) in the category 2.	80
59	Control plots for p_T (left) and η (right) of selected muon (S2) in the category 2.	80
60	Control plots for p_T (upper left) and η (upper right) of the selected tau, and m_T (lower) reconstructed with the selected muon and MET (S2) in the category 2.	81
61	Control plots for p_T (left column) and η (right column) of selected muon (upper row) and tau (lower row) (S3) in the category 2.	82
62	Control plots for ΔR (upper left) and <i>mass</i> (upper right) reconstructed with the selected muon and tau (S3) in the category 2. Plots of m_T (lower left) reconstructed with the selected muon and MET and the number of jets (lower right) (S3) in the category 2.	83
63	Control plots for p_T of the leading (upper left), sub-leading (upper right), third (lower left), and fourth (lower right) jets (S4) in the category 2.	84
64	Control plots for η of the leading (upper left), sub-leading (upper right), third (lower left), and fourth (lower right) jets (S4) in the category 2.	85
65	Control plots for MET (upper left), ϕ of MET (upper right), p_T (lower left) and η (lower right) of b-tagged jet (S5) in the category 2.	86
66	Control plots for p_T (left column) and η (right column) of selected muon (upper row) and tau (lower row) (S6) in the category 2.	87
67	Control plots for ΔR (upper left) and mass (upper right) reconstructed with the selected muon and tau, and m_T (lower) reconstructed with the selected muon and MET (S6) in the category 2.	88
68	Control plots for p_T of the leading (upper left), sub-leading (upper right), third (lower left), fourth (lower right) (S6) in the category 2.	89
69	Control plots for η of the leading (upper left), sub-leading (upper right), third (lower left), fourth (lower right) (S6) in the category 2.	90
70	Control plots for b-tagging discriminator of the leading (upper left), sub-leading (upper right), third (lower left), fourth (lower right) (S6) in the category 2.	91
71	Control plots for p_T (upper left) and η (upper right) of the b-tagged jet, and MET (lower left) and ϕ of MET (lower right) (S6) in the category 2.	92

72	Accuracy per epoch distributions when training for the category 1 (upper) and 2 (lower).	93
73	Loss per epoch distributions when training for the category 1 (upper) and 2 (lower).	94



List of Tables

1	Definitions of the EFT operators and corresponding Wilson Coefficients	5
2	Definitions of EFT operators with indices. $t\bar{q}\mu\tau$ operators in upper rows and $t\bar{u}\mu\tau$ operators in lower rows.	6
3	Theoretical calculation of decay width, branching ratio, and cross sections for interaction types in the $t\bar{t}$ LFV process. All values are summed for the vector-like operator case.	12
4	Cross sections of single top and $t\bar{t}$ LFV processes in $t\bar{q}\mu\tau$ interactions where $q \in \{u, c\}$	13
5	Run II Single Muon Data with corresponding integrated luminosity.	14
6	Golden JSON files for Run II data.	14
7	Single Muon HLT Trigger Selection for Run II samples.	15
8	List of Signal LFV MC Samples with cross section and precision.	16
9	List of Background MC Samples with cross section, precision and effective luminosity.	17
10	Cutflow Table for Run2 data and MC samples in the category 1.	40
11	Cutflow Table for Run2 data and MC samples in the category 2.	41
12	Input variables for DNN training in the category 1 and 2.	48
13	Table for run2 combined upper limits of LFV cross section (σ), Wilson Coefficient ($C_{t\bar{q}\mu\tau}$), and branching fraction for different types of interactions. $\pm 1\sigma$ values are in brackets.	57

Abstract

Search for charged lepton flavor violation in the top quark sector with hadronic tau final state using CMS Run 2 data at $\sqrt{s} = 13$ TeV

Jongwon Lim

Dept. of Physics

The Graduate School

Hanyang University

Searching for new physics beyond the Standard Model has been performed in particle physics experiments since the Higgs boson discovery in 2012. The possible violation of lepton universality is proposed in the interaction of particles with the anomaly measurement in $R(D)$ and $R(D^*)$. This analysis aims to search the charged lepton flavor violation (CLFV) phenomenon in top quark interaction using an effective field theory approach. The machine learning technique identifies the CLFV signal events with fine-tuned hyperparameter optimization. In this analysis, we set upper limits of CLFV interaction cross sections, Wilson coefficients, and branching fractions at the confidence level of 95% for each effective operator in top quark interaction.

1 Introduction

1.1 The Standard Model

Particle physics is the study of fundamental particles and their interactions. In our environment, the Earth, we can observe many materials consisting of molecules with their chemical properties. Molecules are composed of atoms in the periodic table, and those atoms can be divided into smaller pieces. An atom consists of atomic nuclei and electrons, and J.J Thomson discovered the electron in 1897 at the beginning of the particle physics experiment. The nucleus of an atom is made up of protons and neutrons, which are baryons with three quarks. Quarks and leptons are the most fundamental particles that cannot be decomposed further.

The standard model describes the properties of quarks, leptons, and bosons with electromagnetic, strong, and weak interactions, as shown in Fig. 1. There are six quarks (up type – up, charm, top quark, down type – down, strange, bottom quark), three leptons (electron, muon, tau), and three corresponding lepton neutrinos. In the standard model, interactions are mediated by gauge bosons (electromagnetic force – photon, strong force – gluon, weak force – W and Z bosons). Higgs boson was named after Peter Higgs who predicted the new boson [1]. The Higgs boson gives mass to massive particles through the strength of the interaction with the Higgs mechanism [2]. Higgs boson was the last of the standard model particles to be discovered in 2012 [3, 4] and the Nobel prize was awarded to Francois Englert and Peter Higgs.

Among the particles in the standard model, the top quark is the heaviest particle with a mass of 172.5 GeV and is even heavier than a Higgs boson mass with 125 GeV . Top quark highly contributes to the production of Higgs boson with its large mass. An accurate understanding of the properties of a top quark and Higgs boson helps expand the boundaries of the new physics. The masses of the top quark and Higgs boson determine the state of the universe as meta-stable of electroweak vacuum [5].

1.2 The CMS Detector

Large Hadron Collider (LHC) [6] is the world’s largest and most powerful particle accelerator, which has 27 km of circumference and is located on the border of France and

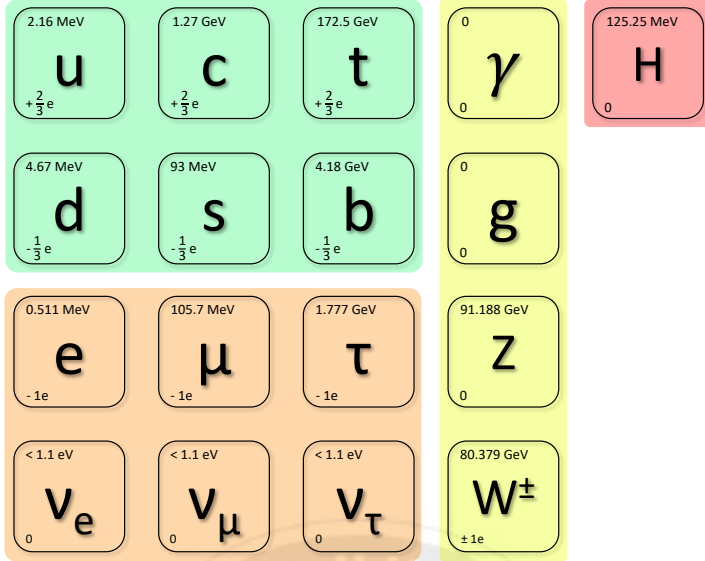


Figure 1: The Standard Model Particles with mass (upper in a box) and charge (lower in a box) properties of particles.

Switzerland. There are four detectors where particle collides – ATLAS, CMS, ALICE, and LHCb experiments. The center of mass energy of the proton–proton collision in the LHC during the Run II period (2015–2018) is 13 TeV , the unprecedented high collision energy in high energy physics experiments. In Run II period of the LHC, the peak luminosity is $2.1 \times 10^{-34} cm^{-2}s^{-1}$ and the integrated luminosity is $138 fb^{-1}$ (2016–2018) measured in the CMS detector. The high collision energy allows for enormous top quark events; thus, the LHC is called a ‘top quark factory.’

Compact Muon Solenoid (CMS) [7] in Fig. 2 is a detector located in the LHC ring and is a general purpose detector. CMS is 15 m high and 21 m long which is more compact than the ATLAS detector. Due to the strong magnetic field of 3.8 T by the solenoid, the CMS detector can be compact with bending particles. The CMS detector consists of several layers to capture rapidly decaying particles. After two protons collide at the center of the CMS detector, lots of particles are produced, and the solenoid’s magnetic field bends them. Silicon tracker tracks the trajectory of a charged particle to measure the momentum of the particles at the innermost part of the CMS detector. The CMS detector has two types of calorimeters for measuring energies of particles – Electromagnetic Calorimeter (ECAL) and Hadron Calorimeter (HCAL). The energy of electrons and photons is measured in the ECAL

by completely stopping them. Hadrons composed of quarks pass through the ECAL and are stopped in the HCAL. Muon lives longer by getting through all the inner parts of the CMS detector, and they are detected in the muon chamber, which is the outermost part of the CMS detector.

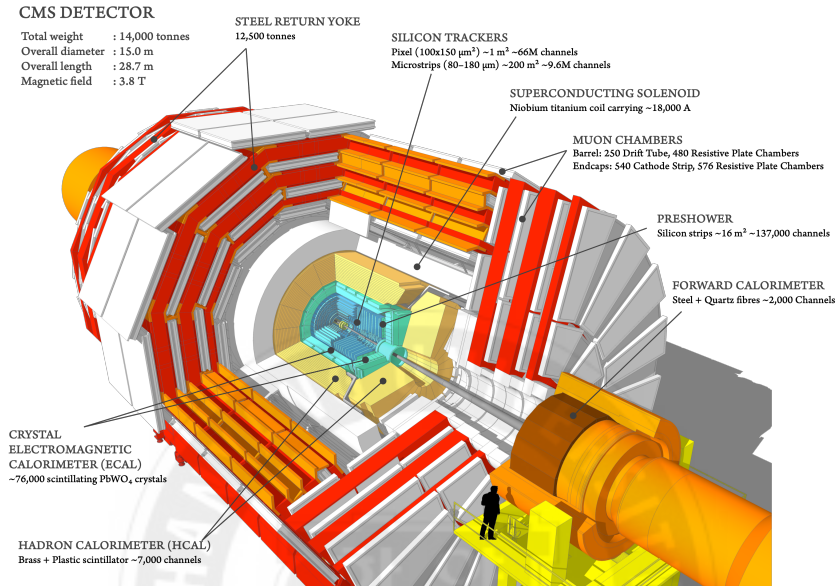


Figure 2: The CMS Detector and the sub-layers of the Detectors [7]

1.3 Lepton Flavor Violation

In the standard model, lepton interaction with a gauge boson is flavor independent. Suppose that a W boson decays to a lepton and a neutrino. The branching ratio of all lepton channels is the same as 1:1:1 for electron, muon, and tau where lepton universality is conserved. There are analyses testing lepton universality with observing $R(D)$ and $R(D^*)$ performed by BaBar [8], Belle [9 – 11] and LHCb [12, 13]. In Fig. 3, the average of $R(D)$ and $R(D^*)$ measurements are 0.299 and 0.254, respectively, and the average result shows differences of 3σ from the standard model expectation. From this significant gap from the standard model, we can assume the new physics of the violation of the lepton universality, and this analysis focuses on the lepton flavor violation (LFV).

A leptoquark is a hypothetical boson interacting both with a quark and a lepton, violating the lepton number conservation. A phenomenology study is performed for correlation between $R_{D^{(*)}}$ and top quark decay in flavor-changing neutral current with two or three

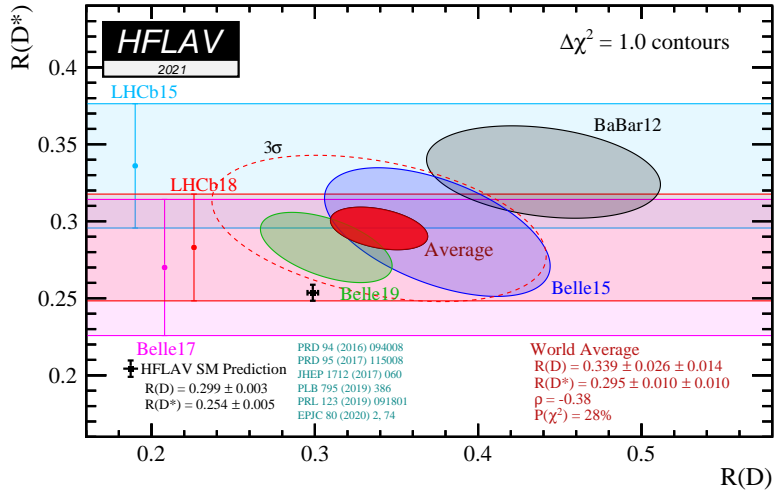


Figure 3: HFLAV average results of $R(D)$ and $R(D^*)$ measurement [14].

body processes of the top quark ($t \rightarrow cV$ or $t \rightarrow cl_i l_j$) mediated by a scalar or a vector type leptoquark [15]. The lower bounds of the mass are set with the first, second, or third generation leptoquark models in the TeV scale using collision data in the CMS experiment [16–20]. The possible LFV process in low energy are $\mu \rightarrow e$ conversion processes [21, 22]. Provided the high sensitivity of the LFV interactions involving a heavy quark and boson by LHC, the CMS and ATLAS experiments have performed LFV searching study on the interaction with the Z boson or Higgs boson [23–25]. The limits for the branching ratio [26–28] are set with heavy bosons involved in LFV interactions. The $t \rightarrow Zq$ analysis which set $Br(t \rightarrow qe\mu) < 6 \times 10^{-5}$ using 20 fb^{-1} data at 8 TeV by the CMS experiment, is recasted by the LHC to $Br(t \rightarrow qe\mu) < 1 \times 10^{-5}$ with extrapolating 100 fb^{-1} data at 13 TeV [29]. The LFV interactions are interpreted with an effective field theory (EFT) model for model-independent study. Recently, the CMS collaboration reported the results of the search for CLFV using the EFT model in the top quark sector with no significant excess over the background expectation [30]. We use the same EFT model that is used for the analysis of an electron and a muon involving interactions.

In this thesis, Section 2 introduces the LFV signal using EFT interpretation. The samples used for this analysis is explained in Section 3 and the definitions of object and event selections are defined in Section 4. After the event selection, histograms of data and MC events are compared in Section 5 and top mass is reconstructed in Section 6. The LFV signals are

extracted in Section 7 and systematic uncertainties are studied in Section 8. Finally, upper limits on cross section, Wilson coefficient, and branching ratio are set in Section 9.

2 Lepton Flavor Violation in Top Quark using EFT

2.1 Effective Field Theory Interpretation

In this analysis, we focus on the top quark interaction with an up-type quark (up or charm), a muon, and a tau lepton. The interaction is interpreted with four fermion interaction with the effective field theory (EFT) model provided by LHC Top working group [31]. The model exploits an effective lagrangian expansion from the standard model (SMEFT). The total lagrangian is described as two terms with the standard model lagrangian and the effective term in the Eq. 1.

$$\mathcal{L}_{BSM} = \mathcal{L}_{SM}^{(4)} + \sum_i \frac{c_i O_i^D}{\Lambda^{D-4}} = \mathcal{L}_{SM}^{(4)} + \sum_i \frac{c_i O_i^{(6)}}{\Lambda^2} \quad (1)$$

The operators in the effective lagrangian are based on the Warsaw basis of the dimension-6 operator, O_i^D where $D = 6$. Since the renormalizable SM Lagrangian contains only operators whose dimension is less than four, it is possible to study the beyond SM interaction with the higher order SMEFT operator [32]. For each operator, the coupling strength is multiplied with a constant called Wilson coefficient (C_i) and is initially set to 1. The scale of interaction is 1 TeV written in Λ . We utilize operators for four fermion interaction operators, especially the operators for two heavy-flavor quarks and two leptons interactions in Table 1.

Type	Operator	Definition	Wilson Coefficient
Scalar	$O_{lequ}^{1(ijkl)}$	$(\bar{l}_i e_j) \varepsilon (\bar{q}_k u_l)$	C_{lequ1}
Vector	$O_{lq}^{1(ijkl)}$	$(\bar{l}_i \gamma^\mu l_j)(\bar{q}_k \gamma^\mu q_l)$	C_{lq}
	$O_{lq}^{3(ijkl)}$	$(\bar{l}_i \gamma^\mu \tau^I l_j)(\bar{q}_k \gamma^\mu \tau^I q_l)$	
	$O_{lu}^{(ijkl)}$	$(\bar{l}_i \gamma^\mu l_j)(\bar{u}_k \gamma^\mu u_l)$	C_{lu}
	$O_{eq}^{(ijkl)}$	$(\bar{e}_i \gamma^\mu e_j)(\bar{q}_k \gamma^\mu q_l)$	C_{eq}
	$O_{eu}^{(ijkl)}$	$(\bar{e}_i \gamma^\mu e_j)(\bar{u}_k \gamma^\mu u_l)$	C_{eu}
Tensor	$O_{lequ}^{3(ijkl)}$	$(\bar{l}_i \sigma^{\mu\nu} e_j) \varepsilon (\bar{q}_k \sigma^{\mu\nu} u_l)$	C_{lequ3}

Table 1: Definitions of the EFT operators and corresponding Wilson Coefficients

In Table 1, the indices of flavors $(ijkl)$ indicates the generations of interacting fermions

(e.g. $ijkl = 2323$ for the $t\mu\tau$ interaction). Left-handed fermion doublets are denoted as q and l, and right-handed fermion singlets are written as u and e. The anti-symmetric $SU(2)$ tensor is defined as $\epsilon \equiv i\tau^2$ where τ^I are the Pauli matrices. The EFT operator takes different chirality combinations of quarks and leptons by the definition of each operator. For example, the operator O_{lequ}^3 is applied for the interaction between the mixed-handed chirality of quarks and leptons, and it is classified as a tensor-like operator due to the $\sigma^{\mu\nu}$ symbol. The operators O_{lq}^1 and O_{lq}^3 have the same Lorentz structure and O_{lq}^1 operator represents O_{lq} operator for the interaction of left-handed leptons and quarks. The analysis uses six independent EFT operators, and corresponding Wilson coefficients are defined in Table 2.

Wilson Coefficient	Definitions with Indices			
$C_{lq}^{t\mu\tau}$	$C_{lq}^{1(2323)}$	$C_{lq}^{1(2332)}$	$C_{lq}^{1(3223)}$	$C_{lq}^{1(3232)}$
$C_{lu}^{t\mu\tau}$	C_{lu}^{2323}	C_{lu}^{2332}	C_{lu}^{3223}	C_{lu}^{3232}
$C_{eq}^{t\mu\tau}$	C_{eq}^{2323}	C_{eq}^{2332}	C_{eq}^{3223}	C_{eq}^{3232}
$C_{eu}^{t\mu\tau}$	C_{eu}^{2323}	C_{eu}^{2332}	C_{eu}^{3223}	C_{eu}^{3232}
$C_{lequ}^{1(t\mu\tau)}$	$C_{lequ}^{1(2323)}$	$C_{lequ}^{1(2332)}$	$C_{lequ}^{1(3223)}$	$C_{lequ}^{1(3232)}$
$C_{lequ}^{3(t\mu\tau)}$	$C_{lequ}^{3(2323)}$	$C_{lequ}^{3(2332)}$	$C_{lequ}^{3(3223)}$	$C_{lequ}^{3(3232)}$
$C_{lq}^{tu\mu\tau}$	$C_{lq}^{1(2313)}$	$C_{lq}^{1(2331)}$	$C_{lq}^{1(3213)}$	$C_{lq}^{1(3231)}$
$C_{lu}^{tu\mu\tau}$	C_{lu}^{2313}	C_{lu}^{2331}	C_{lu}^{3213}	C_{lu}^{3231}
$C_{eq}^{tu\mu\tau}$	C_{eq}^{2313}	C_{eq}^{2331}	C_{eq}^{3213}	C_{eq}^{3231}
$C_{eu}^{tu\mu\tau}$	C_{eu}^{2313}	C_{eu}^{2331}	C_{eu}^{3213}	C_{eu}^{3231}
$C_{lequ}^{1(tu\mu\tau)}$	$C_{lequ}^{1(2313)}$	$C_{lequ}^{1(2331)}$	$C_{lequ}^{1(3213)}$	$C_{lequ}^{1(3231)}$
$C_{lequ}^{3(tu\mu\tau)}$	$C_{lequ}^{3(2313)}$	$C_{lequ}^{3(2331)}$	$C_{lequ}^{3(3213)}$	$C_{lequ}^{3(3231)}$

Table 2: Definitions of EFT operators with indices. $t\mu\tau$ operators in upper rows and $tu\mu\tau$ operators in lower rows.

We use six kinds of EFT operator, $O_{lq}, O_{lu}, O_{eq}, O_{eu}, O_{lequ1}$ and O_{lequ3} , and they can be classified with the mathematical structure of the definition of operators. The operator O_{lequ1} is scalar-like operator and O_{lequ3} is tensor-like operator, categorized in Table 1. And four other operators, O_{lq}, O_{lu}, O_{eq} , and O_{eu} , are vector-like operators. The four vector-like operators are combined into one to reduce the free parameters of the analysis and studied after some justification in a generator-level study of each operator.

2.2 Generator Level Study

There are top quark production (single top or ST) and top quark decay processes ($t\bar{t}$) in LFV interaction. In Fig. 4, Feynman diagrams for ST and $t\bar{t}$ LFV processes are shown with the red EFT interaction. There are two channels for ST LFV processes, s-channel for annihilation and t-channel for scattering. We choose the hadronic top quark decay in the SM process for both ST and $t\bar{t}$ LFV processes to study hadronic tau with a simpler system than in multi-leptonic final states. Samples used for the LFV signals are produced separately for two processes (ST and $t\bar{t}$) and three types of operators (scalar, vector, tensor), and further information about the samples is in Section 3. The purposes of the generator study are to understand the kinematic distributions regarding LFV objects before reconstruction in the detector (reconstruction level) and to establish the criteria for event selections.

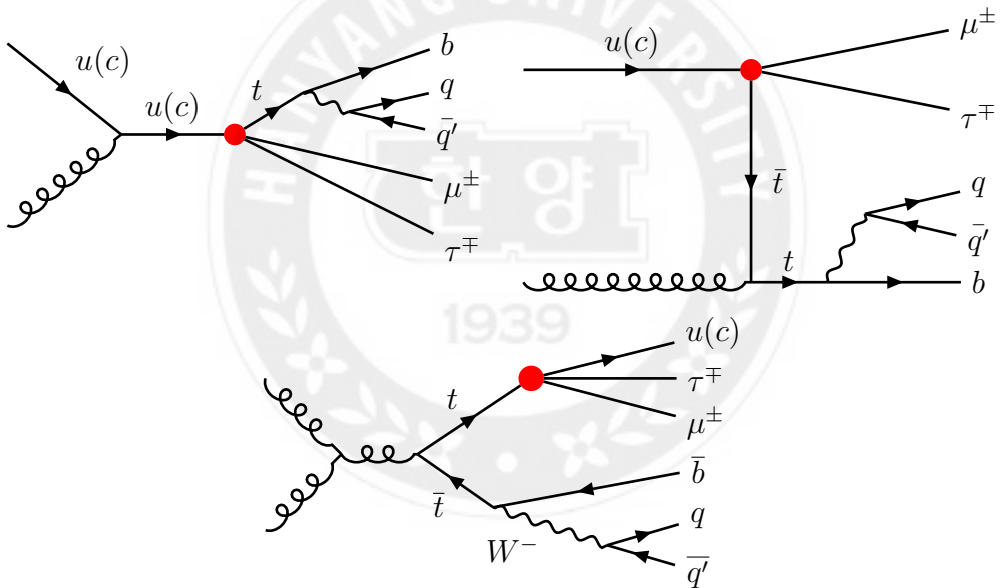


Figure 4: Feynman diagrams for the ST LFV (upper row) and $t\bar{t}$ LFV (lower row) processes.

Firstly, the kinematic distributions of LFV objects from the $t\bar{t}$ LFV process are compared for the cases of six different EFT operators with the standard model $t\bar{t}$ di-leptonic MC events. In Fig. 5, distributions of transverse momentum (p_T) and pseudorapidity (η) are compared for a muon and tau from the LFV top decay. A muon and tau from the LFV top decay have relatively larger p_T than the SM top decay. Vector-like operators are consistent in shape for most of the distributions in Fig. 5. Especially in Fig. 6, distributions of ΔR and $M_{\mu,\tau}$

from vector-like operator interaction have clearly different shapes from scalar-like (C_{lequ}^1) and tensor-like (C_{lequ}^3) operators. Since the order of the coupling constants is similar to the definition of vector-like operators, it is natural to merge all four vector-like operators into one. After merging the vector-like operators into one, the kinematic distributions of the muon and the tau show noticeable differences for scalar, vector, and tensor-like operators, mainly in p_T distributions, in Fig. 7 and 8.

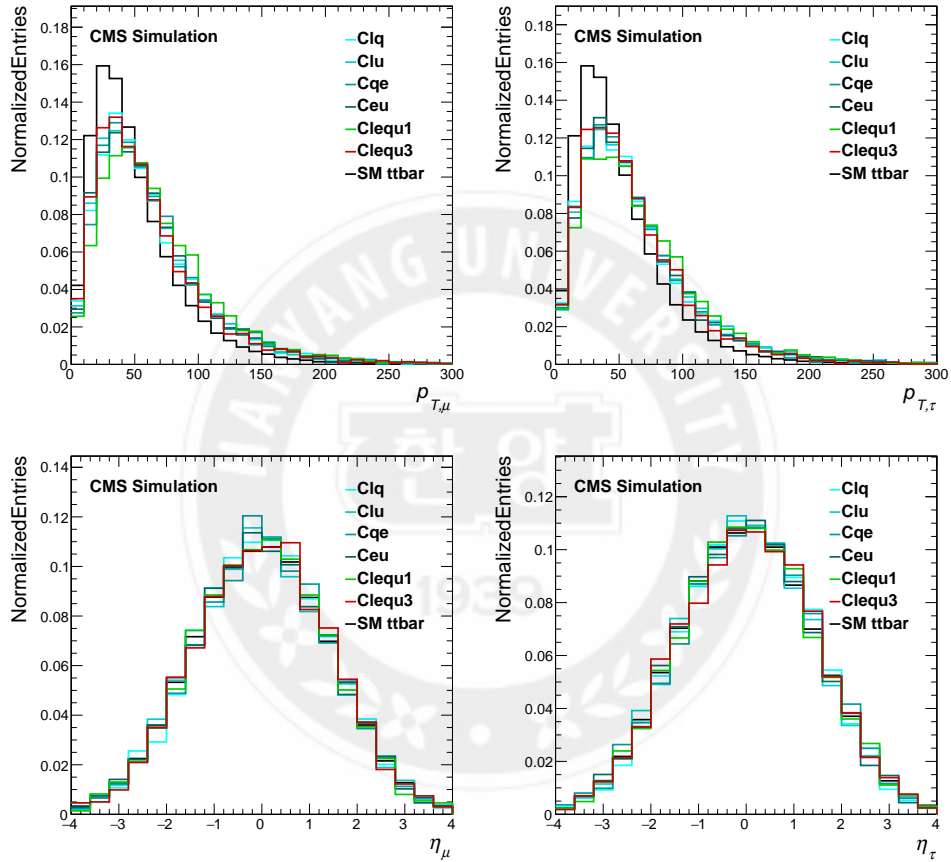


Figure 5: Generator-level p_T (upper row) and η (lower row) distributions of a muon (left column) and tau (right column) from the LFV top decay.

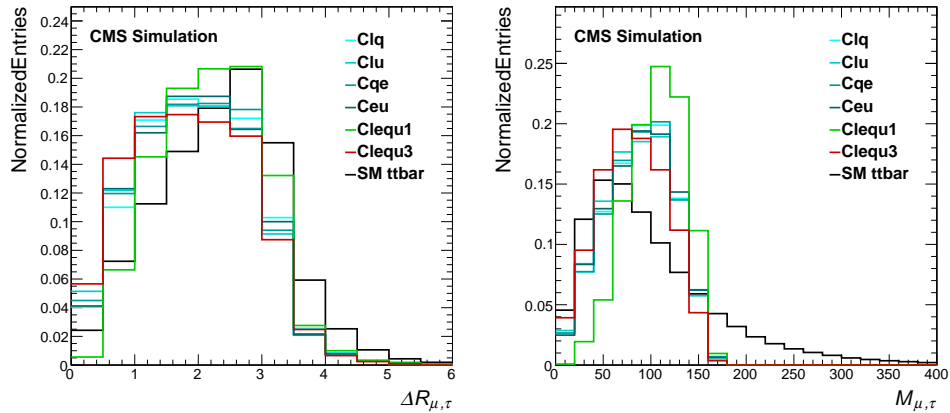


Figure 6: Generator-level distributions of ΔR (left) and mass (right) reconstructed with a muon and a tau from LFV top decay.

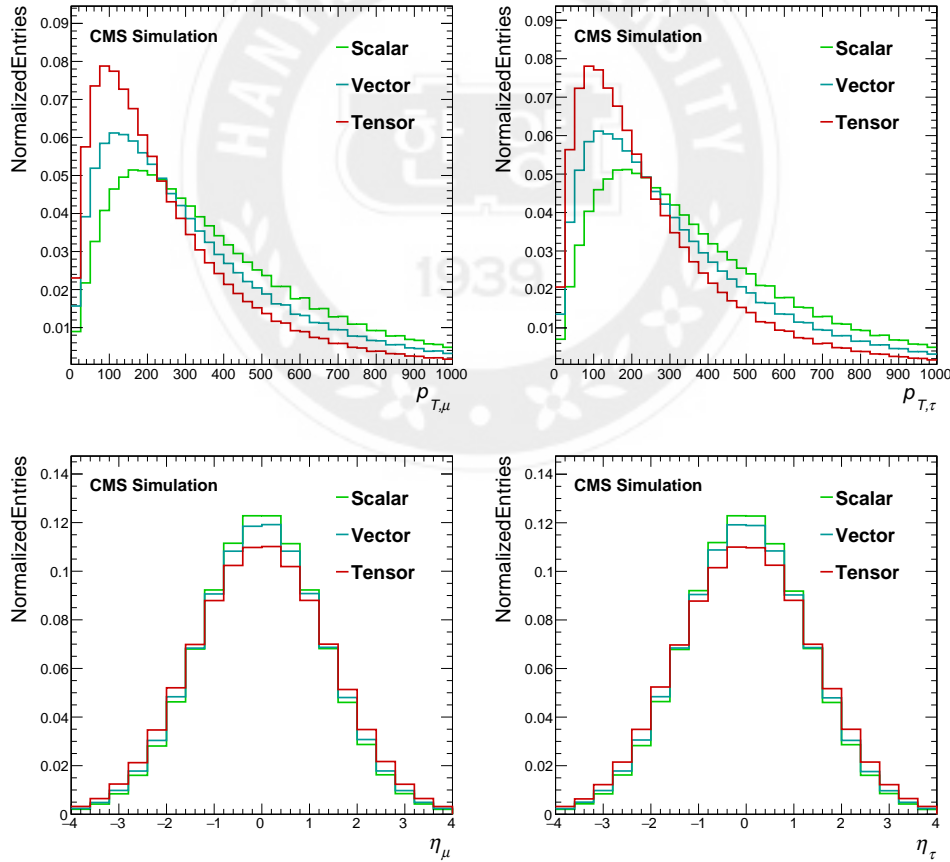


Figure 7: Generator-level p_T (upper row) and η (lower row) distributions of a muon (left column) and tau (right column) from the LFV top decay.

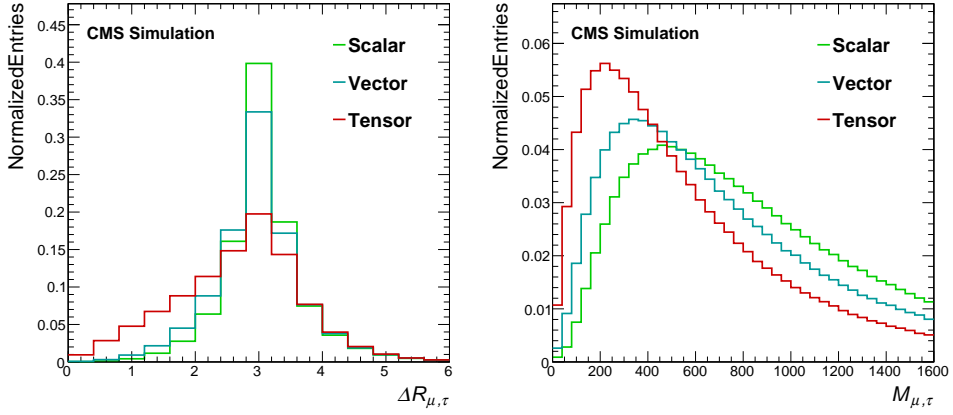


Figure 8: Generator-level distributions of ΔR (left) and mass (right) reconstructed with a muon and tau from LFV top decay.

The second study at the generator level is to understand the kinematic criteria for establishing the event selection. We have two processes ST and $t\bar{t}$ LFV, and the generator-level final objects have huge differences between ST and $t\bar{t}$ LFV processes. In the LFV top quark production process, a muon and tau are directly produced with the large recoiled energy from the initial particle (up or charm quark). For this reason, the muon and tau from the ST LFV process have larger energy than from the $t\bar{t}$ LFV process as in Fig. 9 and the fact is used to apply proper requirements in object selections. With the muon and tau, the ΔR and mass are reconstructed, and the differences are enormous between ST and $t\bar{t}$ LFV events, as shown in Fig. 10. Using the differences of the mass ($M_{\mu,\tau}$) distribution in ST and $t\bar{t}$ LFV process, event categories are defined differently for ST LFV enriched and $t\bar{t}$ LFV enriched regions in Section 3.

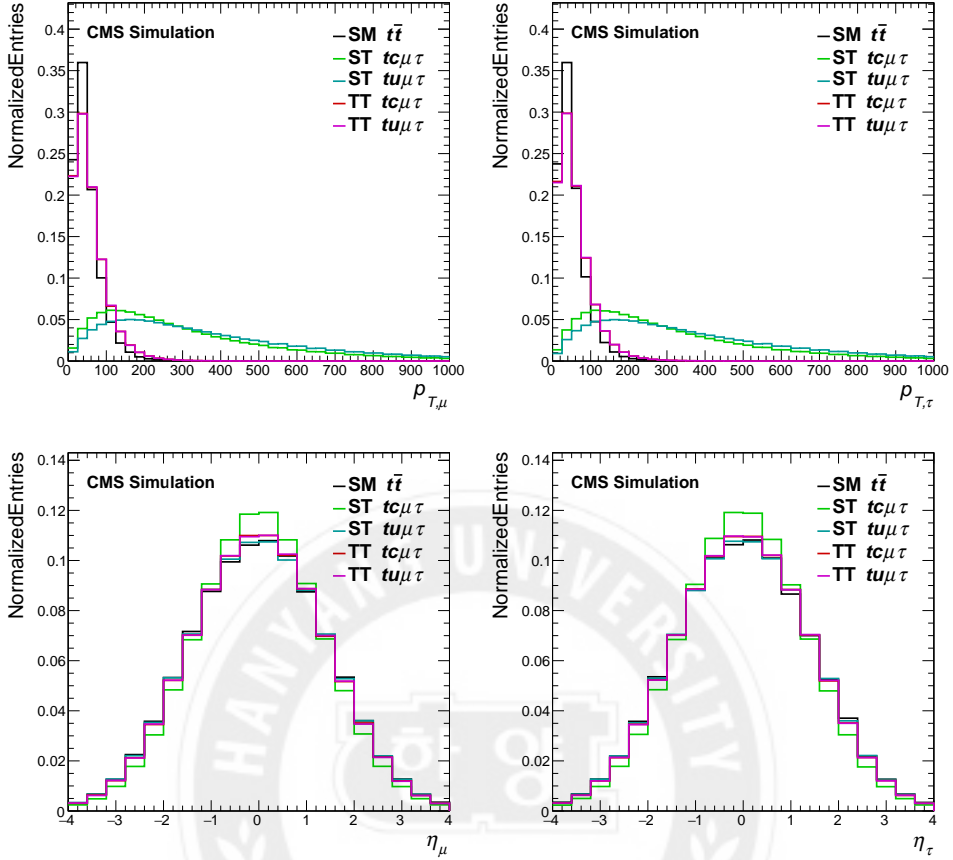


Figure 9: Generator-level p_T (upper row) and η (lower row) distributions of a muon (left column) and tau (right column) from LFV top interaction with vector-like operator.

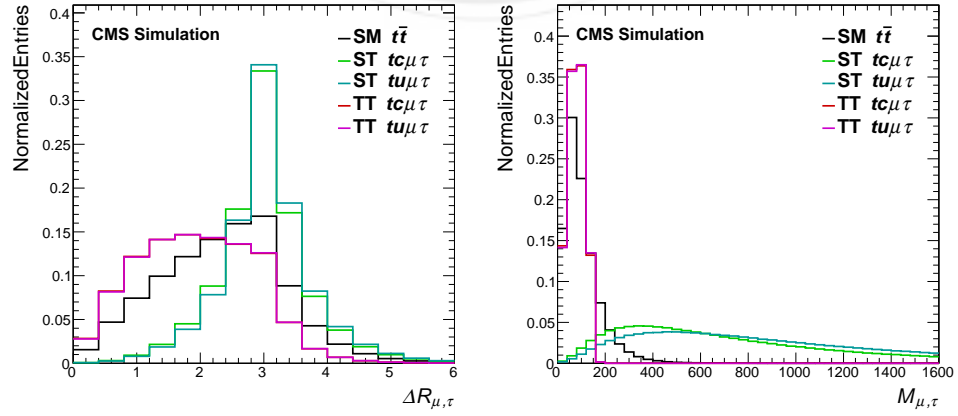


Figure 10: Generator-level distributions of ΔR (left) and mass (right) reconstructed with a muon and a tau from LFV top interaction with vector-like operator.

2.3 Signal Cross Sections

In the high energy experiment, the cross-section refers to a production probability of a specific process. In this analysis, we are interested in ST and $t\bar{t}$ LFV processes, and each process has three interaction types of EFT operators. The signal cross-section for ST LFV processes is directly obtained from the matrix element calculating program, and more details about the program are introduced in Section 3. For $t\bar{t}$ LFV processes, the branching fractions of an LFV decaying top quark are theoretically calculated and further normalized with $t\bar{t}$ inclusive cross-section of 832 pb with the next-to-next leading order (NNLO) precision [33]. The tree-level contributions (Γ_{LFV}) of three types of EFT operators are calculated with the Eq. 2 where Wilson coefficient $C_i = 1$, $\Lambda = 1\text{ TeV}$ as a scale of new physics (NP) and a top quark mass of $m_t = 172.5\text{ GeV}$.

$$\Gamma(t \rightarrow u(c)\mu^\pm\tau^\mp) = \begin{cases} \frac{|C_i|^2}{\Lambda^4} \frac{1}{6144\pi^3} m_t^5 \times 2 & \text{(for Scalar-like operator)} \\ \frac{|C_i|^2}{\Lambda^4} \frac{1}{1536\pi^3} m_t^5 & \text{(for Vector-like operators)} \\ \frac{|C_i|^2}{\Lambda^4} \frac{1}{128\pi^3} m_t^5 \times 2 & \text{(for Tensor-like operator)} \end{cases} \quad (2)$$

Decay widths are identically calculated. The decay widths are doubled for the cases of scalar and tensor-like operators due to the mixed-handed chirality of EFT operators by definition. Branching fraction for LFV process is calculated with the ratio in Γ_{LFV}/Γ_{SM} where $\Gamma_{SM} = \Gamma_t = 1.33\text{ GeV}$. In Table. 3, the theoretical calculation of LFV top decay widths, branching fractions, and cross sections are shown with different interaction operators. Cross sections are normalized to NNLO $t\bar{t}$ cross-section as introduced, and the factor of 0.6 is multiplied for hadronic top quark decay in the SM part. The theoretical values for all four vector-like EFT operator cases are summed.

Operator	$\Gamma(t \rightarrow u(c)\mu^\pm\tau^\mp) [\text{GeV}]$	$Br(t \rightarrow u(c)\mu^\pm\tau^\mp)$	$\sigma [\text{fb}]$
O_{scalar}	1.604×10^{-6}	1.206×10^{-6}	2.69
O_{vector}	12.83×10^{-6}	9.644×10^{-6}	21.5
O_{tensor}	7.697×10^{-5}	5.787×10^{-5}	129.0

Table 3: Theoretical calculation of decay width, branching ratio, and cross sections for interaction types in the $t\bar{t}$ LFV process. All values are summed for the vector-like operator case.

In Table. 4, the cross sections are listed for ST LFV processes which are obtained from the program with leading order (LO) precision and theoretical $t\bar{t}$ LFV processes with NNLO precision. The detailed information of samples for ST LFV processes is described in Section 3.

Process	Interaction Type	Cross section [fb]	Precision
ST $t u \mu \tau$	Scalar	83.8	LO
	Vector	393	
	Tensor	1,796	
ST $t c \mu \tau$	Scalar	7.40	NNLO
	Vector	36.8	
	Tensor	178.4	
$t\bar{t} t q \mu \tau$	Scalar	2.69	NNLO
	Vector	21.5	
	Tensor	129.0	

Table 4: Cross sections of single top and $t\bar{t}$ LFV processes in $t q \mu \tau$ interactions where $q \in \{u, c\}$.

3 Samples

This analysis uses the combination of the collected collision data collected by the CMS experiment and Monte-Carlo (MC) simulation samples generated by CMS collaboration. The data and MC simulated events are compared for signal and background study. The collision data are produced during Run II LHC operation (2016–2018), and corresponding MC samples are used.

3.1 Data

We use a single muon dataset in which events with a muon are triggered by the CMS’s data acquisition (DAQ) system consisting L1 and HLT triggers [34, 35]. The integrated luminosity is 138 fb^{-1} for Run II corresponding single muon data. There are AOD, MiniAOD, and NanoAOD data tiers in the CMS experiment, and the NanoAOD tier has the smallest size per event (1–2 kb / 1 event). This analysis uses the NanoAOD dataset, whose version is the legacy version ‘MiniAODv1_NanoAODv2’ or ‘v8’. In Table. 5, the single muon datasets are listed with separated runs in 16APV (19.5 fb^{-1}), 16 (16.8 fb^{-1}), 17 (41.5 fb^{-1}), and 18 (59.8 fb^{-1}) with corresponding luminosity. The meaning of 16 (APV), 17, and 18 are the

Runs	Samples	$\mathcal{L} [fb^{-1}]$
16APV	/SingleMuon/Run2016B-ver2_HIPM_UL2016_MiniAODv1_NanoAODv2-v1/NANOAOD /SingleMuon/Run2016C-UL2016_MiniAODv1_NanoAODv2-v1/NANOAOD /SingleMuon/Run2016D-UL2016_MiniAODv1_NanoAODv2-v1/NANOAOD /SingleMuon/Run2016E-UL2016_MiniAODv1_NanoAODv2-v1/NANOAOD /SingleMuon/Run2016F-HIPM_UL2016_MiniAODv1_NanoAODv2-v1/NANOAOD	19.5
16	/SingleMuon/Run2016F-UL2016_MiniAODv1_NanoAODv2-v4/NANOAOD /SingleMuon/Run2016G-UL2016_MiniAODv1_NanoAODv2-v1/NANOAOD /SingleMuon/Run2016H-UL2016_MiniAODv1_NanoAODv2-v1/NANOAOD	16.8
17	/SingleMuon/Run2017B-UL2017_MiniAODv1_NanoAODv2-v1/NANOAOD /SingleMuon/Run2017C-UL2017_MiniAODv1_NanoAODv2-v1/NANOAOD /SingleMuon/Run2017D-UL2017_MiniAODv1_NanoAODv2-v1/NANOAOD /SingleMuon/Run2017E-UL2017_MiniAODv1_NanoAODv2-v2/NANOAOD /SingleMuon/Run2017F-UL2017_MiniAODv1_NanoAODv2-v2/NANOAOD	41.5
18	/SingleMuon/Run2018A-UL2018_MiniAODv1_NanoAODv2-v1/NANOAOD /SingleMuon/Run2018B-UL2018_MiniAODv1_NanoAODv2-v1/NANOAOD /SingleMuon/Run2018C-UL2018_MiniAODv1_NanoAODv2-v1/NANOAOD /SingleMuon/Run2018C-UL2018_MiniAODv1_NanoAODv2-v2/NANOAOD	59.8

Table 5: Run II Single Muon Data with corresponding integrated luminosity.

data produced in 2016, 2017, and 2018 respectively during the LHC Run II period. The data produced in 2016 are separated into two different reconstructions with or without HIP migration (HIPM) due to VFP (pre-amplifier Feedback Voltage Bias) issue. Run 16APV data is pre-VFP (aka. HIMP, APV) where is VFP issue and run 16 data have no VFP issue. The integrated luminosity of Run 2 data is calculated by Luminosity POG in CMS collaboration and JSON files used for calculation are listed in Table 6.

Runs	JSON
16(APV)	Cert_271036-284044_13TeV_Legacy2016_Collisions16_JSON.txt
17	Cert_294927-306462_13TeV_UL2017_Collisions17_GoldenJSON.txt
18	Cert_314472-325175_13TeV_Legacy2018_Collisions18_JSON.txt

Table 6: Golden JSON files for Run II data.

Trigger Selection There are two level triggers in the CMS DAQ system, one is L1 (level 1) trigger and the other is high level trigger (HLT). We use the single muon dataset triggered by L1 trigger of the CMS DAQ system and select events with an isolated muon with the HLT of CMS DAQ system. The events with an isolated muon with $p_T > 24$ (27) GeV are triggered by single muon HLT triggers listed in Table. 7. For run 2016, two triggers are required together with a logical OR.

Runs	Single Muon Trigger
16(APV)	HLT_IsoMu24 or HLT_IsoTkMu24
17	HLT_IsoMu27
18	HLT_IsoMu24

Table 7: Single Muon HLT Trigger Selection for Run II samples.

3.2 MC Simulation Samples

Generally, a particle collision event simulation is performed in several steps. Firstly, the matrix element is calculated with the Monte Carlo (MC) method, the precision of the leading order or next leading order (NLO). In the cases of the samples used in this analysis, MadGraph [36, 37] and POWHEG [38 – 40] programs are used for matrix element calculation. Second, after the generation of tree-level events, the hadronization process comes with producing hadrons using quarks or gluons, and Pythia8 [41] simulates it. The rest of the process is a detector simulation by GEANT4 [42 – 44] that simulates particles passing through the layers of the CMS detector. The procedures of GEANT4 event simulation are LHEGEN, SIM, DIGIPremix, HLT, RECO, MiniAOD, and NanoAOD, in order. The MC samples produced after the RECO step can be used for the analysis because the collision data are produced from the RECO step. The reconstructed objects are specifically defined through the MiniAOD and NanoAOD production steps, and the size per event is reduced. This analysis uses the sample produced after the NanoAOD step with well-defined variables with the smallest dataset size per event (4 kb / 1 event). The version of the NanoAOD is ‘v8’, which is the same as the ultra-legacy NanoAODv2.

Signal Samples

Signal LFV samples are officially produced by CMS collaboration using GEANT4 framework with Madgraph event generation in leading order (LO) precision and are further hadronized with Pythia8 with CP5 tune. The ST and $t\bar{t}$ LFV samples are generated separately. The samples are divided into the three operator types (scalar, vector, tensor) and two interactions with up-type quark flavors (up or charm). The cross sections for the samples are introduced again with the exact dataset names in Table. 8.

LFV Signal Samples	σ [fb]	Precision
ST_LFV_TCMuTau_Scalar_TuneCP5_13TeV-madgraph-pythia8	7.40	LO
ST_LFV_TCMuTau_Vector_TuneCP5_13TeV-madgraph-pythia8	36.8	
ST_LFV_TCMuTau_Tensor_TuneCP5_13TeV-madgraph-pythia8	178.4	
ST_LFV_TUMuTau_Scalar_TuneCP5_13TeV-madgraph-pythia8	83.8	
ST_LFV_TUMuTau_Vector_TuneCP5_13TeV-madgraph-pythia8	393	
ST_LFV_TUMuTau_Tensor_TuneCP5_13TeV-madgraph-pythia8	1,796	
TT_LFV_TToCMuTau_Scalar_TuneCP5_13TeV-madgraph-pythia8	2.69	NNLO
TT_LFV_TToCMuTau_Vector_TuneCP5_13TeV-madgraph-pythia8	21.5	
TT_LFV_TToCMuTau_Tensor_TuneCP5_13TeV-madgraph-pythia8	129.0	
TT_LFV_TToUMuTau_Scalar_TuneCP5_13TeV-madgraph-pythia8	2.69	
TT_LFV_TToUMuTau_Vector_TuneCP5_13TeV-madgraph-pythia8	21.5	
TT_LFV_TToUMuTau_Tensor_TuneCP5_13TeV-madgraph-pythia8	129.0	

Table 8: List of Signal LFV MC Samples with cross section and precision.

Background Samples

Background MC samples estimate the standard model background and compare them with data or signal events. The background MC samples for Run II are listed in Table. 9 with the cross-section, precision, and effective luminosity for each run. Cross section values are referenced from the cross-section table by Higgs PAG [45] in CMS collaboration. The effective luminosity (\mathcal{L}_{eff}) indicates whether the number of generated events is enough compared to the data, calculated by dividing the number of generated events by the cross-section.

The samples are simulated using GEANT4 simulation with 106X CMSSW release by CMS collaboration. Events are generated with matrix element calculator (MadGraph or Powheg) and parton shower (hadronization) with Pythia8 using CP5 tune with the NNPDF3.1 parton distribution function set. The $t\bar{t}$ samples are generated with Powheg at next leading order (NLO) in QCD and a top quark mass of 172.5 GeV is used for the generation. The top quark pair production cross section is scaled to its best theoretical prediction at next-to-next leading order (NNLO) in QCD, $\sigma_{t\bar{t}} = 832^{+4.8\%}_{-5.5\%} pb$ [33, 46]. Total uncertainty of $t\bar{t}$ cross section is the sum in quadrature of the scale uncertainty and the PDF + alphaS uncertainty. Inclusive W+Jets sample is required on a sum of p_T of generator level jets (H_T) $< 100 GeV$ for using H_T binned samples. Additional factors provided by Generator POG in CMS collaboration are applied for the cross sections of the W+Jets H_T binned samples on cross section values to make smooth H_T bin stitching.

Background MC Samples	$\sigma [pb]$	Precision	Effective Luminosity (\mathcal{L}_{eff}) [fb^{-1}]			
			16APV	16	17	18
TTTo2LNu_TuneCP5_13TeV-powheg_pythia8	88.29		468.5	537.7	1211.7	1681.6
TTToSemiLeptonic_TuneCP5_13TeV-powheg_pythia8	365.34	NNLO	365.6	419.6	941.4	1287.9
TTToHadronic_TuneCP5_13TeV-powheg_pythia8	377.96		267.8	308.2	675.3	930.6
DYJetsToLL_M-10to50_TuneCP5_13TeV-madgraphMLM_pythia8	18,610	NLO	1.7	1.4	3.7	5.3
DYJetsToLL_M-50_TuneCP5_13TeV-madgraphMLM_pythia8	6,077.22	NNLO QCD, NLO EW	15.1	15.7	32.0	32.3
ST_t-channel_antitop_4f_InclusiveDecays_TuneCP5_13TeV-powheg-madspin_pythia8	136.02	NLO	228.1	224.0	508.7	697.4
ST_t-channel_top_4f_InclusiveDecays_TuneCP5_13TeV-powheg-madspin_pythia8	80.95		691.3	776.1	1566.5	2180.0
ST_tW_antitop_5f_InclusiveDecays_TuneCP5_13TeV-powheg-madspin_pythia8	35.85	approx.NNLO	64.2	70.4	153.9	161.2
ST_tW_top_5f_InclusiveDecays_TuneCP5_13TeV-powheg_pythia8	35.85		64.2	67.9	158.1	166.8
TTWJetsToLNu_TuneCP5_13TeV-amcatnloFXFX-madspin_pythia8	0.2043		14065	3627.4	36539	51506
TTWJetsToQQ_TuneCP5_13TeV-amcatnloFXFX-madspin_pythia8	0.4062	NLO	759.3	760.7	1695.8	2388.4
TTZToLLNuNu_M-10_TuneCP5_13TeV-amcatnlo_pythia8	0.2529		22839	24559	56133	79051
TTZToQQ_TuneCP5_13TeV-amcatnlo_pythia8	0.5297		12060	10944	26721	37682
WW_TuneCP5_13TeV-pythia8	118.7	NNLO QCD	134.1	134.0	133.8	132.0
WZ_TuneCP5_13TeV-pythia8	47.13	NLO	167.8	164.8	167.6	169.4
ZZ_TuneCP5_13TeV-pythia8	16.523		76.9	67.4	163.9	236.5
WjetsToLNu_TuneCP5_13TeV-madgraphMLM_pythia8	59,342.5	NNLO	1.3	1.5	1.4	1.4
WjetsToLNu_HT-100To200_TuneCP5_13TeV-madgraphMLM_pythia8	1,335.6		16.3	14.7	35.7	49.6
WjetsToLNu_HT-200To400_TuneCP5_13TeV-madgraphMLM_pythia8	360.4		0.6	46.0	117.6	157.9
WjetsToLNu_HT-400To600_TuneCP5_13TeV-madgraphMLM_pythia8	49.35		50.8	45.3	110.9	152.9
WjetsToLNu_HT-600To800_TuneCP5_13TeV-madgraphMLM_pythia8	13.50	NLO	178.0	163.4	406.3	559.7
WjetsToLNu_HT-800To1200_TuneCP5_13TeV-madgraphMLM_pythia8	6.612		377.3	331.3	815.2	1122.0
WjetsToLNu_HT-1200To2500_TuneCP5_13TeV-madgraphMLM_pythia8	1.770		1197.7	1181.1	2788.7	3873.0
WjetsToLNu_HT-2500ToInf_TuneCP5_13TeV-madgraphMLM_pythia8	0.1351		597.3	5012.1	8776.5	15527
QCD_Pt-15To20_MuEnrichedPt5_TuneCP5_13TeV-pythia8	3819570		0.0012	0.0012	0.0024	0.0024
QCD_Pt-20To30_MuEnrichedPt5_TuneCP5_13TeV-pythia8	2960198		0.0106	0.0102	0.0215	0.0205
QCD_Pt-30To50_MuEnrichedPt5_TuneCP5_13TeV-pythia8	1652472		0.0172	0.0214	0.0355	0.0352
QCD_Pt-50To80_MuEnrichedPt5_TuneCP5_13TeV-pythia8	437504		0.0450	0.0509	0.0914	0.0902
QCD_Pt-80To120_MuEnrichedPt5_TuneCP5_13TeV-pythia8	106034		0.2087	0.2208	0.4299	0.4269
QCD_Pt-120To170_MuEnrichedPt5_TuneCP5_13TeV-pythia8	25191	LO	0.764	0.785	1.564	1.562
QCD_Pt-170To300_MuEnrichedPt5_TuneCP5_13TeV-pythia8	8654.5		4.244	4.252	8.443	8.323
QCD_Pt-300To470_MuEnrichedPt5_TuneCP5_13TeV-pythia8	797.4		37.12	37.70	73.49	73.71
QCD_Pt-470To600_MuEnrichedPt5_TuneCP5_13TeV-pythia8	79.03		254.7	255.4	503.8	489.0
QCD_Pt-600To800_MuEnrichedPt5_TuneCP5_13TeV-pythia8	25.10		783.4	779.2	1567.1	1533.3
QCD_Pt-800To1000_MuEnrichedPt5_TuneCP5_13TeV-pythia8	4.71		8429.8	8835.7	16606	16766
QCD_Pt-1000_MuEnrichedPt5_TuneCP5_13TeV-pythia8	1.62		8751.8	8785.0	16985	16917

Table 9: List of Background MC Samples with cross section, precision and effective luminosity.

3.3 Pileup

In the CMS detector, there are pileup events in one collision, and the profiles of pileup distribution are different run by run. In Fig. 11, the probability distributions of the true number of interactions are compared as pileup profiles for data and MC. In terms of MC generation, one of the reasons for separating the samples by runs is the different pileup profiles. The profiles of MC runs are provided in MixingModule of CMSSW by CMS collaboration. The MC pileup distributions are re-weighted to the nominal (69.2 mb) data pileup distribution and the variation of $\pm 1\sigma$ (72.4 mb , 66.0 mb) data pileup scenarios for systematic uncertainty.

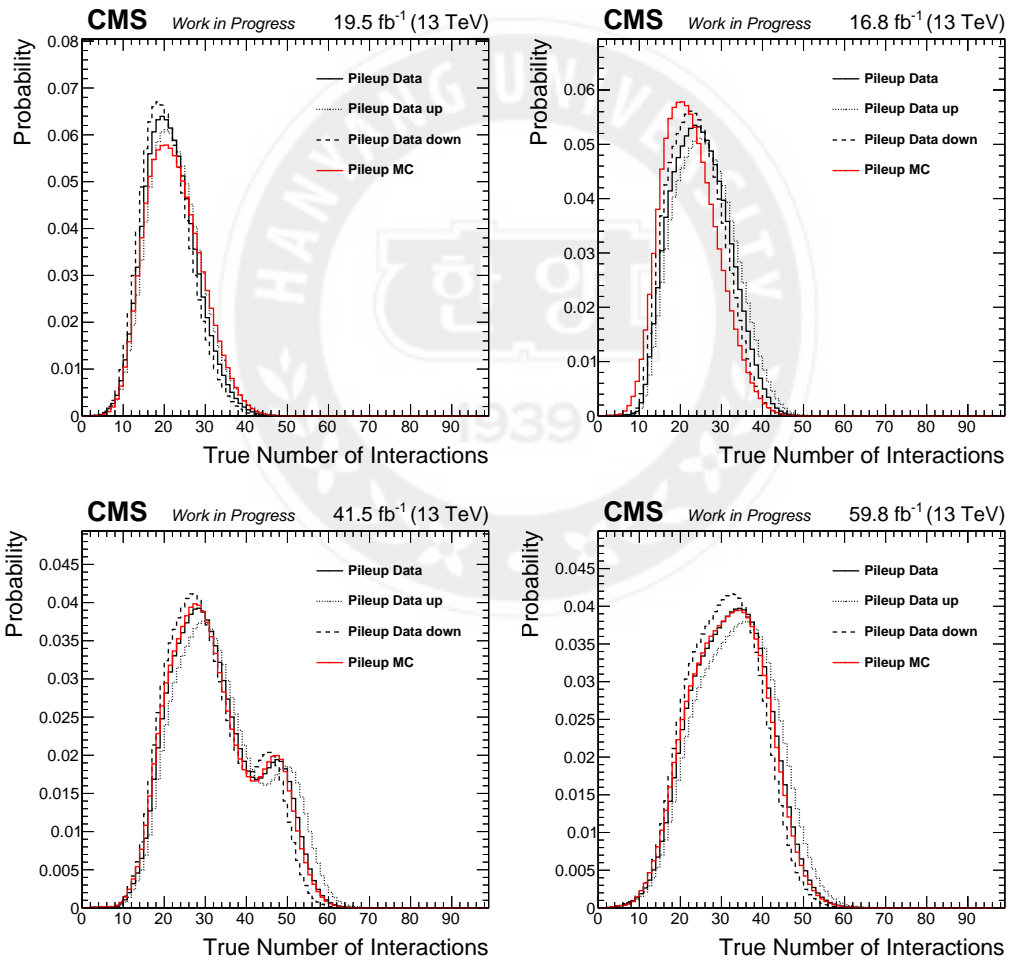


Figure 11: Comparison of Pileup distributions for data and MC in run 16APV (upper left), run 16 (upper right), run 17 (lower left) and run 18 (lower right)

4 Object and Event Selections

The CMS global event reconstruction [47] based on the particle-flow (PF) algorithm aims to reconstruct and identify each individual particle in an event by combining information from CMS subdetector information. The direction and the energy of particle objects are determined with the identification of particle types (photon, electron, muon, and charged and neutral hadron). In Section 2, the differences in the ST and $t\bar{t}$ LFV processes are checked through the generator level study. The object and event selections are separately applied to two event categories where each signal LFV process is enriched. We define **category 1** as ST LFV process enriched region and **category 2** as $t\bar{t}$ LFV process enriched region with the reconstructed mass of a selected muon and a selected tau. In the following sections, the definitions of object selections for the muon, tau, jet, b-tagging, and missing transverse momentum (MET) and event selections in several steps are introduced.

4.1 Object Selections

4.1.1 Muon

We initially select triggered events with an isolated muon HLT trigger in Table. 7, then the events contain at least one isolated loose muon. Among the muons in the events, we require kinematic requirements such as momentum p_T and pseudorapidity η to constrain the detector region into a barrel and obtain the highest signal significance (S/\sqrt{B}) compared to the background events. In this analysis, there are a muon from LFV interaction and we require $p_T > 50$ (30) GeV and $|\eta| < 2.4$ for the category 1 (category 2). Tight selection of identification (ID) for muon is applied, and its efficiency is about 96–97% [48]. The isolation (ISO) of the muon is calculated with $\delta\beta$ correction with the relative PF isolation using an isolation cone size of 0.4, and the selected muon is required to have less than 0.15. Also, we veto events with extra loose muons passing $p_T > 15$ GeV , $|\eta| < 2.4$, loose ID, and $Iso_\mu^{pf04} < 0.25$ to prevent any contamination by a muon decayed from W boson or decayed from a leptonic tau.

Dedicated p_T and η dependent scale factors are applied to the MC events in order to improve the agreement of the reconstruction, ID, and isolation efficiencies with the efficiencies in data, following the recommendations of the Muon POG. The scale factors of ID and

Isolation are not applied for veto muons. The muon trigger, ID, and isolation scale factors are provided by Muon POG in the CMS collaboration.

Muon Selections

- $p_T > 50 \text{ GeV}$ for the category 1 and $p_T > 30 \text{ GeV}$ for the category 2.
- $|\eta| < 2.4$, Tight ID, $Iso_\mu^{pf04} < 0.15$
- Loose muon $p_T > 15 \text{ GeV}$, $|\eta| < 2.4$, Loose ID, $Iso_\mu^{pf04} < 0.25$

4.1.2 Electron

There is no electron at the final states in the signal LFV processes, and the events with any loose electrons are rejected. The loose electrons are required to have $p_T > 15 \text{ GeV}$ and $|\eta| < 2.4$ with the veto ID of cut-based electron ID. The cut-based veto ID has an average efficiency of about 95%, and no additional impact parameter cuts are required for the veto ID.

Electron Selections

- Loose electron $p_T > 15 \text{ GeV}$, $|\eta| < 2.4$, cut-based Veto ID

4.1.3 Hadronic Tau

Tau decays leptonically into muon or electron and hadronically with a number of pions. This analysis focuses on the hadronic tau objects in the final state, where the portion of hadronic tau decay is about 60% of total tau decay processes. Hadronic tau (τ_h) objects are reconstructed and identified using hadrons-plus-strips (HPS) algorithm [49, 50] with particle flow candidates. The HPS algorithm reconstructs the 4-momentum of τ_h with PF neutral and charged hadrons and identifies τ_h from other leptons and jets. τ_h are seeded by jets reconstructed with the anti- k_T algorithm [51] with a distance parameter $\Delta R = 0.4$. DeepTauv2p1 is an algorithm for the τ_h identification [52] using DNN-based multi-classification and provides identification discriminators from jets, muons, and electrons. The kinematic requirements for tau are $p_T > 40$ (30) GeV and $|\eta| < 2.3$ for the category 1 (category 2). In order to identify τ_h with the DeepTauv2p1 algorithm, the 1- and 3-prong tau decay modes are selected, rejecting the 2-prong tau decay mode. Working point (WP)

based DeepTauv2p1 ID selections are required for taus, and there are three kinds of the IDs – against jet ID, muon ID, and electron ID. The $t\bar{t}$ and LFV signal processes have large jet multiplicity. Thus we require **very tight** (**medium**) for against jet ID for the category 1 (category 2). **Tight** for against muon ID and **very loose** for against electron ID are required for selected taus. If the τ_h objects are overlapped with the selected muon in $R = 0.4$, then overlapped taus are not selected.

Scale factors for DeepTauv2p1 IDs are provided by Tau POG of CMS collaboration and are obtained for the selected τ_h . The pt-binned scale factor against jet ID is applied on the genuine τ_h , which is gen-matched. Also, against electron and muon ID eta-binned scale factors for the fake τ_h into electron or muon are required to $e \rightarrow \tau_h$ and $\mu \rightarrow \tau_h$ fake taus. Tau energy scale (TES) is multiplied on p_T , energy, and mass of τ_h to correct shape distributions for genuine taus. Fake $e \rightarrow \tau_h$ tau energy scale (FES) is also applied to τ_h faked by electrons.

Hadronic Tau Selections

- $p_T > 40 \text{ GeV}$ for the category 1 and $p_T > 30 \text{ GeV}$ for the category 2.
- $|\eta| < 2.3$ and decay mode selection (1 and 3-prong hadronic tau).
- For the category 1, **Very tight** vs. Jet ID, **Tight** vs. Muon ID, **Very loose** vs. Electron ID.
- For the category 2, **Medium** vs. Jet ID, **Tight** vs. Muon ID, **Very loose** vs. Electron ID.

4.1.4 Jet

Particle flow (PF) jet candidates go through charged hadron subtraction, and charged particles from pileup are removed in this step (PFCHS jet). Then, the anti- k_T algorithm is used for clustering with a distance parameter $\Delta R = 0.4$ (AK4 jet). We require jets to pass the **tight lepton veto** ID and to have $p_T > 40$ (30) GeV and $|\eta| < 2.4$ for the category 1 (category 2). When the jets are overlapped with the selected muon or tau in $R = 0.4$, the overlapped jets are not selected for the analysis. Jet energy correction (JEC) is applied on both data and MC to scale the p_T of jet, E_T^{miss} , and ϕ of E_T^{miss} . JEC global tags for each era are Summer19UL16APV_V7, Summer19UL16_V7, Summer19UL17_V5, and Summer19UL18_V5 for run 16APV, 16, 17, and 18, respectively.

Jet Selections

- $p_T > 30 \text{ GeV}$, $|\eta| < 2.4$, Tight Lepton Veto ID

b-tagging We use the DeepJet algorithm to identify jets originating from b-quark decays. Jets are tagged as b-tagged jet where b-tagging discriminator values are larger than medium working point criteria (0.2598, 0.2489, 0.3040 and 0.2783 for 16APV, 16, 17, 18, respectively). The distribution of the b-tagging discriminator is re-calibrated with b-tagging scale factors obtained from the selected jets that are processed with overlap removal of jets from the selected muon or tau. The re-calibration of the b-tagging discriminator is implemented by applying weights (b-tagging scale factor) to the events. The number of events before and after applying the b-tagging scale factor are made to be conserved before b-tagged jet selection. The b-tagging scale factors are provided by BTV POG in CMS collaboration.

Medium WP of DeepJet b-tagging Algorithm

- Run 16APV : B-tag discriminator of a jet > 0.2598
- Run 16 : B-tag discriminator of a jet > 0.2489
- Run 17 : B-tag discriminator of a jet > 0.3040
- Run 18 : B-tag discriminator of a jet > 0.2783

4.1.5 Missing Transverse Energy (MET)

The missing transverse energy (E_T^{miss}) is defined as the magnitude of the negative vector sum of all visible particles, based on the momentum conservation. The type 1 correction is applied on MET, and the E_T^{miss} and ϕ of E_T^{miss} are scaled for JEC with jet objects as mentioned above. MET is exclusively required for the category 2 to reach a higher significance for the $t\bar{t}$ LFV signal compared to the SM $t\bar{t}$ backgrounds. And prior to the event selection, MET filters provided by JetMET POG in CMS collaboration are applied to clean the events with noises (HB: HCAL Barrel, HE: HCAL Endcap, TP: Trigger Primitive, PF: Particle Flow, SC: SuperCluster).

List of MET Filters

- Primary Vertex Filter
- Beam Halo Filter
- HBHE Noise Filter
- HBHEiso Noise Filter
- ECAL TP Filter
- Bad PF Muon Filter
- ee BadSC Noise Filter
- ECAL bad Calib. Filter (run 17/18)

4.2 Event Selections

Baseline selection is established based on the final particles of LFV signal processes. Both ST and $t\bar{t}$ LFV signal processes are required to have one muon and one hadronic tau from LFV interaction and one b-tagged jet from the SM top decay in common. The main differences between ST and $t\bar{t}$ LFV processes come from jet multiplicity and reconstructed kinematic variables. From the gen-level study in Section 2, a distinguishable variable separating the ST and $t\bar{t}$ LFV is reconstructed visible mass of a muon and a tau ($m_{\mu\tau}$). The events are divided into two categories to improve the signal significance, with $m_{\mu\tau}$ criteria of 150 GeV as introduced at the beginning of this section. The criteria for $m_{\mu\tau} = 150 \text{ GeV}$ is set with consideration of the mass of top quark mass and the products from top quark decay. The events in the category 1 is required to have $m_{\mu\tau} > 150 \text{ GeV}$ and $m_{\mu\tau} \leq 150 \text{ GeV}$ for the category 2. The following definitions are the event selections for the category 1 and 2.

Category 1 (ST LFV enriched region) selection steps

- S1 Select events with exactly one muon. Veto events with extra leptons.
- S2 Select events with exactly one τ_h after removing overlap with the muon.
- S3 $m_{\mu\tau} > 150 \text{ GeV}$, OS (opposite sign) selected muon and tau.
- S4 Remove jets overlapping with a muon and τ_h and select at least 3 jets.
- S5 Select events with exactly one b-tagged jet.

Category 2 (TT LFV enriched region) selection steps

- S1 Select events with exactly one muon. Veto events with extra leptons.
- S2 Select events with exactly one τ_h after removing overlap with the muon.

S3 $m_{\mu\tau} \leq 150 \text{ GeV}$, OS (opposite sign) selected muon and tau.

S4 Remove jets overlapping with a muon and τ_h and select at least 4 jets.

S5 Select events with exactly one b-tagged jet.

S6 $10 \text{ GeV} < E_T^{\text{miss}} < 70 \text{ GeV}$.

5 Data and MC Comparison

Data and MC events are compared for full run 2 (16APV, 16, 17, and 18 are in Appendix) through the event selection established in Section 4. In this section, the comparison histograms for data and MC are shown in the different event selection steps for both categories. Kinematic distributions of the selected muon, tau, jets, b-tagged jets, and E_T^{miss} are compared, as well as the distributions of reconstructed m_T with muon and E_T^{miss} , and reconstructed variables with the muon and tau ($m_{\mu\tau_h}$, $\Delta R_{\mu\tau_h}$). Distributions after the event selections are used as inputs of top mass reconstruction in Section 6 and signal extraction in Section 7. More control plots excluded in this section are attached in Appendix I.

Descriptions for Histogram Legends

Data	Observed data events.
TT-di	SM $t\bar{t}$ Di-leptonic MC events.
TT-semi	SM $t\bar{t}$ Semi-leptonic MC events.
W+Jets	SM W+jets MC events.
Z+Jets	SM DY (Z+jets) MC events.
Others	SM $t\bar{t}$ hadronic, $t\bar{t}+X$ (W or Z), and di-boson MC events.
QCD	SM QCD MC events.
LFV ¹	LFV signal MC events. Only vector-like operator events are drawn. "LFV STc" means ST LFV events with $t\bar{c}\mu\tau$ interaction. Category 2 signals are multiplied by 50 for visibility.

5.1 Comparison for the Category 1 (ST LFV enriched region)

Histograms during Event Selections

This section displays several histograms for data and MC comparison in the category 1 for different event selection steps. In Fig. 12, distributions of ΔR and mass reconstructed with a muon and tau are compared after the step 2 (S2) of event selections before $m_{\mu\tau} > 150 \text{ GeV}$ selection at step 3 (S3). In Fig. 13 and 14, distributions related to the muon and tau are compared after the step 3 of event selections (S3). And, in Fig. 15, the number of jets and b-tagged jets distribution is shown after step 3 (S3) and step 4 (S4), respectively, where we observe overlaid signal distribution becomes dominant in the selected regions. After the step 4 selection, the distributions of p_T and η of the leading and sub-leading jets in the higher p_T order are in Fig. 16.

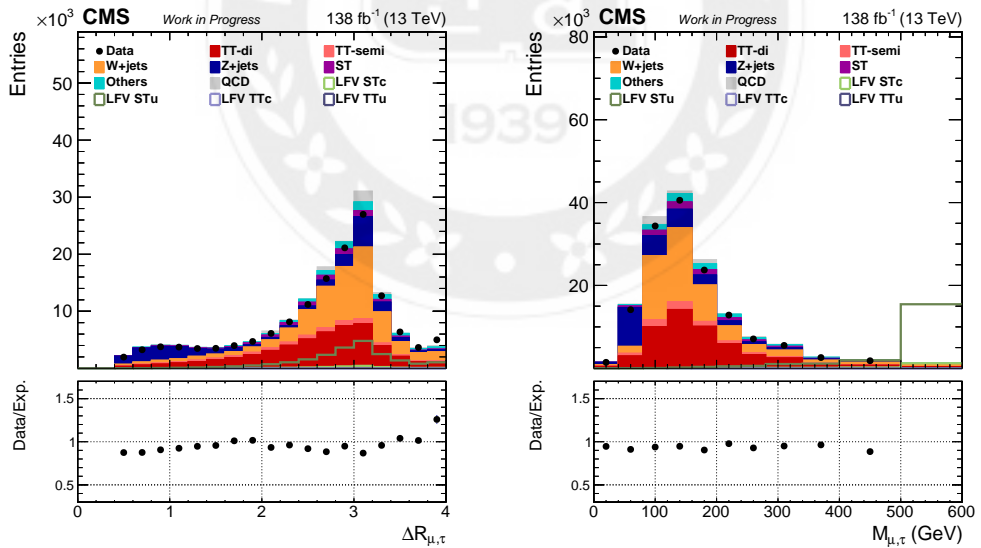


Figure 12: Data/MC comparison histograms in the category 1 after S2. ΔR (left) and mass (right) reconstructed with a muon and tau.

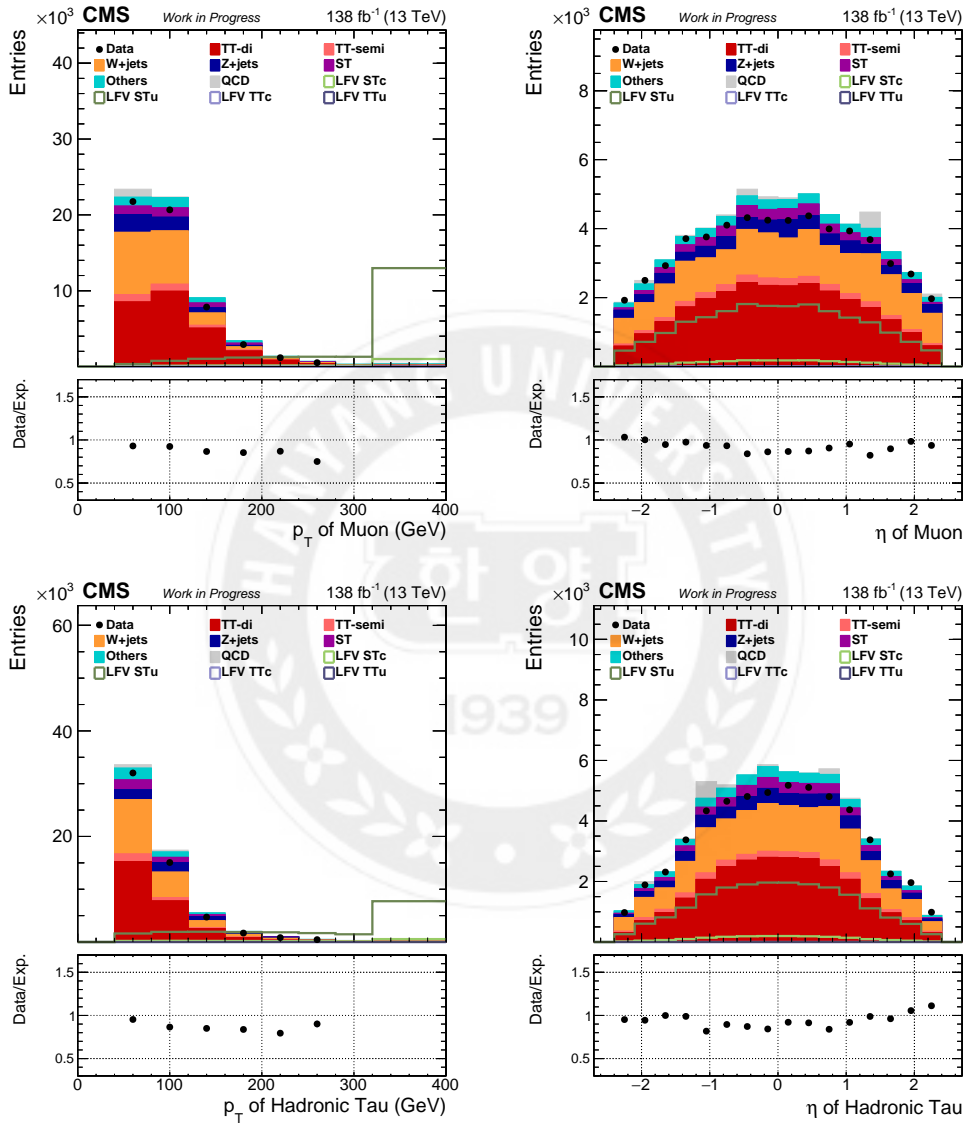


Figure 13: Data/MC comparison histograms in the category 1 after S3. p_T (left column) and η (right column) distributions for muon (upper row) and tau (lower row).

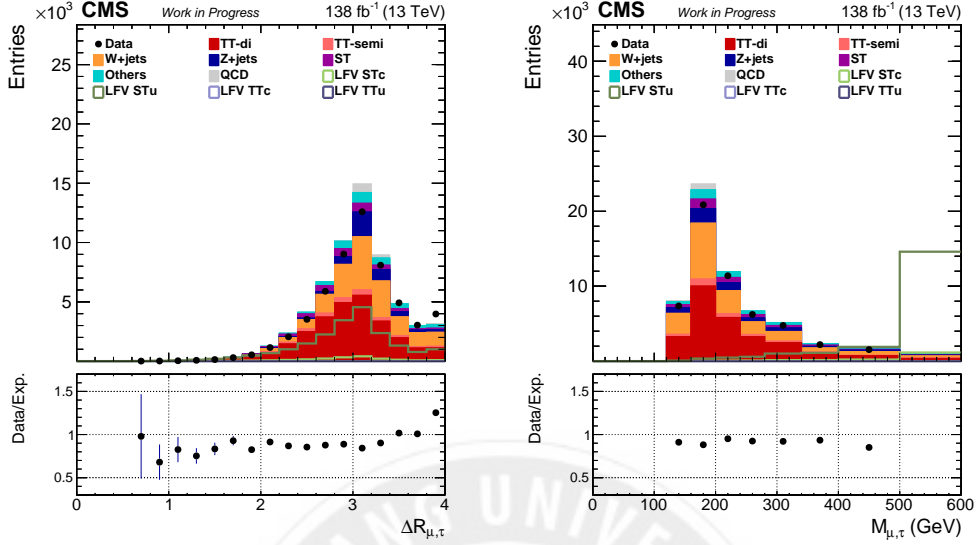


Figure 14: Data/MC comparison histograms in the category 1 after S3. ΔR (left) and mass (right) distributions reconstructed with the muon and tau.

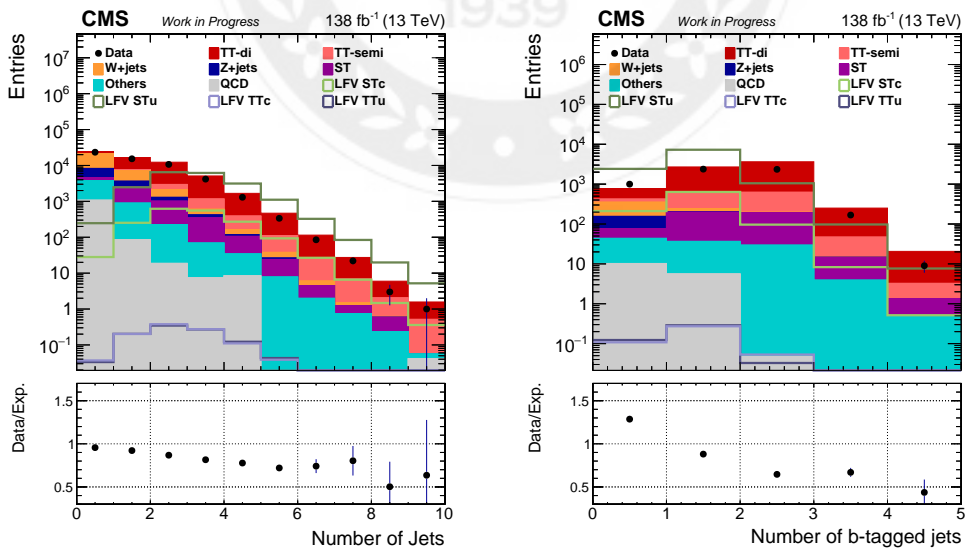


Figure 15: Data/MC comparison histograms in the category 1 for jet multiplicity distribution (left) after S3 and b-tagged jet multiplicity distribution (right) after S4.

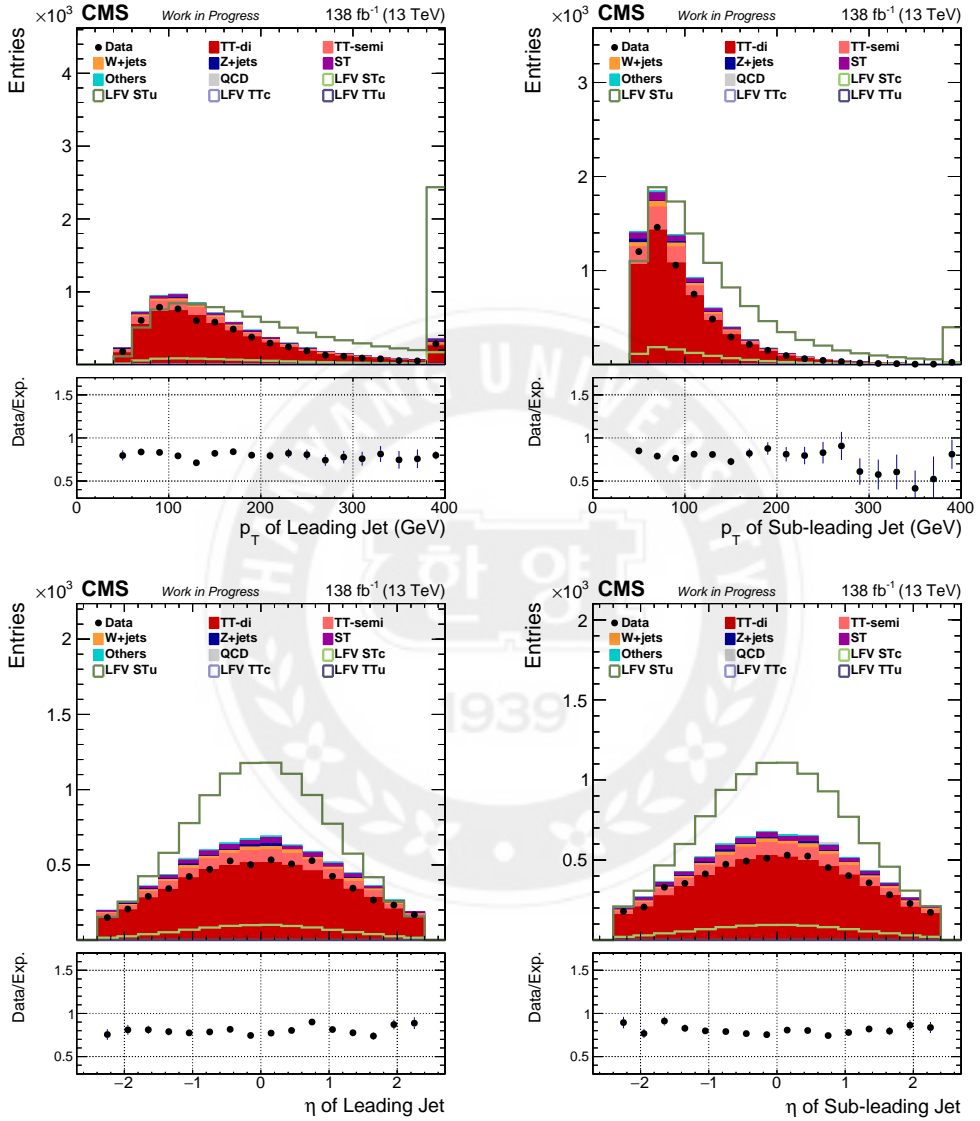


Figure 16: Data/MC comparison histograms in the category 1 after S4. p_T (upper row) and η (lower row) distributions of the leading (left column) and sub-leading jets (right column).

Final selection histograms (S5)

From Fig. 17 to 20, distributions after event selection (S5) are compared. The data is blinded where the signal is clearly dominant over the backgrounds.

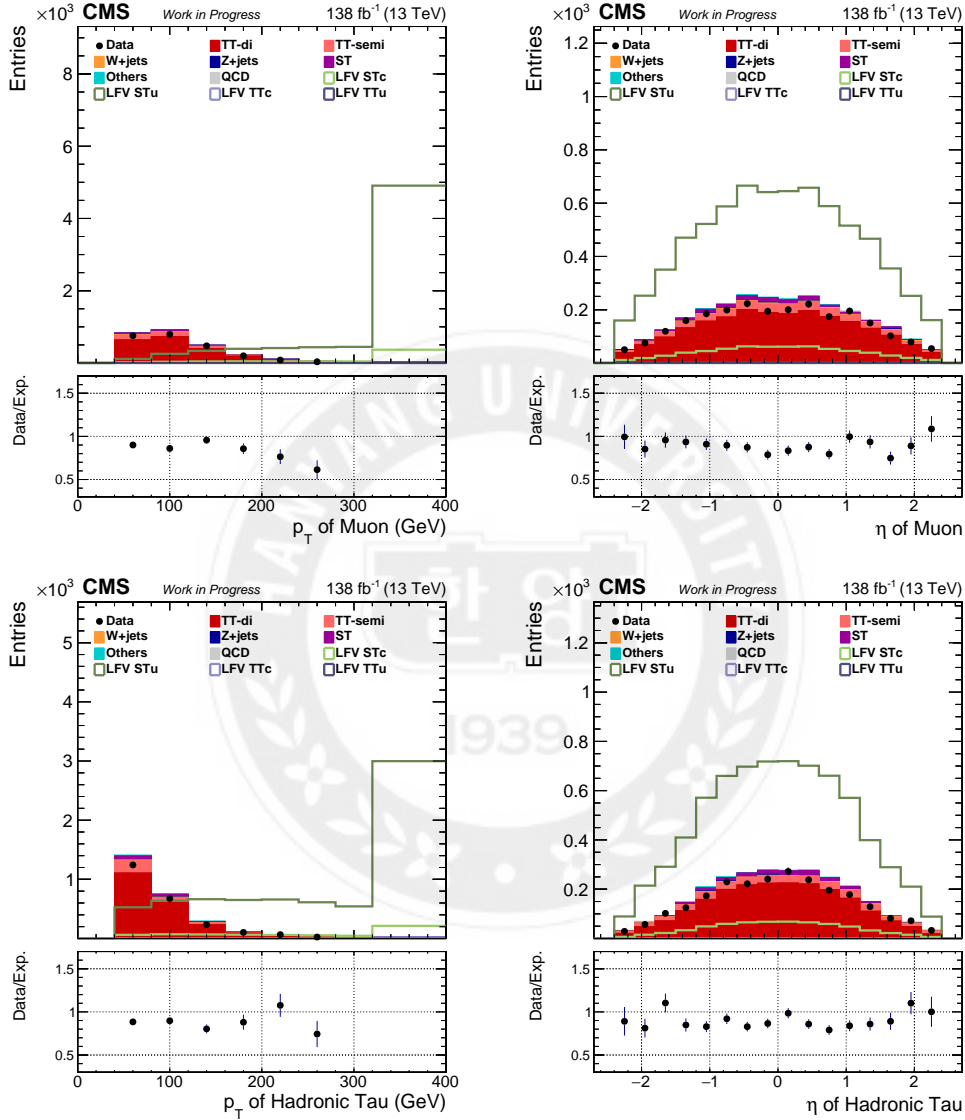


Figure 17: Data/MC comparison histograms in the category 1 after S5 (final). p_T (left column) and η (right column) distributions for muon (upper row) and tau (lower row).

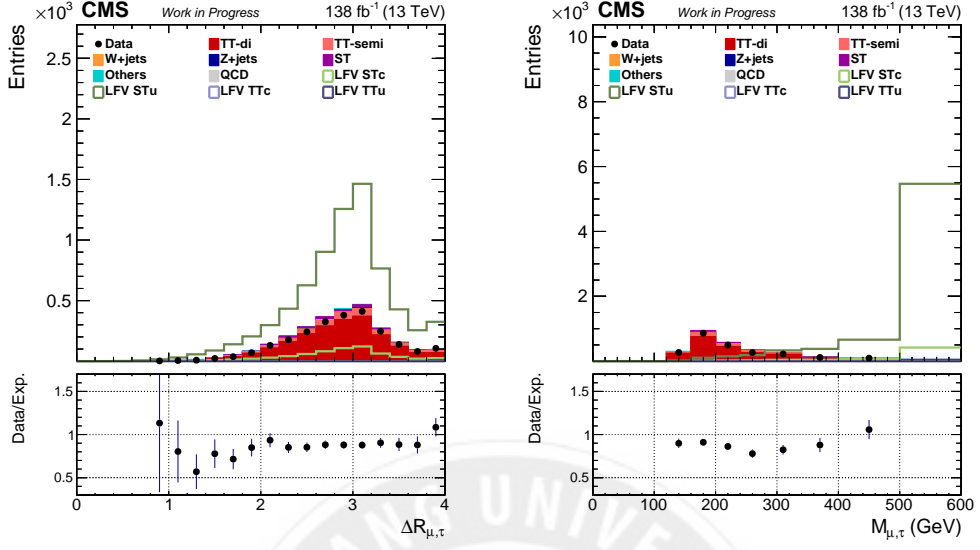


Figure 18: Data/MC comparison histograms in the category 1 after S5 (final). ΔR (left) and mass (right) distributions reconstructed with the muon and tau.

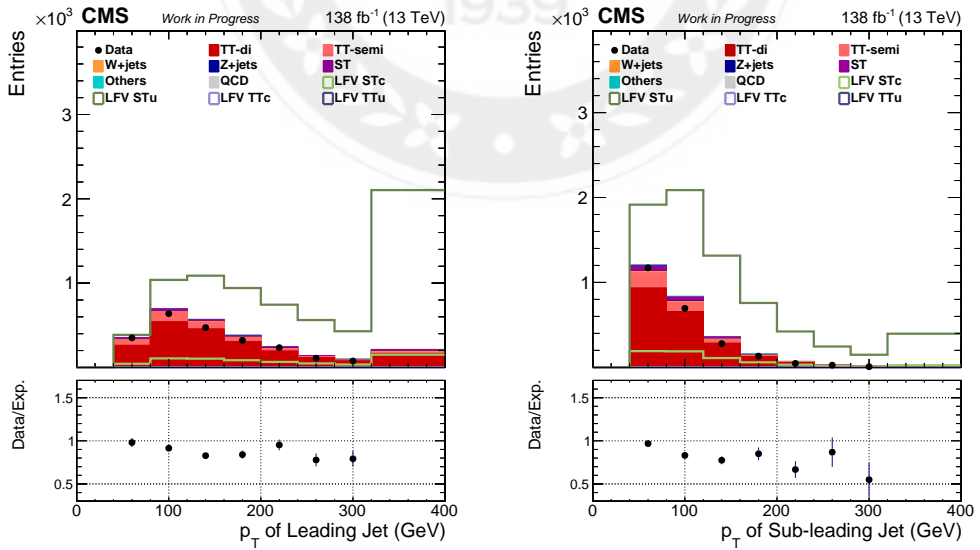


Figure 19: Data/MC comparison histograms in the category 1 after S5 (final). p_T distributions of the leading (left) and sub-leading jets (right).

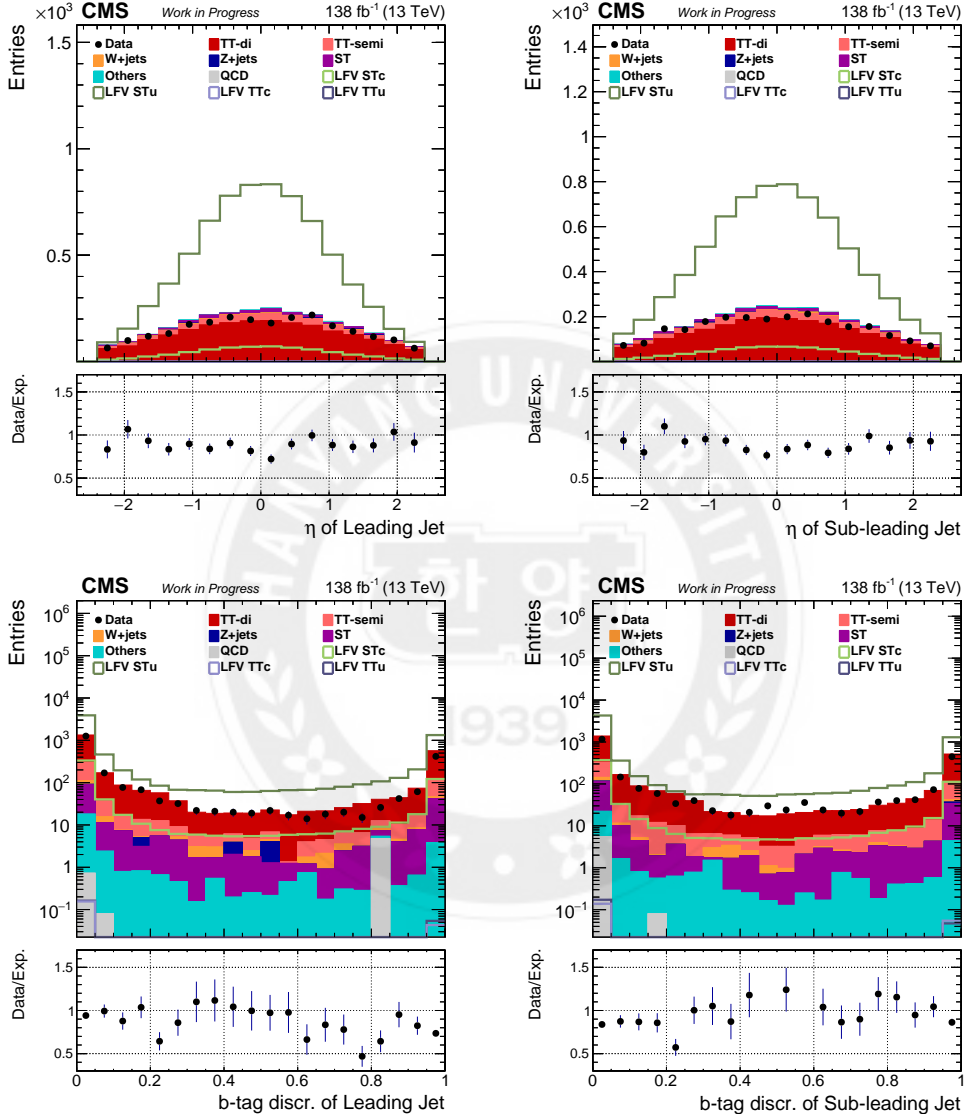


Figure 20: Data/MC comparison histograms in the category 1 after S5 (final). η (upper row) and b-tagging discriminator (lower row) distributions of the leading (left column) and sub-leading jets (right column).

5.2 Comparison for the Category 2 (TT LFV enriched region)

Histograms during Event Selections

This section displays several histograms for data and MC comparison in the category 2 for different event selection steps. In Fig. 21, distributions of ΔR and mass reconstructed with a muon and tau are compared after the step 2 (S2) of event selections before $m_{\mu\tau} > 150 \text{ GeV}$ selection at step 3 (S3). In Fig. 22 and 23, distributions related to the muon and tau are compared after the step 3 of event selections (S3). And, in Fig. 24, the number of jets and b-tagged jets distribution is shown after step 3 (S3) and step 4 (S4), respectively, as in the category 1. After the step 4 selection, the distributions of p_T and η of the leading and sub-leading jets in the higher p_T order are in Fig. 25.

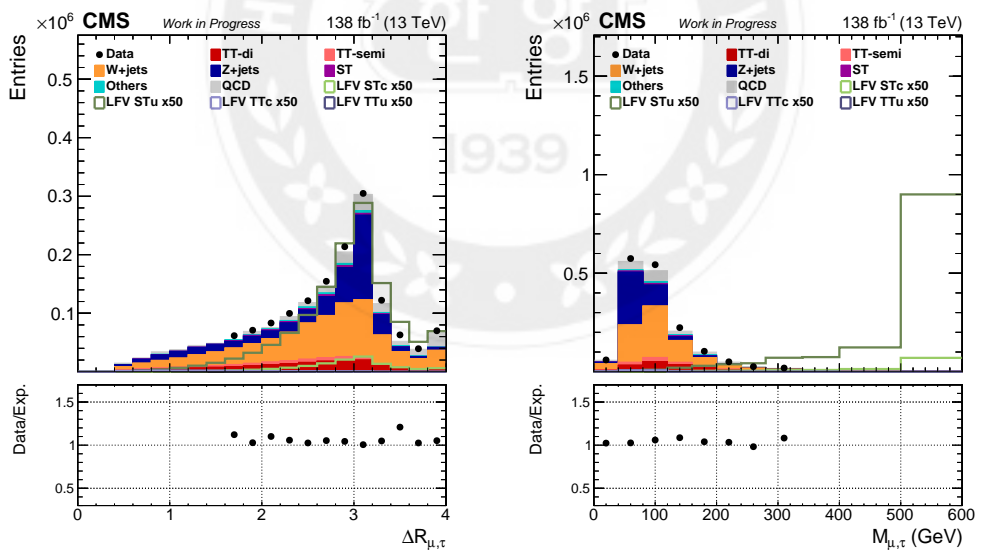


Figure 21: Data/MC comparison histograms in the category 2 after S2. ΔR (left) and mass (right) reconstructed with a muon and tau.

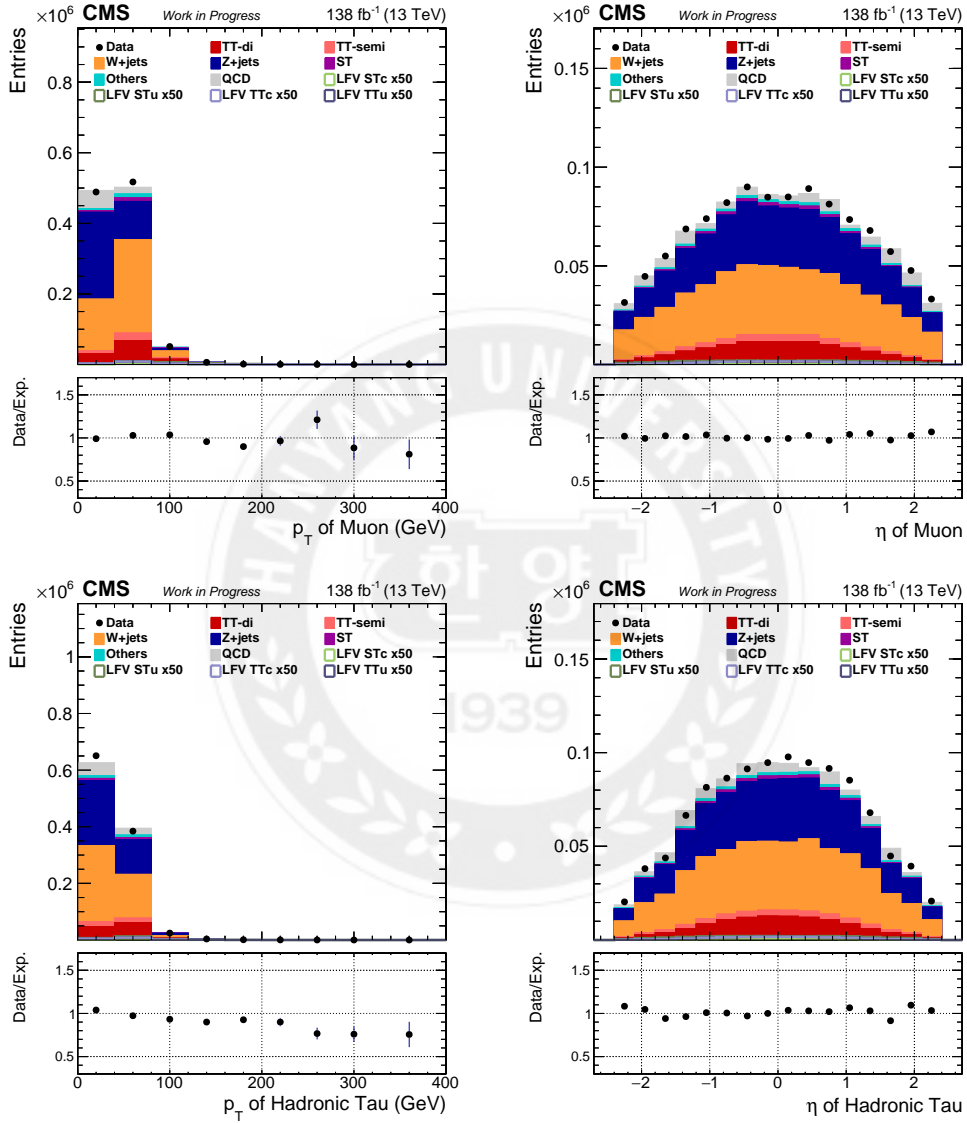


Figure 22: Data/MC comparison histograms in the category 2 after S3. p_T (left column) and η (right column) distributions for muon (upper row) and tau (lower row).

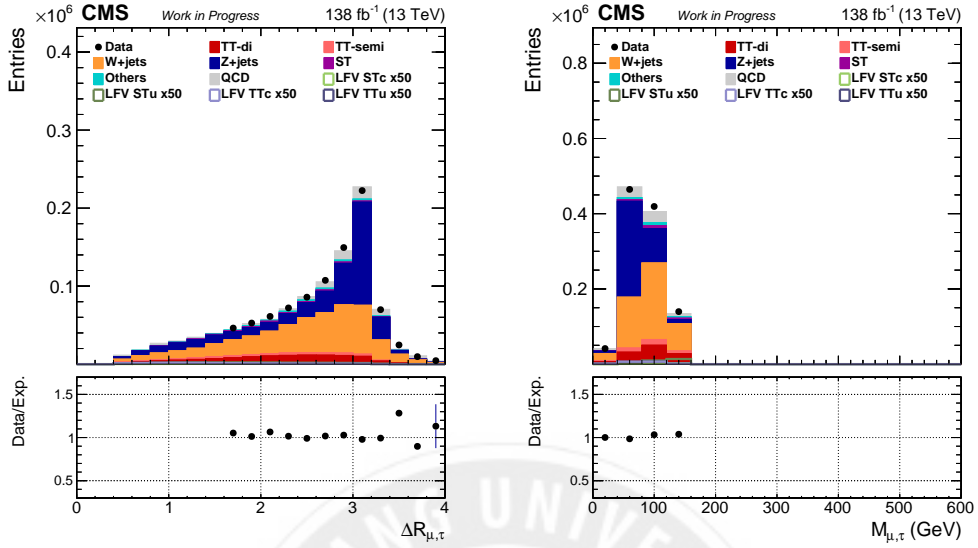


Figure 23: Data/MC comparison histograms in the category 2 after S3. ΔR (left) and mass (right) distributions reconstructed with the muon and tau.

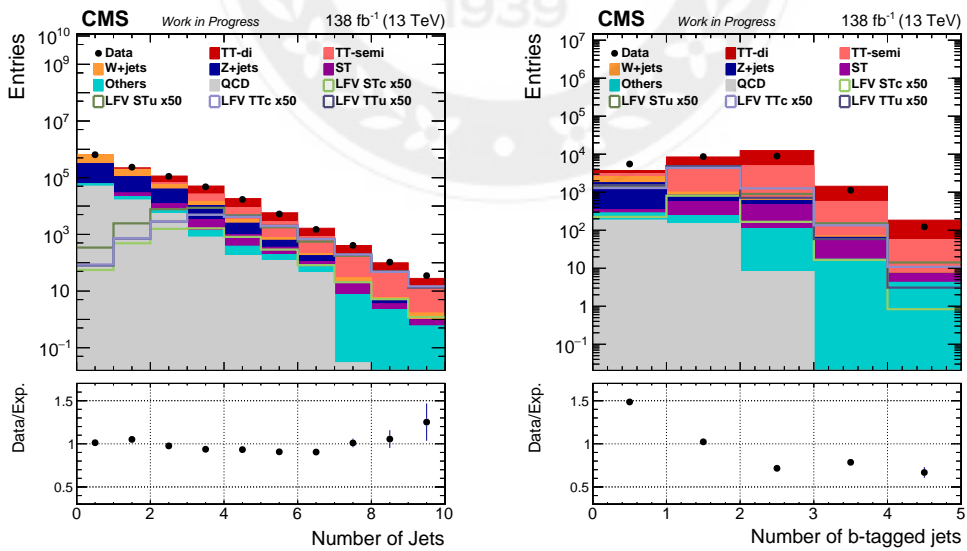


Figure 24: Data/MC comparison histograms in the category 2 for jet multiplicity distribution (left) after S3 and b-tagged jet multiplicity distribution (right) after S4.

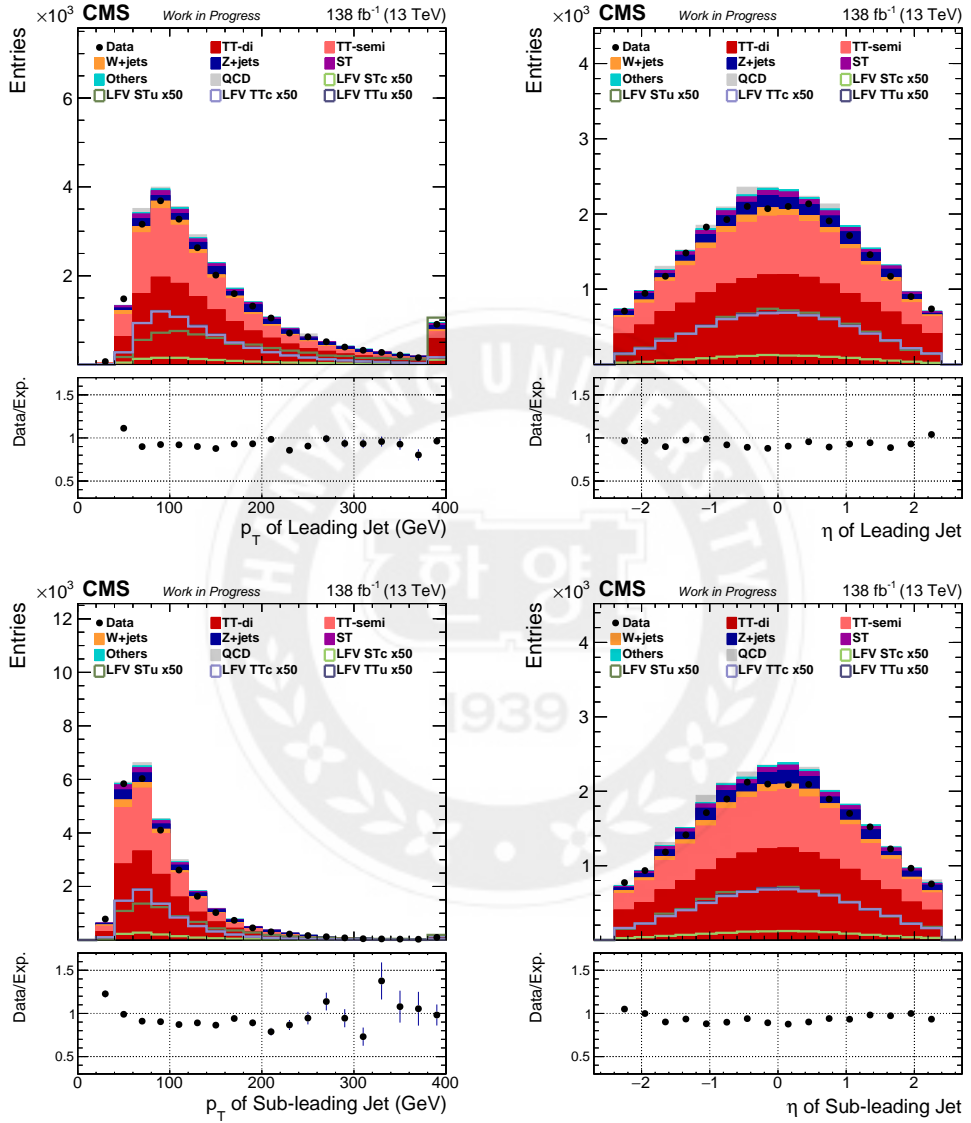


Figure 25: Data/MC comparison histograms in the category 2 after S4. p_T (left column) and η (right column) distributions of the leading (upper row) and sub-leading jets (lower row).

Final selection histograms (S6)

From Fig. 26 to 29, distributions after event selection (S6) are compared. The data is blinded where the LFV signal is clearly dominant.

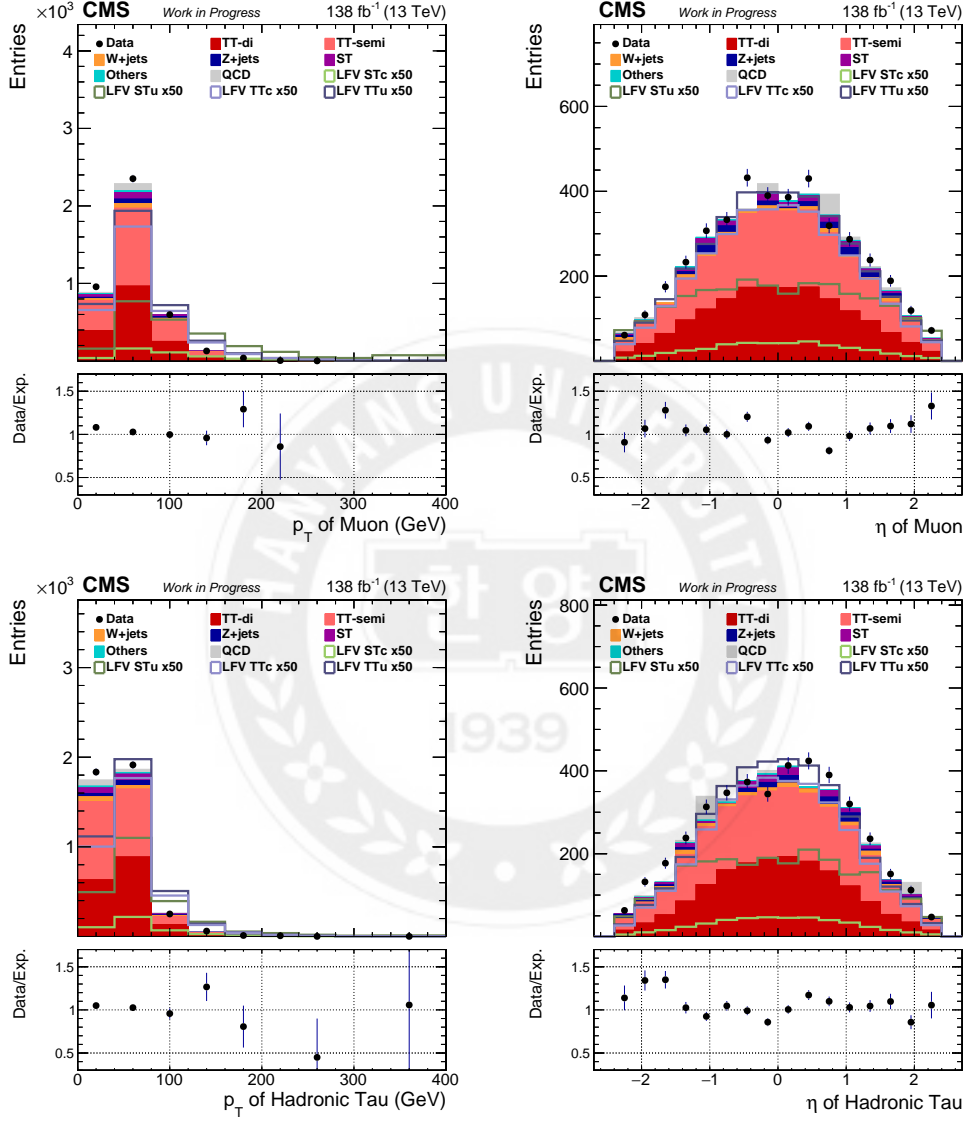


Figure 26: Data/MC comparison histograms in the category 2 after S6 (final). p_T (left column) and η (right column) distributions for muon (upper row) and tau (lower row).

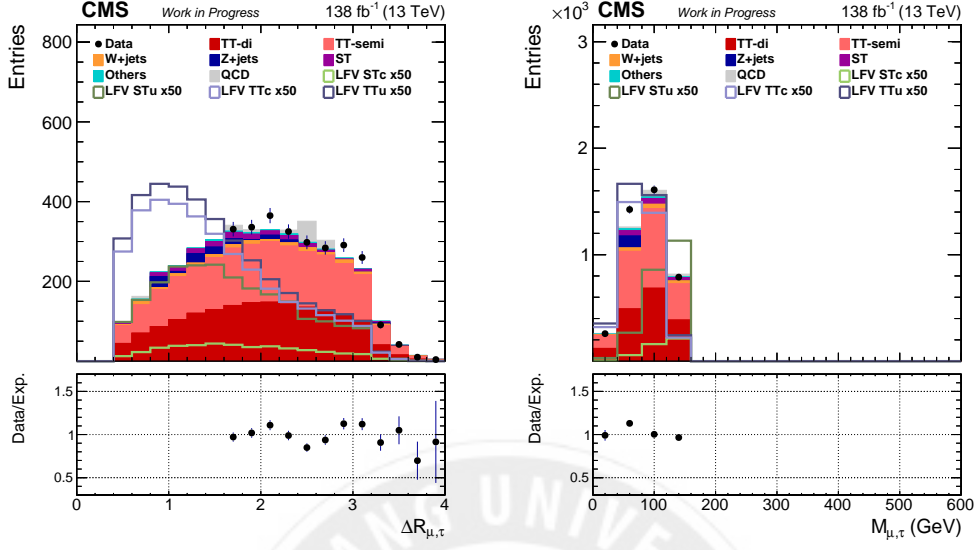


Figure 27: Data/MC comparison histograms in the category 2 after S6 (final). ΔR (left) and mass (right) distributions reconstructed with the muon and tau.

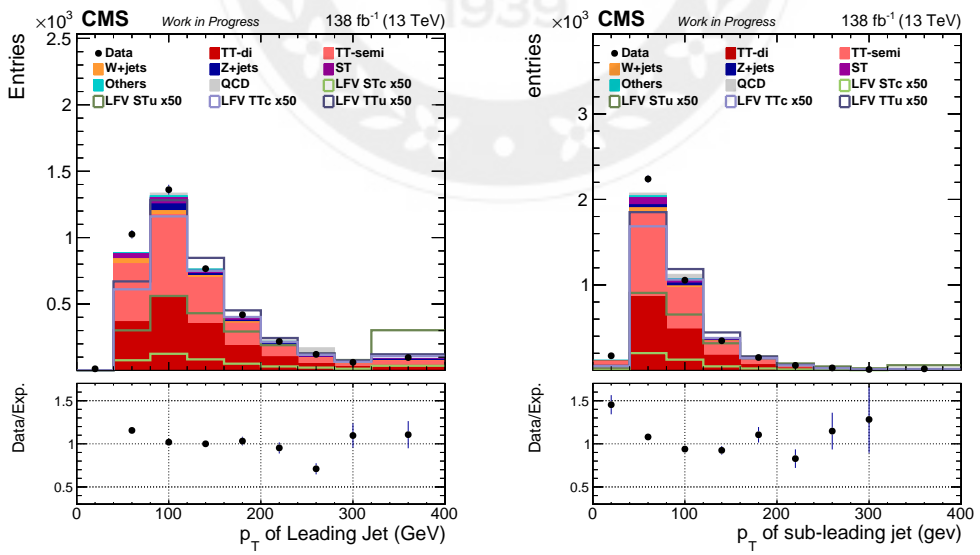


Figure 28: Data/MC comparison histograms in the category 2 after S6 (final). p_T distributions of the leading (left) and sub-leading jets (right).

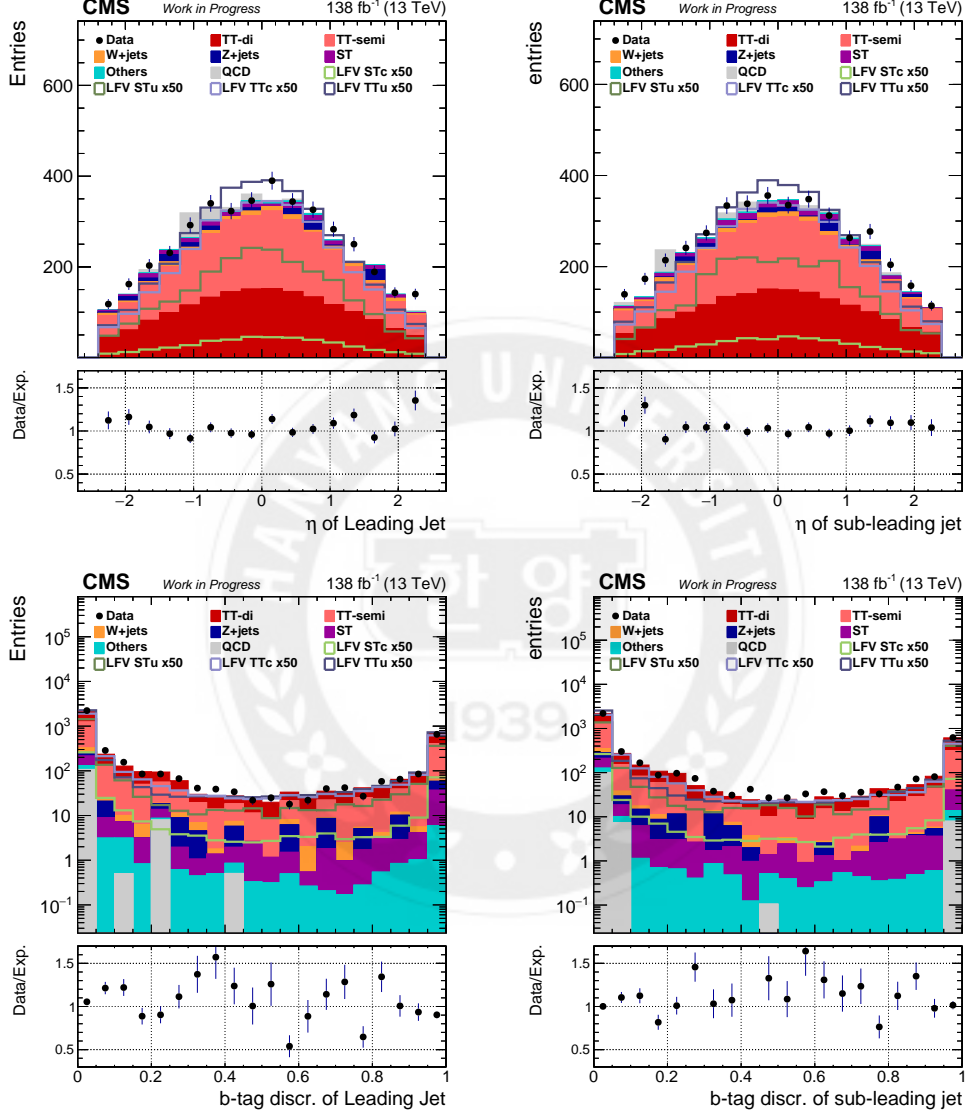


Figure 29: Data/MC comparison histograms in the category 2 after S6 (final). η (upper row) and b-tagging discriminator (lower row) distributions of the leading (left column) and sub-leading jets (right column).

5.3 Cutflow Table for Run2

Cutflow table in Table. 10 and 11 are containing the normalized events with the event selection steps. The signal event yields are in the top part of the cutflow table, and the background MC event yields for different processes are in the middle part of the cutflow. And only vector-like signal events are shown in the cutflow table. The ratio of the data and MC is calculated by dividing the number of data by the number of total MC events. In the bottom part of the cutflow table, the significance of the signal (S/\sqrt{B}) with respect to the total backgrounds of MC events and the acceptance of the signal events during the event selections. The statistical uncertainties for the signal and background MC events are included with the error propagation.

The cutflow table for the category 1 is in Table. 10. After the event selection, most of the SM background events are $t\bar{t}$ events as expected. The signal acceptance of the $t\bar{t}$ LFV process in the category 1 is suppressed compared to ST LFV processes after the event selection. In Table. 11, the acceptance of ST LFV signal processes is suppressed in the category 2. As in the category 1, the $t\bar{t}$ process is the main background for the category 2, and, from the data/mc histograms, the signal distributions are similar to the SM $t\bar{t}$ processes leading into irreducible backgrounds.

Run2 (138 fb^{-1})	S1	S2	S3	S4	S5
LFV ST $t c \mu \tau$	$3,118 \pm 1.16$	$1,058 \pm 0.673$	993 ± 0.653	510 ± 0.468	341 ± 0.372
LFV ST $t u \mu \tau$	$32,828 \pm 12.2$	$11,413 \pm 7.18$	$10,748 \pm 6.97$	$5,818 \pm 5.13$	$3,899 \pm 4.09$
LFV TT $t c \mu \tau$	963 ± 0.560	51.7 ± 0.130	0.563 ± 0.014	0.234 ± 0.009	0.144 ± 0.007
LFV TT $t u \mu \tau$	969 ± 0.514	52.1 ± 0.119	0.548 ± 0.012	0.238 ± 0.008	0.154 ± 0.006
$t\bar{t}$ dileptonic	$1,810,647 \pm 260$	$51,822 \pm 44$	$26,958 \pm 31.8$	$5,698 \pm 14.6$	$2,103 \pm 9.47$
$t\bar{t}$ semileptonic	$5,233,509 \pm 494$	$7,065 \pm 18.1$	$2,466 \pm 10.7$	884 ± 6.43	354 ± 4.29
$t\bar{t}$ hadronic	$5,933 \pm 20.4$	12 ± 0.922	2.15 ± 0.401	1.19 ± 0.290	0.666 ± 0.204
DY	$10,167,245 \pm 7,368$	$24,682 \pm 350$	$5,196 \pm 146$	84.3 ± 19.8	5.93 ± 5.9
Single Top	$1,457,724 \pm 512$	$6,728 \pm 45.6$	$3,526 \pm 33.3$	368 ± 10.9	161 ± 7.6
W+Jets	$99,962,292 \pm 51,554$	$53,108 \pm 1,053$	$17,651 \pm 516$	242 ± 8.43	41.3 ± 3.32
$t\bar{t} + X$	$15,201 \pm 19.5$	271 ± 2.09	103 ± 1.46	57.6 ± 1.16	22.6 ± 0.808
VV	$847,590 \pm 522$	$7,225 \pm 49$	$3,711 \pm 35.4$	39.4 ± 3.64	7.78 ± 1.65
QCD	$10,121,748 \pm 60,976$	$4,413 \pm 1,173$	$1,195 \pm 487$	15.9 ± 8.84	5.59 ± 4.94
Total MC	$129,621,889 \pm 80,194$	$155,327 \pm 1,617$	$60,808 \pm 727$	$7,391 \pm 30.5$	$2,701 \pm 15.5$
DATA	$145,225,850$	$145,383$	$55,321$	$5,908$	$2,379$
DATA / MC	1.12 ± 0.00	0.94 ± 0.01	0.91 ± 0.01	0.80 ± 0.01	0.88 ± 0.01
S/\sqrt{B} (ST $t c \mu \tau$)	0.056	0.599	0.906	1.33	1.44
S/\sqrt{B} (ST $t u \mu \tau$)	0.622	6.71	10.12	15.53	17.13
S/\sqrt{B} (TT $t c \mu \tau$)	0.012	0.019	0.000	0.000	0.000
S/\sqrt{B} (TT $t u \mu \tau$)	0.012	0.019	0.000	0.000	0.001
Acceptance (ST $t c \mu \tau$)	0.616	0.209	0.196	0.101	0.067
Acceptance (ST $t u \mu \tau$)	0.607	0.211	0.199	0.108	0.072
Acceptance (TT $t c \mu \tau$)	0.326	0.017	0.000	0.000	0.000
Acceptance (TT $t u \mu \tau$)	0.327	0.018	0.000	0.000	0.000

Table 10: Cutflow Table for Run2 data and MC samples in the category 1.

Run2 ($138 fb^{-1}$)	S1	S2	S3	S4	S5	S6
LFV ST $t c \mu \tau$	$3,200 \pm 1.17$	$1,339 \pm 0.758$	53 ± 0.151	13.1 ± 0.075	8.67 ± 0.060	4.65 ± 0.044
LFV ST $t \bar{t} \mu \tau$	$33,368 \pm 12.3$	$14,094 \pm 7.98$	284 ± 1.13	78.7 ± 0.595	52.1 ± 0.478	24.5 ± 0.329
LFV TT $t c \mu \tau$	$1,369 \pm 0.667$	176 ± 0.240	167 ± 0.234	75.6 ± 0.157	46.8 ± 0.122	36.7 ± 0.108
LFV TT $t \bar{t} \mu \tau$	$1,375 \pm 0.612$	178 ± 0.220	169 ± 0.214	76.6 ± 0.144	51.8 ± 0.116	40.9 ± 0.103
$t\bar{t}$ dileptonic	$2,977,333 \pm 333$	$170,195 \pm 79.7$	$116,309 \pm 65.8$	$13,617 \pm 22.5$	$4,429 \pm 13.7$	$1,678 \pm 8.42$
$t\bar{t}$ semileptonic	$8,535,807 \pm 631$	$61,932 \pm 53.7$	$35,704 \pm 40.7$	$8,403 \pm 19.8$	$3,042 \pm 12.6$	$1,747 \pm 9.54$
$t\bar{t}$ hadronic	$15,401 \pm 32.7$	177 ± 3.51	84 ± 2.42	30 ± 1.45	17.6 ± 1.1	14.3 ± 0.995
DY	$50,407,674 \pm 14,682$	$414,724 \pm 1.313$	$362,770 \pm 1.195$	$1,815 \pm 107$	260 ± 43.3	99 ± 31.4
Single Top	$2,731,104 \pm 660$	$27,625 \pm 87.8$	$17,265 \pm 70.3$	791 ± 15.5	328 ± 10.5	152 ± 7.13
W+Jets	$860,836,898 \pm 166,791$	$685,505 \pm 4,224$	$430,854 \pm 3,424$	$1,000 \pm 40.4$	168 ± 8.48	107 ± 7.07
$t\bar{t} + X$	$22,792 \pm 23.8$	851 ± 3.9	391 ± 2.83	172 ± 2.04	56.1 ± 1.31	21.9 ± 0.809
VV	$1,759,212 \pm 752$	$28,936 \pm 97.2$	$18,005 \pm 77.1$	113 ± 5.82	18.9 ± 2.34	6.14 ± 1.3
QCD	$96,887,852 \pm 302,669$	$154,442 \pm 10,284$	$71,959 \pm 7,177$	338 ± 124	147 ± 55.8	116 ± 49.1
Total MC	$1,024,174,072 \pm 345,897$	$1,544,387 \pm 11,197$	$1,053,341 \pm 8,042$	$26,277 \pm 172$	$8,467 \pm 74.3$	$3,942 \pm 60.5$
DATA	$971,102,378$	$1,615,240$	$1,064,976$	$24,369$	$8,662$	$4,080$
DATA / MC	0.95 ± 0.00	1.05 ± 0.01	1.01 ± 0.01	0.93 ± 0.01	1.02 ± 0.01	1.04 ± 0.01
S/\sqrt{B} (ST $t c \mu \tau$)	0.020	0.233	0.005	0.009	0.010	0.007
S/\sqrt{B} (ST $t \bar{t} \mu \tau$)	0.224	2.57	0.029	0.052	0.063	0.041
S/\sqrt{B} (TT $t c \mu \tau$)	0.006	0.019	0.022	0.060	0.066	0.076
S/\sqrt{B} (TT $t \bar{t} \mu \tau$)	0.006	0.019	0.022	0.061	0.073	0.084
Acceptance (ST $t c \mu \tau$)	0.632	0.264	0.010	0.003	0.002	0.001
Acceptance (ST $t \bar{t} \mu \tau$)	0.617	0.261	0.005	0.001	0.001	0.000
Acceptance (TT $t c \mu \tau$)	0.463	0.059	0.056	0.026	0.016	0.012
Acceptance (TT $t \bar{t} \mu \tau$)	0.465	0.060	0.057	0.026	0.018	0.014

Table 11: Cutflow Table for Run2 data and MC samples in the category 2.

6 Top Mass Reconstruction

After the final event selection, the top quark mass is reconstructed using the final state particles with the minimum χ^2 method. The method is to minimize the χ^2 equation (Eq. 3 and 4), with the combination of jets. The events after the final selection step 5 (6) for the category 1 (category 2) contain exactly one muon, one tau, and one b-tagged jet. For the category 1, χ^2 equation (Eq. 3) includes SM top quark and W boson mass terms. While for the category 2, χ^2 equation (Eq. 4) involves the additional LFV top mass reconstruction term.

The two equations can be read as follows:

$$\chi_{cat1}^2 = \left(\frac{m_{t,sm} - m_{bjj}}{\sigma_{t,sm}} \right)_{SM_t}^2 + \left(\frac{m_{w,sm} - m_{jj}}{\sigma_{w,sm}} \right)_{SM_W}^2 \quad (3)$$

$$\chi_{cat2}^2 = \left(\frac{m_{t,lfv} - m_{j\mu\tau}}{\sigma_{t,lfv}} \right)_{LFV_t}^2 + \left(\frac{m_{t,sm} - m_{bjj}}{\sigma_{t,sm}} \right)_{SM_t}^2 + \left(\frac{m_{w,sm} - m_{jj}}{\sigma_{w,sm}} \right)_{SM_W}^2 \quad (4)$$

where $m_{t,lfv}$, $m_{t,sm}$ and $m_{w,sm}$ are LFV top mass, SM top mass and W boson mass, respectively, and $\sigma_{t,lfv}$, $\sigma_{t,sm}$ and $\sigma_{w,sm}$ are resolutions of LFV top quark, SM top quark and W boson.

Detector resolution is considered for the values of mass and resolutions for top quark and W boson. First, the origin of decay objects from the LFV top, SM top quark, or W boson are studied at the generator level, and they are matched with reconstructed objects. Second, masses are reconstructed with the reconstruction level objects matched with the generator-level objects, and we perform Voigt fitting on the mass distributions in Fig. 30. The fitting results of masses and resolutions are used instead of the theoretical values for the top quark mass reconstruction.

- Mass : $m_{t,lfv} = 150.5 \text{ GeV}$, $m_{t,sm} = 165.2 \text{ GeV}$, $m_{w,sm} = 80.8 \text{ GeV}$
- Resolution : $\sigma_{t,lfv} = 17.8 \text{ GeV}$, $\sigma_{t,sm} = 21.3 \text{ GeV}$, $\sigma_{w,sm} = 11.7 \text{ GeV}$

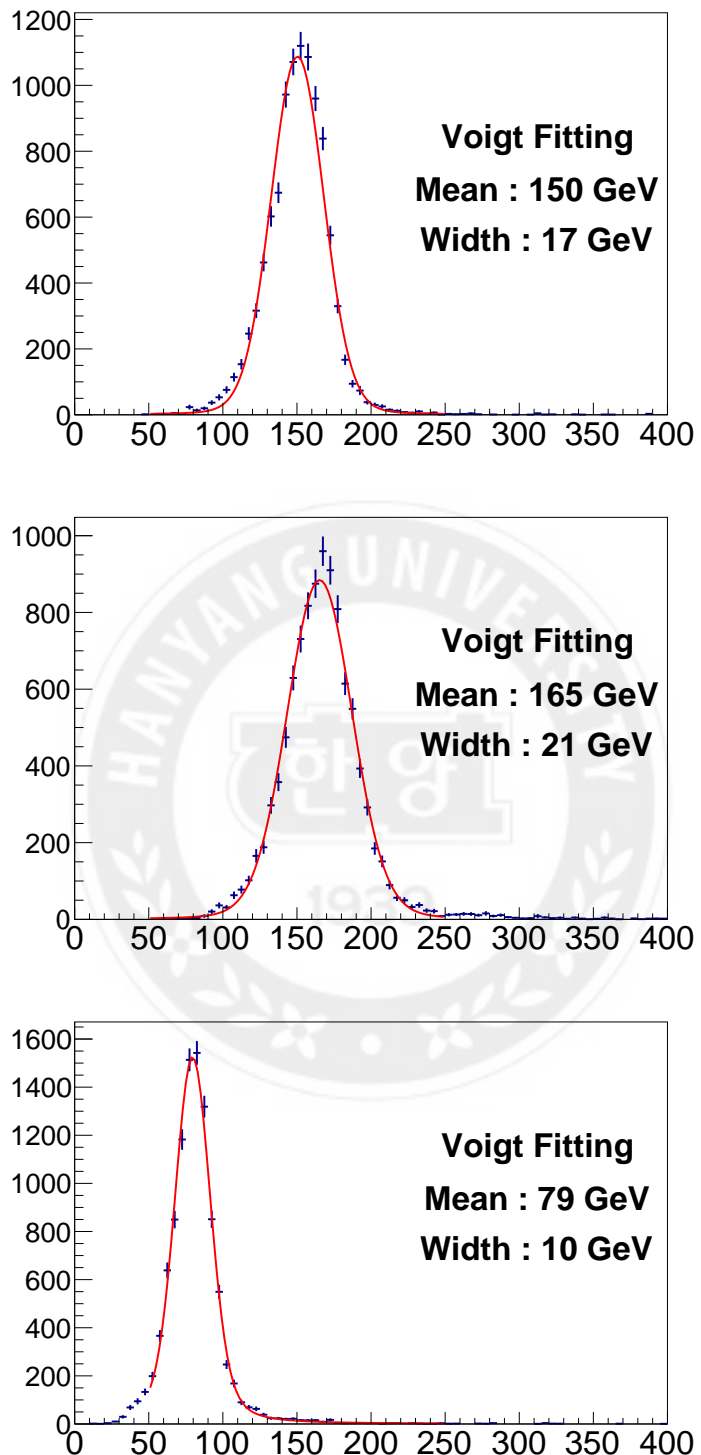


Figure 30: Voigt fitting results for mass of LFV top quark (top), SM top quark (middle), and W boson (bottom) from the left.

For the χ^2 method, the non b-tagged jets are looped over for matching jets from the SM decaying W boson and up-type jet from $t\bar{t}$ LFV process (category 2). In the Eq. 4, the first term is χ^2 of LFV top where one jet is assigned. And other two jets are assigned to "jj" in the second and third term that jets from hadronically decaying W boson. Therefore, we assign total 2 (3) jets for the category 1 (category 2) among the selected jets. For example, in the category 2, we require at least 3 jets excluding a b-tagged jet, and if there are 6 jets (contains a b-tagged jet) in an event, the number of non b-tagged jet combinations is ${}_5P_1 \times {}_4C_2 = 30$. The jets in the jet combination that provides the minimum χ^2 value are assigned to their associated parent particle such as LFV top, SM top or W boson. In Fig. 31, the χ^2 score distributions are in log-Y scaled, and the plots show no big difference in the signal and backgrounds.

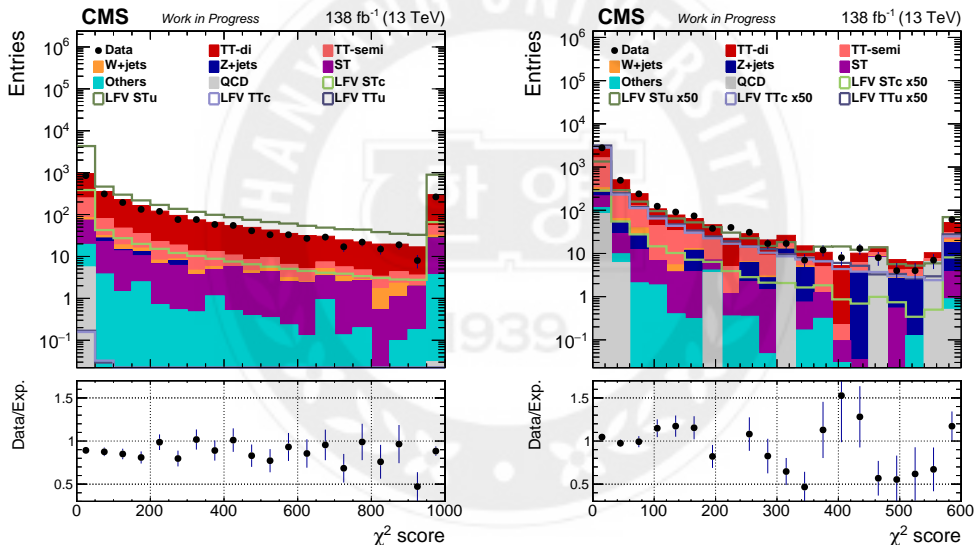


Figure 31: Distributions of χ^2 score from top reconstruction in the category 1 (left) and 2 (right).

The reconstructed SM top and SM W boson distributions are in Fig. 32 and 33 for both categories. The distributions of reconstructed mass of LFV top is in Fig. 34 for the category 2. The data points are blinded for the mass resonance region where the signal exceeds the SM backgrounds. In Fig. 32 and 33, the distributions in the category 1 have more significant signal shapes compared to the backgrounds. However, in the category 2, the signal and background shapes are similar each other and it is more challenging to identify the signal from the background than the category 1.

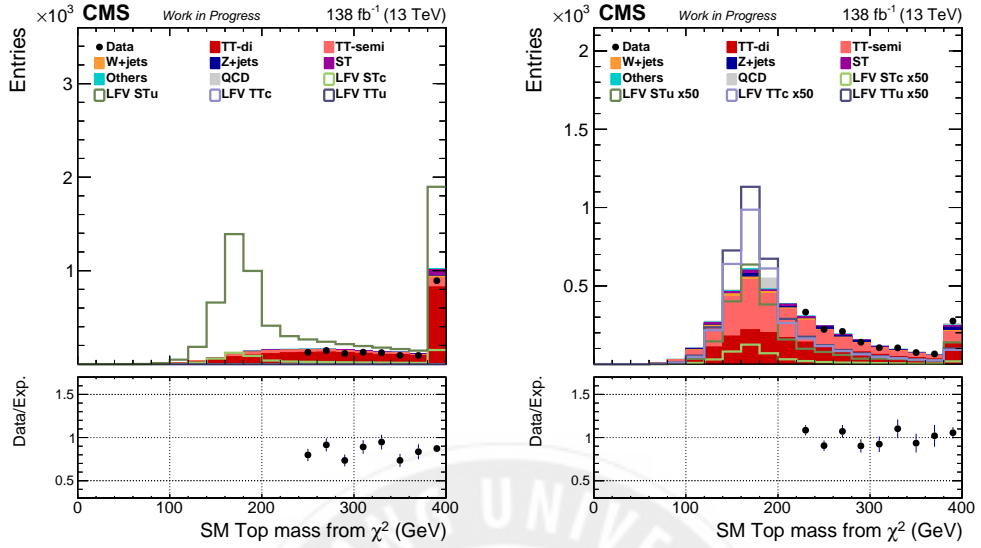


Figure 32: Distributions of SM top mass from top reconstruction in the category 1 (left) and 2 (right).

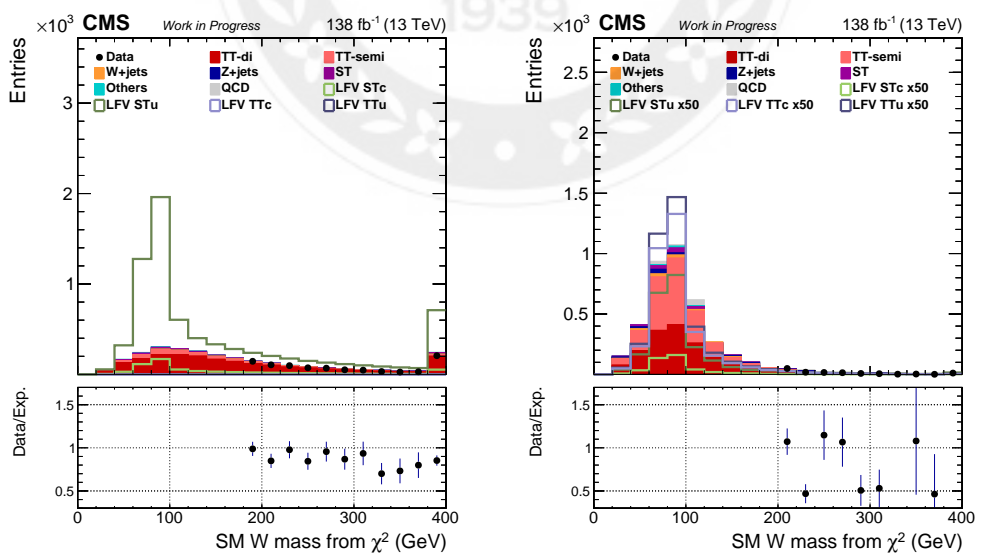


Figure 33: Distributions of W boson mass from top reconstruction in the category 1 (left) and 2 (right).

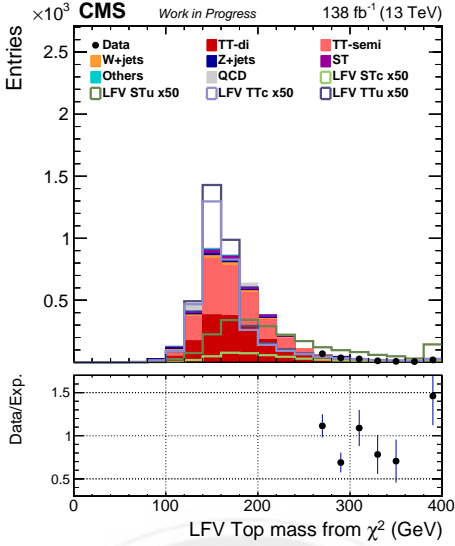


Figure 34: Distribution of LFV top mass from top reconstruction in the category 2.

7 Signal Extraction

Signal extraction for LFV signal is performed with a deep neural network (DNN) algorithm, which is a machine learning technique to perform multivariate analysis. By using the DNN algorithm, the signal processes are expected to be well distinguished from the background processes. The SM $t\bar{t}$ events are used as the background component as it is 90% of all the background. We separately extract the signal processes from the category 1 and 2. ST LFV events are used as input signal events for the category 1 and $t\bar{t}$ LFV events as signal inputs for the category 2. The training and evaluation of the two categories are performed separately, and details are explained in the following sections. Through the signal extraction, the DNN output distribution is obtained as a probability distribution of the signal.

7.1 Model Training

The events are divided into two categories, and input samples and hyperparameters for DNN training are separated for each category. To increase the statistics for the DNN training, full run 2 signal and background events are included for training the model. Training is performed using Keras backend [53] of Tensorflow [54], and the input data structure is flattened for the training. In this section, input variables (features) for the categories are

introduced, and hyperparameters are optimized in terms of the accuracy of the trained model.

Input Samples and Variables

LFV signal events are used as input signal samples for DNN training. Different signal (ST or $t\bar{t}$) LFV events are used for the category 1 and 2. Scalar, vector, and tensor-like LFV events are all included for training. The SM $t\bar{t}$ semi-leptonic and di-leptonic events are used as input background samples for DNN training. All events in the input samples are randomized to remove any bias from the order of the input samples. We balance the number of events for signal and background events so that statistical bias is suppressed for the dominant class. Total $159,334 = 79,667$ signal+ $79,667$ background events are used for training in the category 1, and $202,124 = 101,062$ signal+ $101,062$ background events in the category 2. We use 70% of total events for training and the remainder (30%) events for validation of training.

Input variables are collected with the kinematic variables from final selection and the top reconstruction. In Table. 12, the input variable are summarized with the descriptions. **29 variables** are used for training in the category 1 and **46 variables** are used in the category 2. The correlation of input features for signal and background events in the category 1 and 2 are shown in Fig. 35 and 36. The whiter indication in the correlation matrix, the less the correlation between two variables.

Group	Category 1	Category 2	Description
Muon (μ)	$p_{T\mu}, \eta_\mu$		p_T and η of selected muon.
Tau (τ_h)	$p_{T\tau_h}, \eta_{\tau_h}, m_{\tau_h}$		p_T and η of selected τ_h .
MuTau ($\mu\tau_h$)	$m_{\mu\tau_h}, \Delta\eta_{\mu\tau_h}, \Delta\phi_{\mu\tau_h}, \Delta R_{\mu\tau_h}$		Reconstructed with selected μ and τ_h .
Jet (j)	$p_{Tj1}, p_{Tj2}, p_{Tj3}, p_{Tj4}$ $\eta_{j1}, \eta_{j2}, \eta_{j3}$ m_{j1}, m_{j2}, m_{j3} $btag_{j1}, btag_{j2}, btag_{j3}$	$\eta_{j1}, \eta_{j2}, \eta_{j3}, \eta_{j4}$ $m_{j1}, m_{j2}, m_{j3}, m_{j4}$ $btag_{j1}, btag_{j2}, btag_{j3}, btag_{j4}$	p_T of jets in higher p_T order. Mass of jets in higher p_T order. b-tag discriminant of jets in higher p_T order.
MET (E_T^{miss})	$E_T^{miss}, \phi_{E_T^{miss}}$		E_T^{miss} and ϕ of E_T^{miss}
Top Reco.	$\chi^2, m_{tSM}, m_{W_{SM}}$ $\Delta\eta_{Wjj}, \Delta\Phi_{Wjj}, \Delta R_{Wjj}$	$\chi^2, m_{t_{LFV}}, m_{W_{SM}}, m_{t_{LFV}}$ $\Delta\eta_{Wjj}, \Delta\Phi_{Wjj}, \Delta R_{Wjj}$ $\Delta\eta_{j\mu}, \Delta\Phi_{j\mu}, \Delta R_{j\mu}, m_{j\mu}$ $\Delta\eta_{j\tau_h}, \Delta\Phi_{j\tau_h}, \Delta R_{j\tau_h}, m_{j\tau_h}$ $\Delta\eta_{j\mu\tau_h}, \Delta\Phi_{j\mu\tau_h}, \Delta R_{j\mu\tau_h}, m_{j\mu\tau_h}$	χ^2 score and reconstructed masses. Variables related to W boson reco. Reconstructed with LFV jet and μ Reconstructed with LFV jet and τ_h Reconstructed with LFV jet and $\mu\tau_h$

Table 12: Input variables for DNN training in the category 1 and 2.

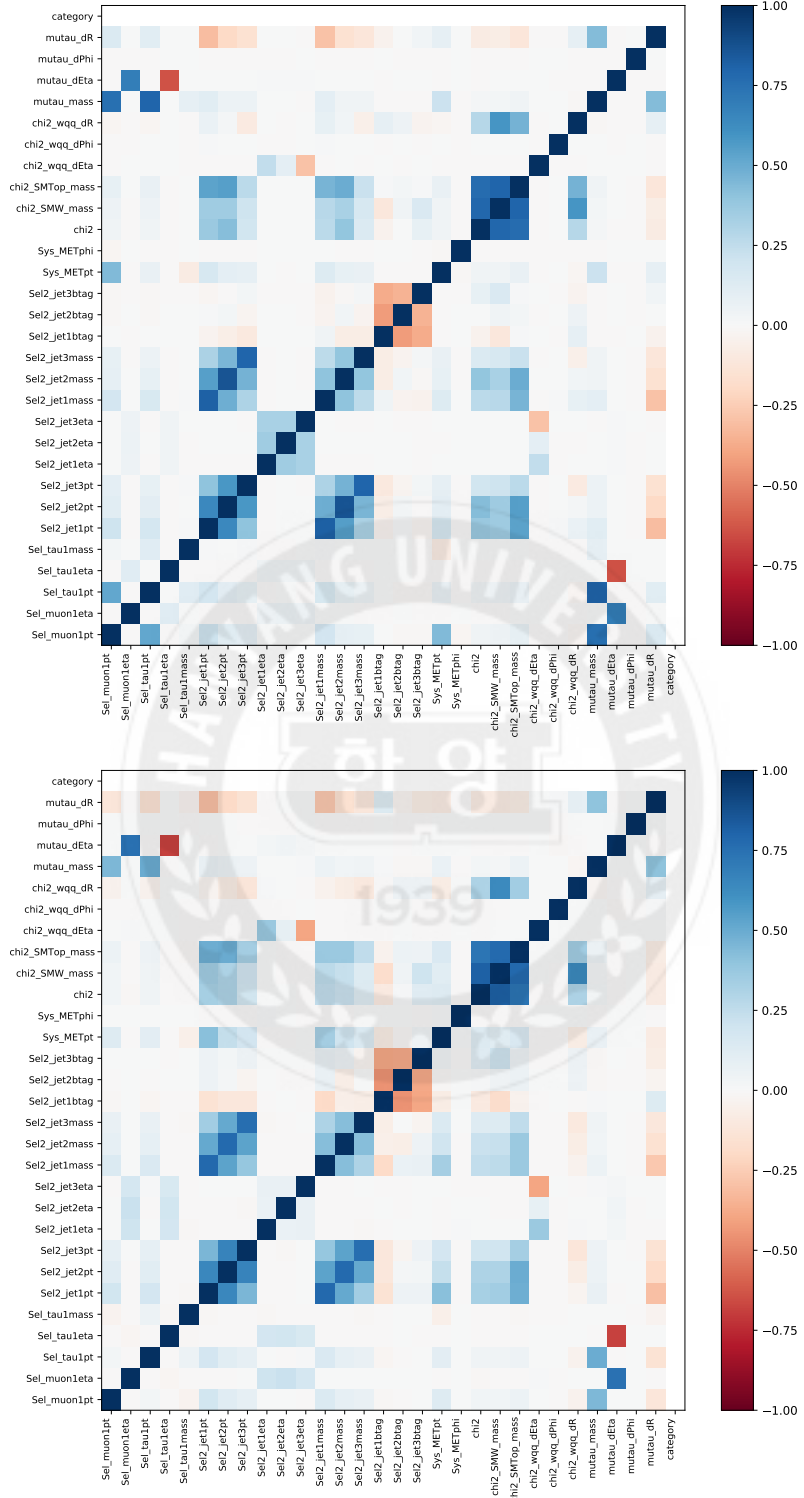


Figure 35: Correlation matrix for signal (upper) and background (lower) input variables in the category 1.

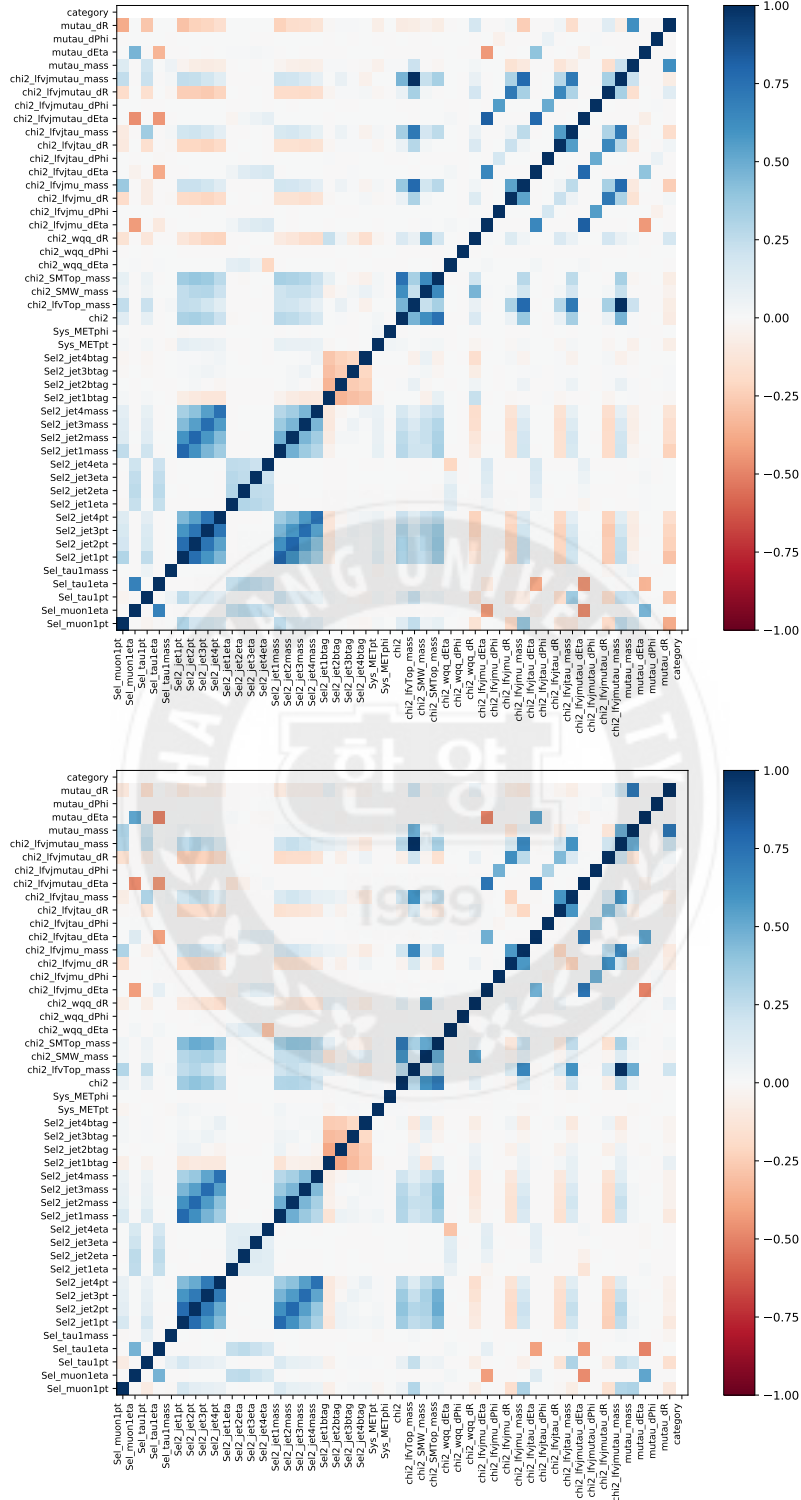


Figure 36: Correlation matrix for signal (upper) and background (lower) input variables in the category 2.

Hyperparameters for Training

Most of the hyperparameters are set the same in the category 1 and 2, except the number of epochs which is automatically determined with the early stopping option. The early stopping option is set with the minimum validation loss, and the training stops after the patience of 30 epochs. Hyperparameters such as the number of hidden layers, the number of nodes per layer, activation function, weight initializer, and optimizer are optimized in terms of the accuracy of the trained model.

Hyperparameter Optimization

- Keras backend Tensorflow is used.
- Batch normalization and L2 Regularization for all hidden layers.
- 2 Hidden Layers, 50 Nodes per Hidden Layers, 1024 Batch size.
- ReLu Activation Function, Adam Optimizer, Random Normal Weight Initializer
- Sparse Categorical Cross Entropy for Loss Function.

Train Results

After the training for the DNN model with the optimized hyperparameters, the signal events are distinguished with the highest accuracy from background $t\bar{t}$ events using the DNN model. In Fig. 37, the accuracy of the DNN model is 93.88% for the category 1 and 77.47% for the category 2, with the diagonalized probability of true positive and true negative. The result from the category 2 shows lower accuracy than category 1 since the top decaying in the SM contributes to both the $t\bar{t}$ LFV signal and the SM $t\bar{t}$ background events. Also, the off-diagonal part of the confusion matrix (false positive or false negative) has a higher probability in the category 2 than in the category 1, which can lead to irreducible backgrounds. In Fig. 38, DNN output distributions for train and test agree with each other in both categories where there is no overtraining for the trained model. The distributions of loss and accuracy per epoch in Appendix II show higher accuracy and lower loss for train than for test, and this is the usual case of DNN. DNN training is stopped before the differences between train and test cases get larger to prevent overtraining and this can be checked through the distributions per epochs.

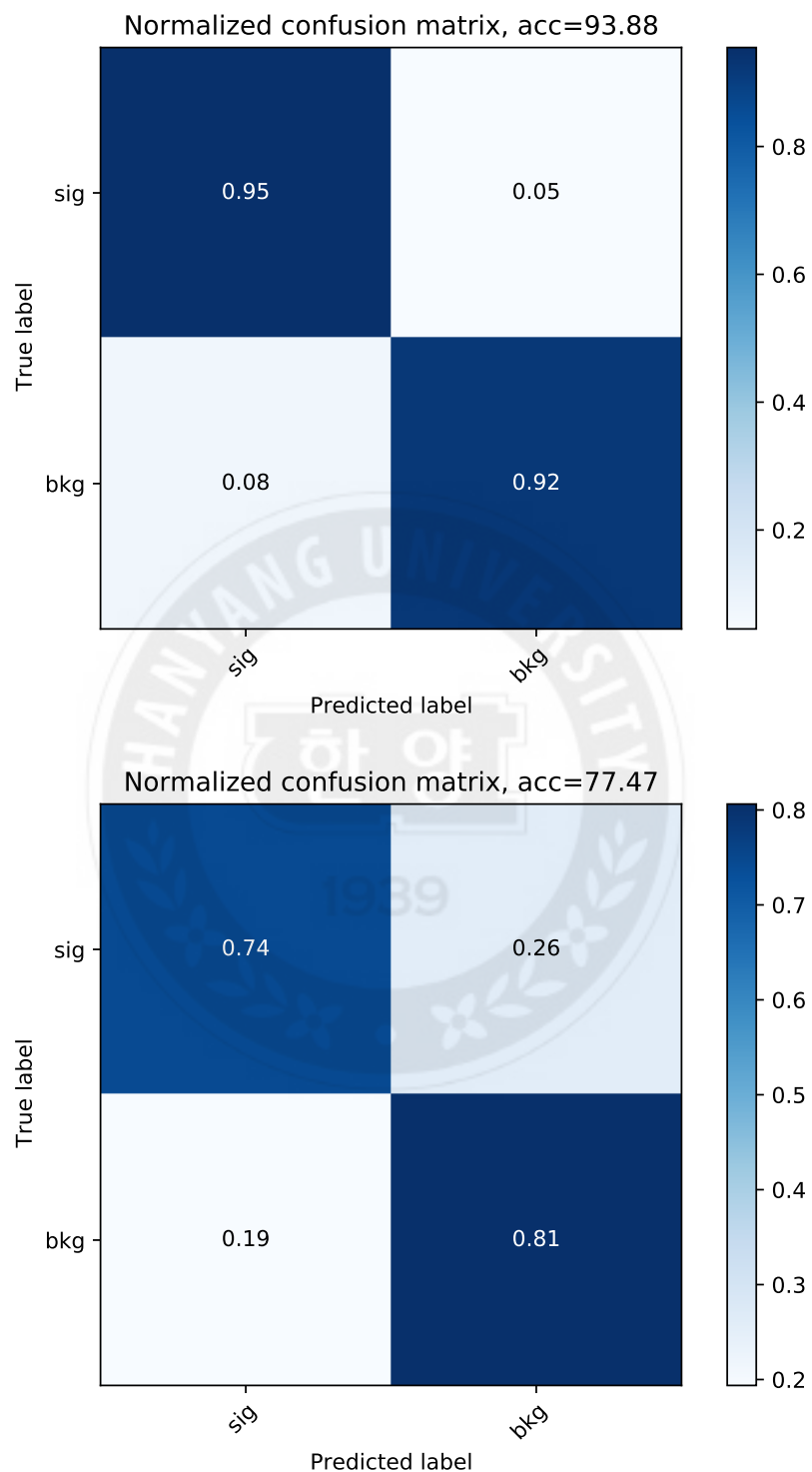


Figure 37: Normalized confusion matrix for training models in the category 1 (upper) and 2 (lower).

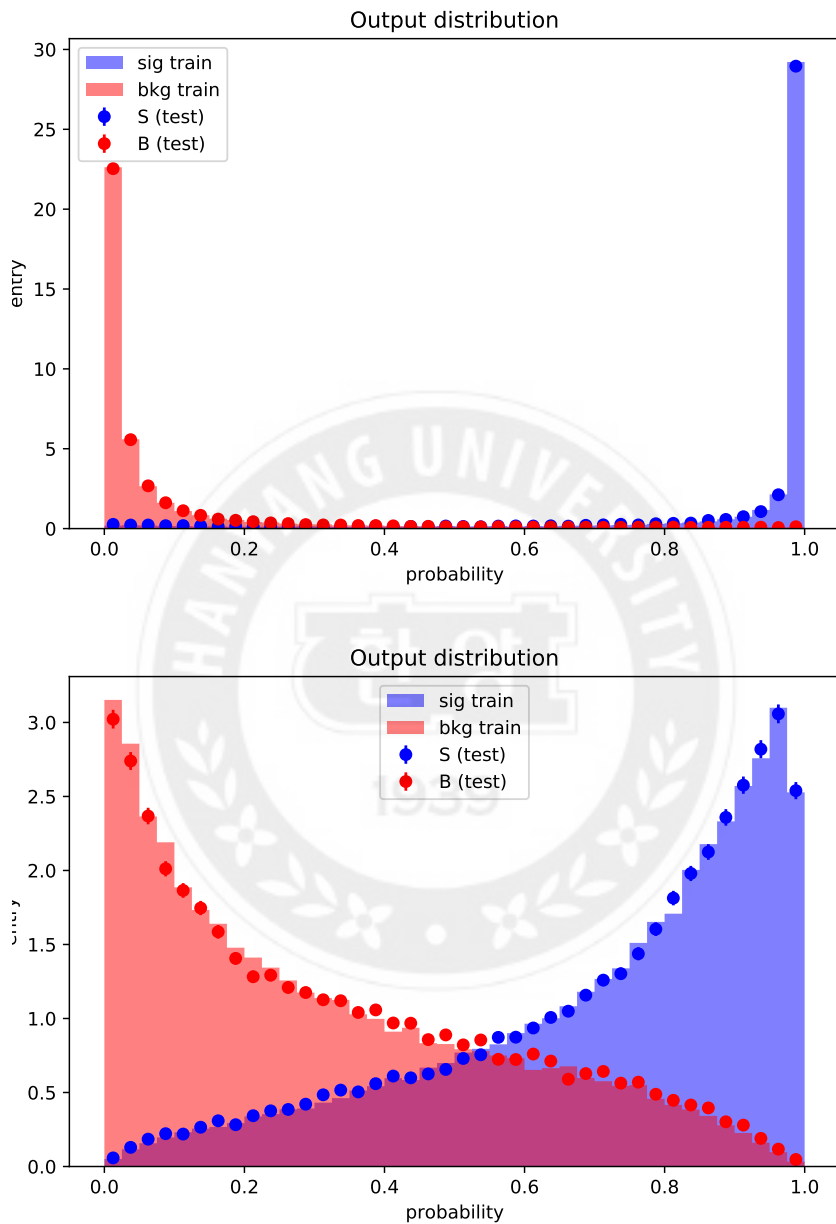


Figure 38: DNN output distributions of signals and backgrounds showing agreements in train and test for the category 1 (upper) and 2 (lower). X-axis: Probability, Y-axis: Arbitrary Unit

7.2 Evaluation

The evaluation process is performed with all MC samples and the training models from the previous step of the signal extraction. Since the separation of the categories does not imply that, for example, the ST LFV events do not exist in the category 2, both the ST and $t\bar{t}$ LFV events are evaluated by the DNN models in both categories. The output distribution for run 2 is shown in Fig. 39, and signal histograms are drawn only with vector-like LFV samples. The signal output distribution in the category 1 has more significance compared to background events than in the category 2. The distributions are used to set the limits of Wilson coefficients in Section 9.

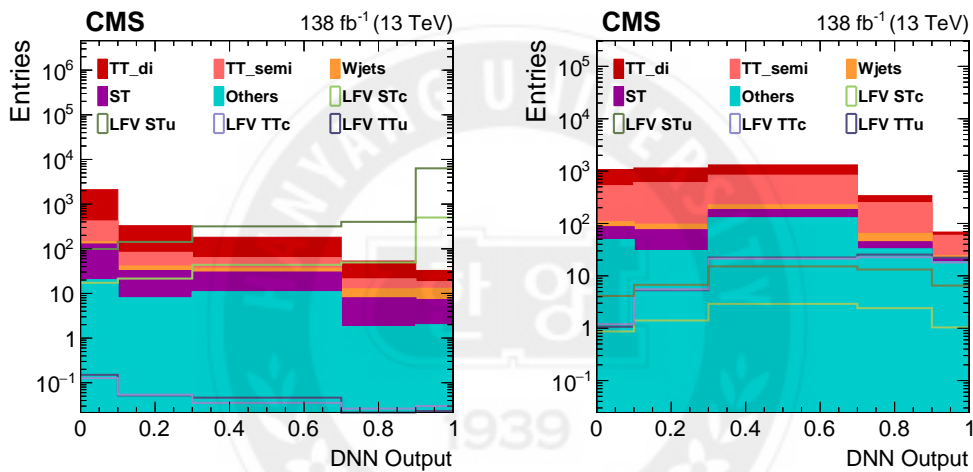


Figure 39: DNN output distribution for run 2 evaluation in the category 1 (left) and 2 (right)

8 Systematic Uncertainties

8.1 Systematic Sources

Luminosity Luminosity POG in CMS collaboration provides uncertainties of integrated luminosity for entire run 2 data. Recommended uncertainties for luminosity in each year are 1.2%, 2.3%, and 2.5% for 2016, 2017, and 2018 integrated luminosity. Correlated and uncorrelated uncertainties of luminosity for each year are considered.

Pileup Pileup systematic uncertainties are studied with systematic variations of data pileup profiles as introduced in Section 3.3. The difference between data and MC profiles is corrected as pileup re-weighting, and this is done for systematic variations to get pileup shape uncertainties.

Jet Energy Scale (JES) We apply jet energy correction (JEC) for JES with scaling the p_T of jets, E_T^{miss} , and ϕ of E_T^{miss} . In Fig. 40, up and down systematic variations for MC events are shown for leading jet's p_T , E_T^{miss} , and ϕ of E_T^{miss} .

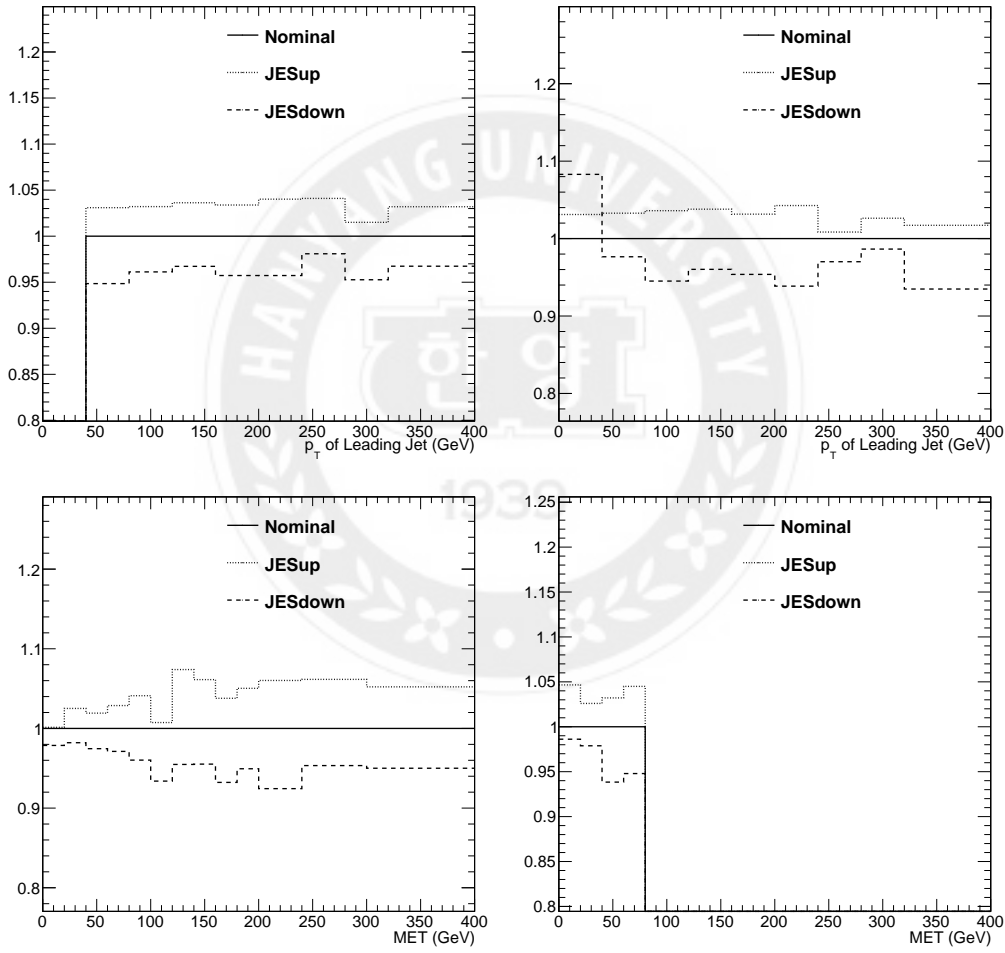


Figure 40: JES systematic variation distributions for p_T of the leading jet (upper row) and E_T^{miss} (lower row) in the category 1 (left column) and 2 (right column).

B-tagging Scale Factor BTV POG in CMS collaboration provides the b-tagging scale factors, and this analysis re-calibrates the shape of b-tagging discriminators with iterative fit

mode. The POG recommends applying b-tagging SF uncertainty for jes, hf, and lf sources, and all sources are applied in this analysis.

8.2 Systematic Variations on DNN Output Distribution

We have obtained the DNN output distributions from the previous Section 7. The variations by systematic uncertainties are studied with the DNN output distributions to understand the variation by systematic sources. The shapes with the systematic uncertainties are used to apply systematic uncertainties to setting upper limits of the Wilson coefficient of the LFV signal operator. Shapes of jet energy scale, pile-up, and b-tagging SF systematic sources are studied in Fig. 41.

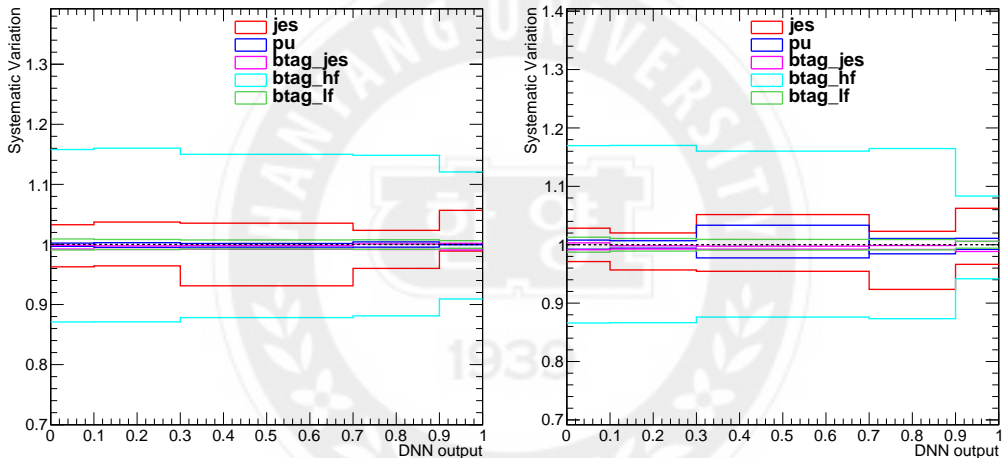


Figure 41: Systematic variations for Run II on DNN output distribution in the category 1 (left) and 2 (right).

9 Results

LFV signal strength is determined by the Wilson coefficients for each LFV interaction operator. The event reconstruction and selection are made to improve the significance of both ST and $t\bar{t}$ LFV processes in separate categories. Upper limits of signal strength are calculated with the Combine Tool [55]. In different event categories and runs, the upper limits are set for each category, and the limits are combined from two categories (e.g., 16APV cat 1 and cat 2 are combined). Combining for Run II limits is done by combining the combined

limits for each year (e.g., the combined run 16APV, 16, 17, and 18 are further combined as run2). Limits are calculated with the shape method, and, as an input shape, the DNN output distribution is used. Shapes of LFV signals and backgrounds ($t\bar{t}$ di-leptonic, $t\bar{t}$ semi-leptonic, single top, W+Jets, and others) and systematic uncertainties are included as input shapes of the combine tool.

The results are expressed as limits of signal strength (r), and when r is 1.0, the Wilson coefficient is 1.0 as initially assumed. Limits of the cross-section for the LFV signal are calculated by multiplying the signal strength limit on the sum of ST and $t\bar{t}$ LFV sample cross sections. Limits of the Wilson coefficient are calculated as the square root of the signal strength (\sqrt{r}) since interaction strength is the square of the Wilson coefficient. Limits of the branching fractions of LFV top decay are calculated with the limits of the Wilson coefficient using the Eq. 2. In Table 13, the limits of cross section, Wilson coefficient, and branching ratio for each interaction and type are listed for run 2 combined results with the $\pm 1\sigma$ deviations. When setting the limits, the impacts of the systematic sources are calculated in Fig. 42–44. The btag_jes and jes systematic sources strongly impact most of the interaction types. Since the systematic variations of two sources are relatively large compared to other sources, the uncertainties from two sources are constrained.

Category	Interaction	Type	σ [fb]	$C_{tq\mu\tau}/\Lambda^2$ [TeV^{-2}]	$Br(t \rightarrow q\mu\tau) \times 10^{-6}$
Combined	$t\mu\tau$	Scalar	2.01 [1.402, 2.908]	0.4463 [0.3727, 0.5368]	0.3194 [0.2227, 0.4621]
		Vector	2.705 [1.901, 3.935]	0.2154 [0.1806, 0.2598]	0.1488 [0.1045, 0.2165]
		Tensor	3.443 [2.336, 4.888]	0.1058 [0.08718, 0.1261]	0.8621 [0.585, 1.224]
	$t\mu\tau$	Scalar	1.349 [0.9168, 1.998]	0.1249 [0.103, 0.152]	0.02501 [0.017, 0.03704]
		Vector	1.409 [1.036, 2.321]	0.05831 [0.05, 0.07483]	0.0109 [0.008018, 0.01796]
		Tensor	2.888 [1.155, 3.465]	0.03873 [0.02449, 0.04243]	0.1155 [0.04618, 0.1385]

Table 13: Table for run2 combined upper limits of LFV cross section (σ), Wilson Coefficient ($C_{tq\mu\tau}$), and branching fraction for different types of interactions. $\pm 1\sigma$ values are in brackets.

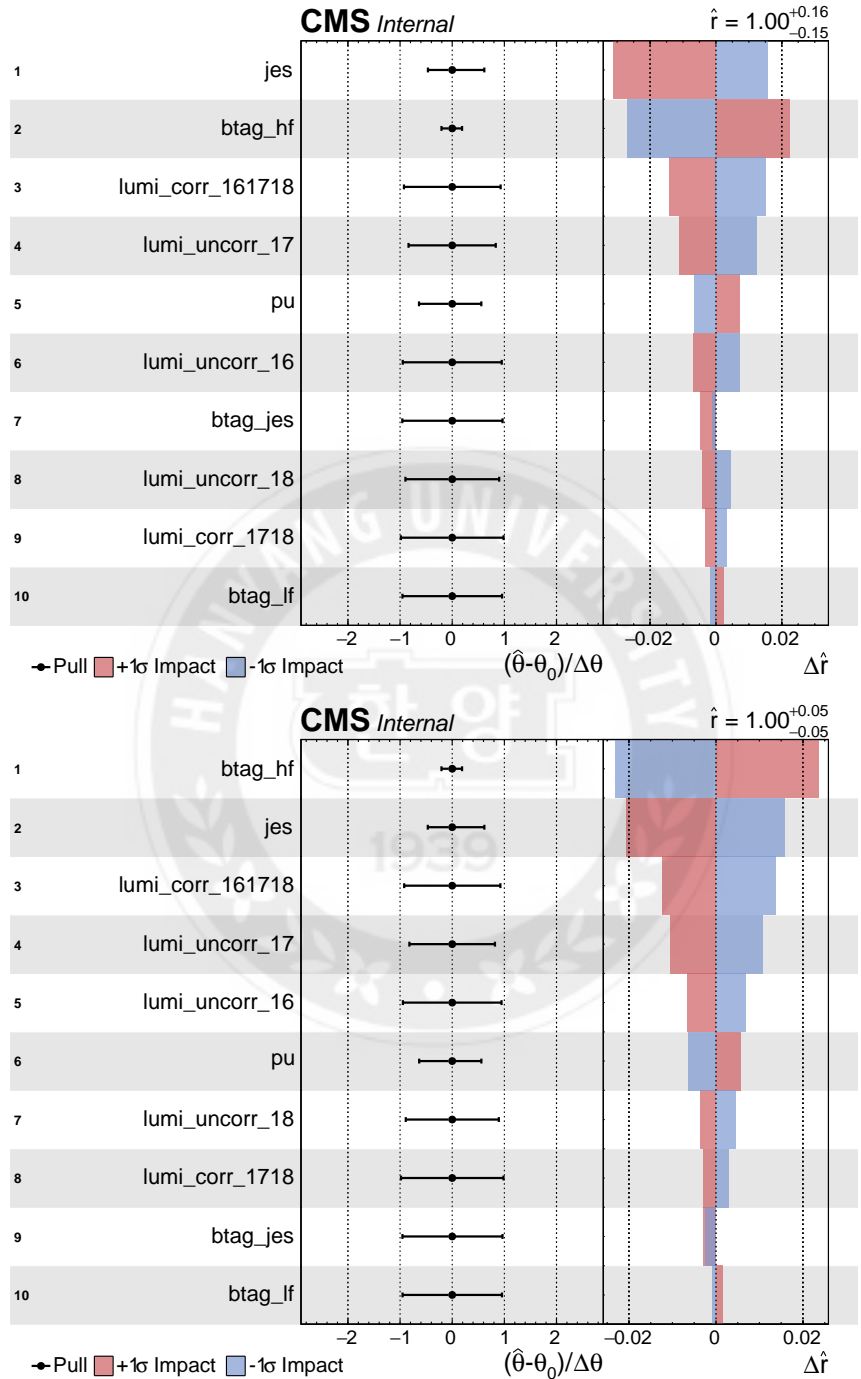


Figure 42: Combined run 2 impact of systematic sources when setting limits for scalar-like operators in $tc\mu\tau$ (upper) and $tu\mu\tau$ (lower) interaction.

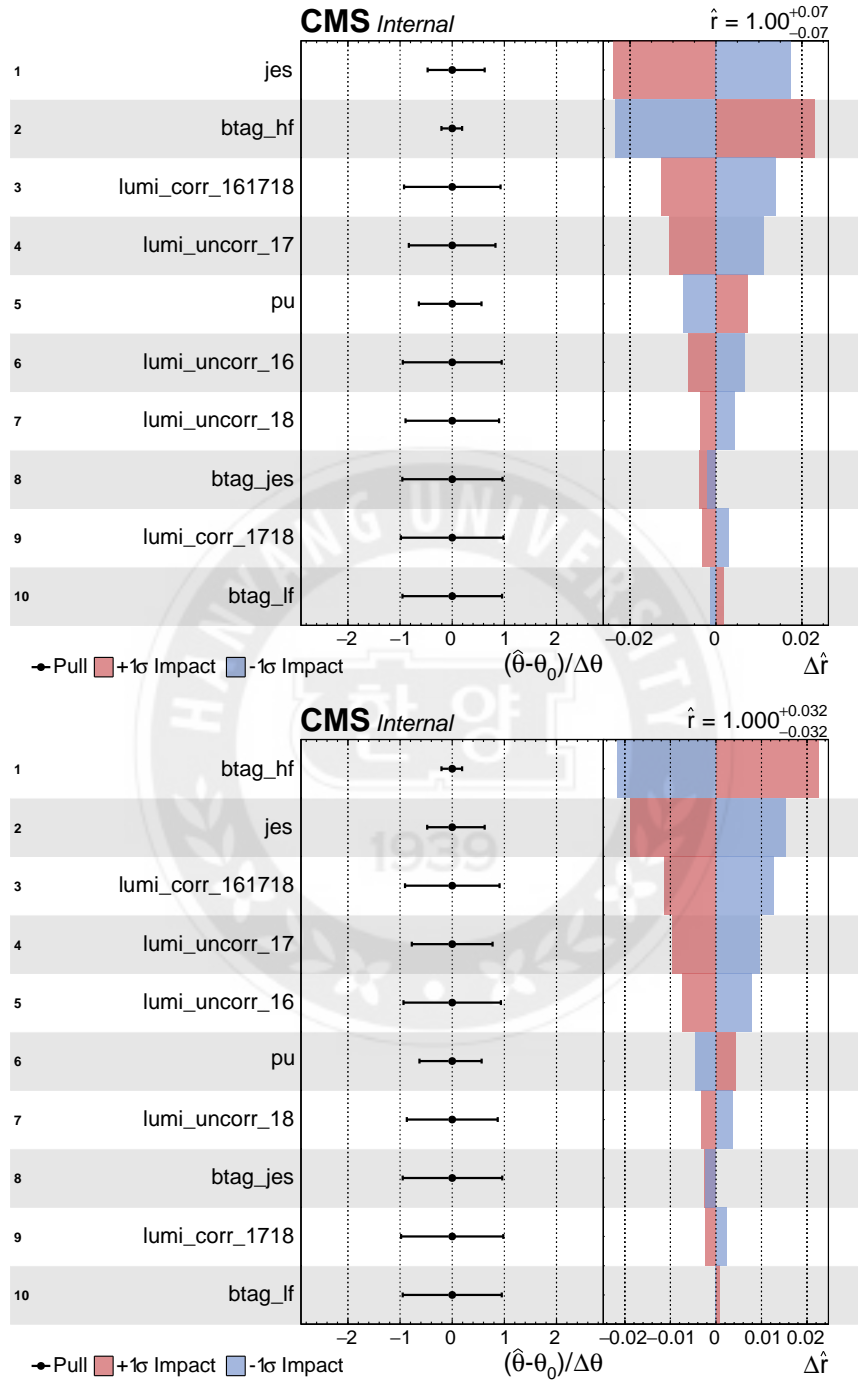


Figure 43: Combined run 2 impact of systematic sources when setting limits for vector-like operators in $tc\mu\tau$ (upper) and $tu\mu\tau$ (lower) interaction.

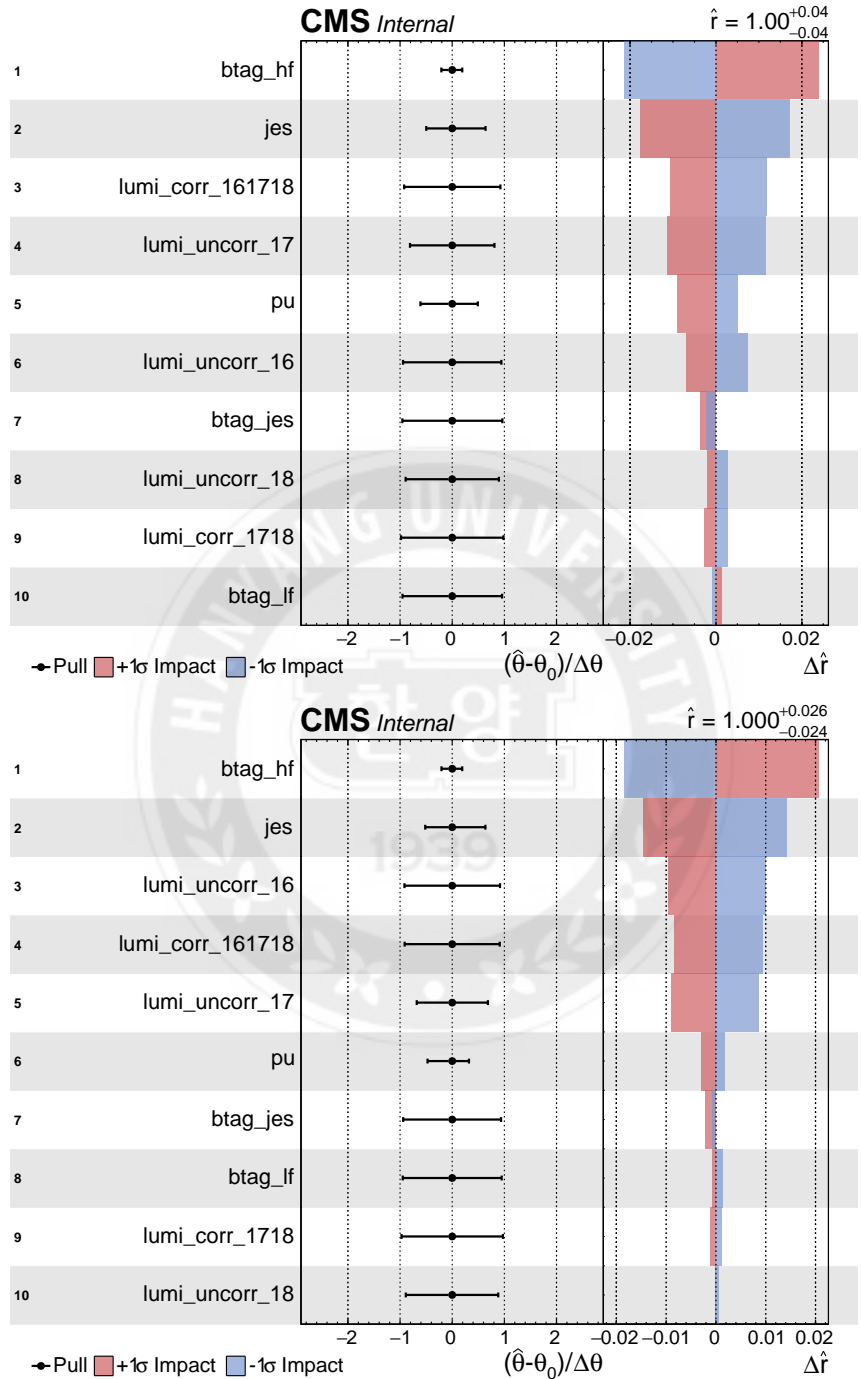


Figure 44: Combined run 2 impact of systematic sources when setting limits for tensor-like operators in $tc\mu\tau$ (upper) and $tu\mu\tau$ (lower) interaction.

10 Conclusion

This analysis searches CLFV signals using Run 2 data using several steps of event selections and machine learning techniques with DNN. We use advanced tools such as DNN, b-tagging algorithm, or tau identification algorithm for the analysis to improve the performance. The expected upper limits are calculated by combining the entire run 2 MC events with blinding the data. The expected limits of branching fraction in the CLFV top decay processes are set $Br(t \rightarrow c\mu\tau) < 3.194 \times 10^{-5}$, 1.488×10^{-5} , 8.621×10^{-5} and $Br(t \rightarrow u\mu\tau) < 0.2501 \times 10^{-5}$, 0.109×10^{-5} , 1.155×10^{-5} for scalar, vector, and tensor-like operators, respectively. The results using data will be published after the approval from the CMS collaboration.



References

- [1] Peter W. Higgs. “Broken symmetries, massless particles and gauge fields”. In: Phys. Lett. 12 (1964), pp. 132 – 133. DOI: 10.1016/0031-9163(64)91136-9.
- [2] Philip W. Anderson. “Plasmons, Gauge Invariance, and Mass”. In: Phys. Rev. 130 (1963). Ed. by J. C. Taylor, pp. 439 – 442. DOI: 10.1103/PhysRev.130.439.
- [3] Serguei Chatrchyan et al. “Observation of a New Boson at a Mass of 125 GeV with the CMS Experiment at the LHC”. In: Phys. Lett. B 716 (2012), pp. 30 – 61. DOI: 10.1016/j.physletb.2012.08.021. arXiv: 1207.7235 [hep-ex].
- [4] Georges Aad et al. “Observation of a new particle in the search for the Standard Model Higgs boson with the ATLAS detector at the LHC”. In: Phys. Lett. B 716 (2012), pp. 1 – 29. DOI: 10.1016/j.physletb.2012.08.020. arXiv: 1207.7214 [hep-ex].
- [5] S. Alekhin, A. Djouadi, and S. Moch. “The top quark and Higgs boson masses and the stability of the electroweak vacuum”. In: Phys. Lett. B 716 (2012), pp. 214 – 219. DOI: 10.1016/j.physletb.2012.08.024. arXiv: 1207.0980 [hep-ph].
- [6] Large Hadron Collider. URL: <https://home.cern/science/accelerators/large-hadron-collider>.
- [7] CERN accelerating science. URL: <https://cms.cern/detector>.
- [8] J. P. Lees et al. “Evidence for an excess of $\bar{B} \rightarrow D^{(*)}\tau^-\bar{\nu}_\tau$ decays”. In: Phys. Rev. Lett. 109 (2012), p. 101802. DOI: 10.1103/PhysRevLett.109.101802. arXiv: 1205.5442 [hep-ex].
- [9] M. Huschle et al. “Measurement of the branching ratio of $\bar{B} \rightarrow D^{(*)}\tau^-\bar{\nu}_\tau$ relative to $\bar{B} \rightarrow D^{(*)}\ell^-\bar{\nu}_\ell$ decays with hadronic tagging at Belle”. In: Phys. Rev. D 92.7 (2015), p. 072014. DOI: 10.1103/PhysRevD.92.072014. arXiv: 1507.03233 [hep-ex].
- [10] S. Hirose et al. “Measurement of the τ lepton polarization and $R(D^*)$ in the decay $\bar{B} \rightarrow D^*\tau^-\bar{\nu}_\tau$ ”. In: Phys. Rev. Lett. 118.21 (2017), p. 211801. DOI: 10.1103/PhysRevLett.118.211801. arXiv: 1612.00529 [hep-ex].
- [11] G. Caria et al. “Measurement of $\mathcal{R}(D)$ and $\mathcal{R}(D^*)$ with a semileptonic tagging method”. In: Phys. Rev. Lett. 124.16 (2020), p. 161803. DOI: 10.1103/PhysRevLett.124.161803. arXiv: 1910.05864 [hep-ex].

- [12] Roel Aaij et al. “Measurement of the ratio of branching fractions $\mathcal{B}(\bar{B}^0 \rightarrow D^{*+}\tau^-\bar{\nu}_\tau)/\mathcal{B}(\bar{B}^0 \rightarrow D^{*+}\mu^-\bar{\nu}_\mu)$ ”. In: Phys. Rev. Lett. 115.11 (2015). [Erratum: Phys. Rev. Lett. 115, 159901 (2015)], p. 111803. DOI: 10.1103/PhysRevLett.115.111803. arXiv: 1506.08614 [hep-ex].
- [13] R. Aaij et al. “Measurement of the ratio of the $B^0 \rightarrow D^{*-}\tau^+\nu_\tau$ and $B^0 \rightarrow D^{*-}\mu^+\nu_\mu$ branching fractions using three-prong τ -lepton decays”. In: Phys. Rev. Lett. 120.17 (2018), p. 171802. DOI: 10.1103/PhysRevLett.120.171802. arXiv: 1708.08856 [hep-ex].
- [14] Yasmine Sara Amhis et al. “Averages of b -hadron, c -hadron, and τ -lepton properties as of 2018”. In: Eur. Phys. J. C81 (2021). updated results and plots available at <https://hflav.web.cern.ch/>, p. 226. DOI: 10.1140/epjc/s10052-020-8156-7. arXiv: 1909.12524 [hep-ex].
- [15] Tae Jeong Kim et al. “Correlation between $R_{D^{(*)}}$ and top quark FCNC decays in leptoquark models”. In: JHEP 07 (2019), p. 025. DOI: 10.1007/JHEP07(2019)025. arXiv: 1812.08484 [hep-ph].
- [16] Albert M Sirunyan et al. “Search for singly and pair-produced leptoquarks coupling to third-generation fermions in proton–proton collisions at $s=13$ TeV”. In: Phys. Lett. B 819 (2021), p. 136446. DOI: 10.1016/j.physletb.2021.136446. arXiv: 2012.04178 [hep-ex].
- [17] Albert M Sirunyan et al. “Search for pair production of first-generation scalar leptoquarks at $\sqrt{s} = 13$ TeV”. In: Phys. Rev. D 99.5 (2019), p. 052002. DOI: 10.1103/PhysRevD.99.052002. arXiv: 1811.01197 [hep-ex].
- [18] Albert M Sirunyan et al. “Search for heavy neutrinos and third-generation leptoquarks in hadronic states of two τ leptons and two jets in proton–proton collisions at $\sqrt{s} = 13$ TeV”. In: JHEP 03 (2019), p. 170. DOI: 10.1007/JHEP03(2019)170. arXiv: 1811.00806 [hep-ex].
- [19] Albert M Sirunyan et al. “Search for leptoquarks coupled to third-generation quarks in proton–proton collisions at $\sqrt{s} = 13$ TeV”. In: Phys. Rev. Lett. 121.24 (2018), p. 241802. DOI: 10.1103/PhysRevLett.121.241802. arXiv: 1809.05558 [hep-ex].

- [20] Albert M Sirunyan et al. “Search for pair production of second-generation leptoquarks at $\sqrt{s} = 13$ TeV”. In: Phys. Rev. D 99.3 (2019), p. 032014. DOI: 10.1103/PhysRevD.99.032014. arXiv: 1808.05082 [hep-ex].
- [21] J. Adam et al. “New constraint on the existence of the $\mu^+ \rightarrow e^+\gamma$ decay”. In: Phys. Rev. Lett. 110 (2013), p. 201801. DOI: 10.1103/PhysRevLett.110.201801. arXiv: 1303.0754 [hep-ex].
- [22] S. Mihara et al. “Charged Lepton Flavor Violation Experiments”. In: Annual Review of Nuclear and Particle Science 63.1 (2013), pp. 531–552. DOI: 10.1146/annurev-nucl-102912-144530. eprint: <https://doi.org/10.1146/annurev-nucl-102912-144530>. URL: <https://doi.org/10.1146/annurev-nucl-102912-144530>.
- [23] Morad Aaboud et al. “A search for lepton-flavor-violating decays of the Z boson into a τ -lepton and a light lepton with the ATLAS detector”. In: Phys. Rev. D 98 (2018), p. 092010. DOI: 10.1103/PhysRevD.98.092010. arXiv: 1804.09568 [hep-ex].
- [24] Georges Aad et al. “Search for lepton-flavour-violating decays of the Higgs and Z bosons with the ATLAS detector”. In: Eur. Phys. J. C 77.2 (2017), p. 70. DOI: 10.1140/epjc/s10052-017-4624-0. arXiv: 1604.07730 [hep-ex].
- [25] Albert M Sirunyan et al. “Search for lepton flavour violating decays of the Higgs boson to $\mu\tau$ and $e\tau$ in proton-proton collisions at $\sqrt{s} = 13$ TeV”. In: JHEP 06 (2018), p. 001. DOI: 10.1007/JHEP06(2018)001. arXiv: 1712.07173 [hep-ex].
- [26] Georges Aad et al. “Search for the lepton flavor violating decay $Z \rightarrow e\mu$ in pp collisions at \sqrt{s} TeV with the ATLAS detector”. In: Phys. Rev. D 90.7 (2014), p. 072010. DOI: 10.1103/PhysRevD.90.072010. arXiv: 1408.5774 [hep-ex].
- [27] Vardan Khachatryan et al. “Search for lepton flavour violating decays of the Higgs boson to $e\tau$ and $e\mu$ in proton-proton collisions at $\sqrt{s} = 8$ TeV”. In: Phys. Lett. B 763 (2016), pp. 472–500. DOI: 10.1016/j.physletb.2016.09.062. arXiv: 1607.03561 [hep-ex].
- [28] P. Abreu et al. “Search for lepton flavor number violating Z0 decays”. In: Z. Phys. C 73 (1997), pp. 243–251. DOI: 10.1007/s002880050313.

- [29] Sacha Davidson et al. “Lepton Flavour Violating top decays at the LHC”. In: Eur. Phys. J. C 75.9 (2015), p. 450. DOI: 10.1140/epjc/s10052-015-3649-5. arXiv: 1507.07163 [hep-ph].
- [30] Armen Tumasyan et al. “Search for charged-lepton flavor violation in top quark production and decay in pp collisions at $\sqrt{s} = 13$ TeV”. In: (Jan. 2022). arXiv: 2201.07859 [hep-ex].
- [31] D. Barducci et al. “Interpreting top-quark LHC measurements in the standard-model effective field theory”. In: (Feb. 2018). Ed. by Juan Antonio Aguilar-Saavedra et al. arXiv: 1802.07237 [hep-ph].
- [32] B. Grzadkowski et al. “Dimension-Six Terms in the Standard Model Lagrangian”. In: JHEP 10 (2010), p. 085. DOI: 10.1007/JHEP10(2010)085. arXiv: 1008.4884 [hep-ph].
- [33] Matteo Cacciari et al. “Top-pair production at hadron colliders with next-to-next-to-leading logarithmic soft-gluon resummation”. In: Phys. Lett. B 710 (2012), pp. 612–622. DOI: 10.1016/j.physletb.2012.03.013. arXiv: 1111.5869 [hep-ph].
- [34] S. Dasu et al. “CMS. The TriDAS project. Technical design report, vol. 1: The trigger systems”. In: (Dec. 2000).
- [35] “CMS: The TriDAS project. Technical design report, Vol. 2: Data acquisition and high-level trigger”. In: (Dec. 2002). Ed. by P. Sphicas.
- [36] J. Alwall et al. “The automated computation of tree-level and next-to-leading order differential cross sections, and their matching to parton shower simulations”. In: JHEP 07 (2014), p. 079. DOI: 10.1007/JHEP07(2014)079. arXiv: 1405.0301 [hep-ph].
- [37] R. Frederix et al. “The automation of next-to-leading order electroweak calculations”. In: JHEP 07 (2018). [Erratum: JHEP 11, 085 (2021)], p. 185. DOI: 10.1007/JHEP11(2021)085. arXiv: 1804.10017 [hep-ph].
- [38] Paolo Nason. “A New method for combining NLO QCD with shower Monte Carlo algorithms”. In: JHEP 11 (2004), p. 040. DOI: 10.1088/1126-6708/2004/11/040. arXiv: hep-ph/0409146.

- [39] Stefano Frixione, Paolo Nason, and Carlo Oleari. “Matching NLO QCD computations with Parton Shower simulations: the POWHEG method”. In: JHEP 11 (2007), p. 070. DOI: 10.1088/1126-6708/2007/11/070. arXiv: 0709.2092 [hep-ph].
- [40] Simone Alioli et al. “A general framework for implementing NLO calculations in shower Monte Carlo programs: the POWHEG BOX”. In: JHEP 06 (2010), p. 043. DOI: 10.1007/JHEP06(2010)043. arXiv: 1002.2581 [hep-ph].
- [41] Christian Bierlich et al. “A comprehensive guide to the physics and usage of PYTHIA 8.3”. In: (Mar. 2022). arXiv: 2203.11601 [hep-ph].
- [42] S. Agostinelli et al. “GEANT4 – a simulation toolkit”. In: Nucl. Instrum. Meth. A 506 (2003), pp. 250 – 303. DOI: 10.1016/S0168-9002(03)01368-8.
- [43] John Allison et al. “Geant4 developments and applications”. In: IEEE Trans. Nucl. Sci. 53 (2006), p. 270. DOI: 10.1109/TNS.2006.869826.
- [44] J. Allison et al. “Recent developments in Geant4”. In: Nucl. Instrum. Meth. A 835 (2016), pp. 186 – 225. DOI: 10.1016/j.nima.2016.06.125.
- [45] URL: <https://twiki.cern.ch/twiki/bin/view/CMSPublic/SummaryResultsHIG>.
- [46] URL: https://twiki.cern.ch/twiki/bin/view/LHCPhysics/TtbarNNLO#Top_quark_pair_cross_sections_at.
- [47] A.M. Sirunyan et al. “Particle-flow reconstruction and global event description with the CMS detector”. In: JINST 12.10 (2017), P10003. DOI: 10.1088/1748-0221/12/10/P10003. arXiv: 1706.04965 [physics.ins-det].
- [48] A. M. Sirunyan et al. “Performance of the CMS muon detector and muon reconstruction with proton–proton collisions at $\sqrt{s} = 13$ TeV”. In: JINST 13.06 (2018), P06015. DOI: 10.1088/1748-0221/13/06/P06015. arXiv: 1804.04528 [physics.ins-det].
- [49] “Reconstruction and identification of τ lepton decays to hadrons and ν_τ at CMS”. In: JINST 11 (2016), P01019. ISSN: 0370-2693. DOI: 10.1088/1748-0221/11/01/P01019. URL: <http://iopscience.iop.org/1748-0221/11/01/P01019>.
- [50] A.M. Sirunyan et al. “Performance of reconstruction and identification of τ leptons decaying to hadrons and ν_τ in pp collisions at $\sqrt{s} = 13$ TeV”. In: JINST 13.10 (2018), P10005. DOI: 10.1088/1748-0221/13/10/P10005. arXiv: 1809.02816 [hep-ex].

- [51] Matteo Cacciari, Gavin P. Salam, and Gregory Soyez. “The anti- k_T jet clustering algorithm”. In: JHEP 04 (2008), p. 063. DOI: 10.1088/1126-6708/2008/04/063. arXiv: 0802.1189 [hep-ex].
- [52] “Performance of the DeepTau algorithm for the discrimination of taus against jets, electron, and muons”. In: (Oct. 2019). URL: <https://cds.cern.ch/record/2694158>.
- [53] Francois Chollet et al. Keras. 2015. URL: <https://github.com/fchollet/keras>.
- [54] Martin Abadi et al. TensorFlow: Large-Scale Machine Learning on Heterogeneous Systems. Software available from tensorflow.org. 2015. URL: <http://tensorflow.org/>.
- [55] Procedure for the LHC Higgs boson search combination in Summer 2011. Tech. rep. Geneva: CERN, Aug. 2011. URL: <https://cds.cern.ch/record/1379837>.



Appendix I. Control Plots for Run 2 data and MC

Category 1

Step 1

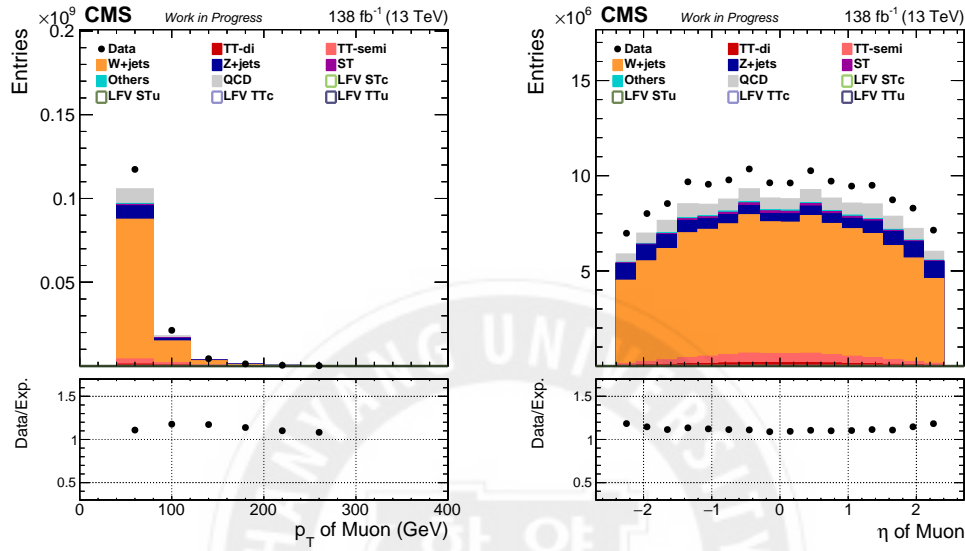


Figure 45: Control plots for p_T (left) and η (right) of selected muon (S1) in the category 1.

Step 2

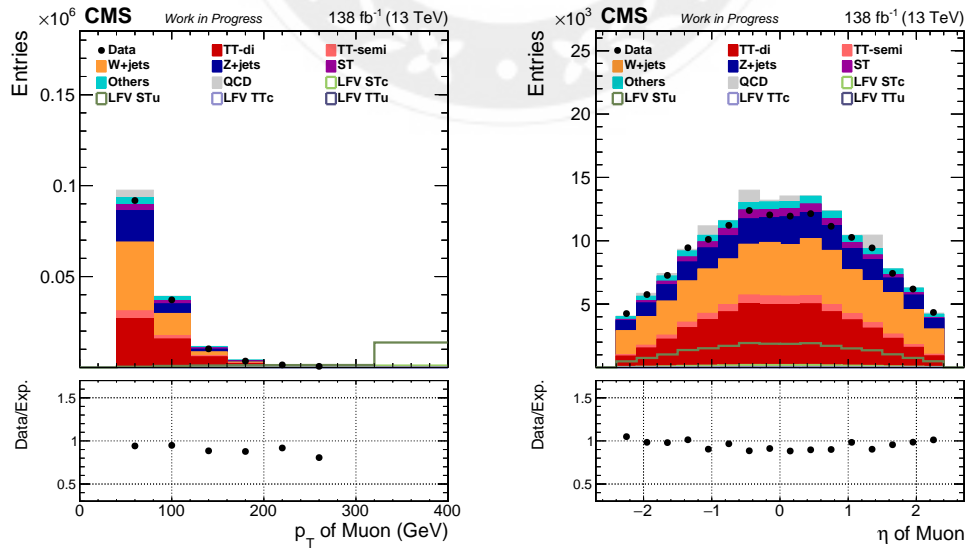


Figure 46: Control plots for p_T (left) and η (right) of selected muon (S2) in the category 1.

Step 2

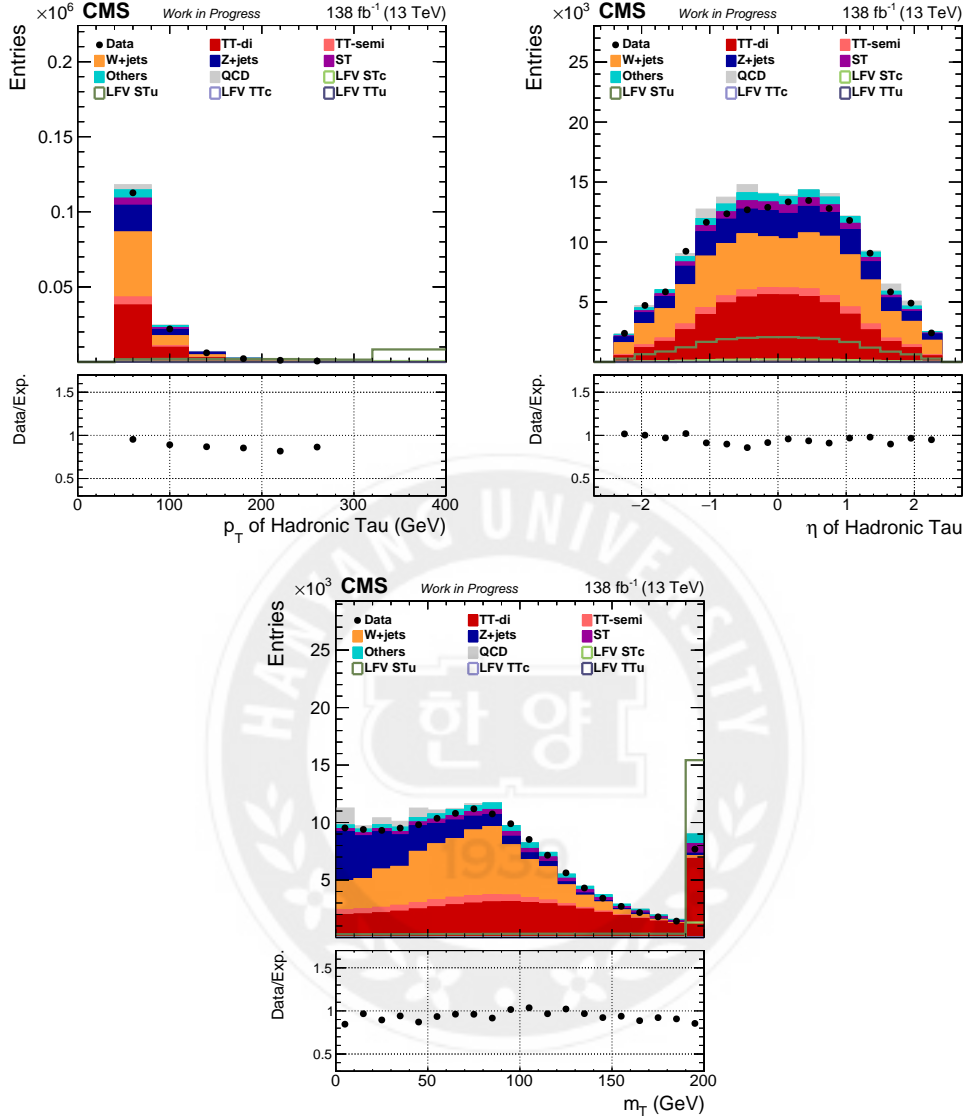


Figure 47: Control plots for p_T (left column) and η (right column) of selected muon (top row) and tau (middle row), and m_T reconstructed with the selected muon and MET (bottom row) (S2) in the category 1.

Step 3

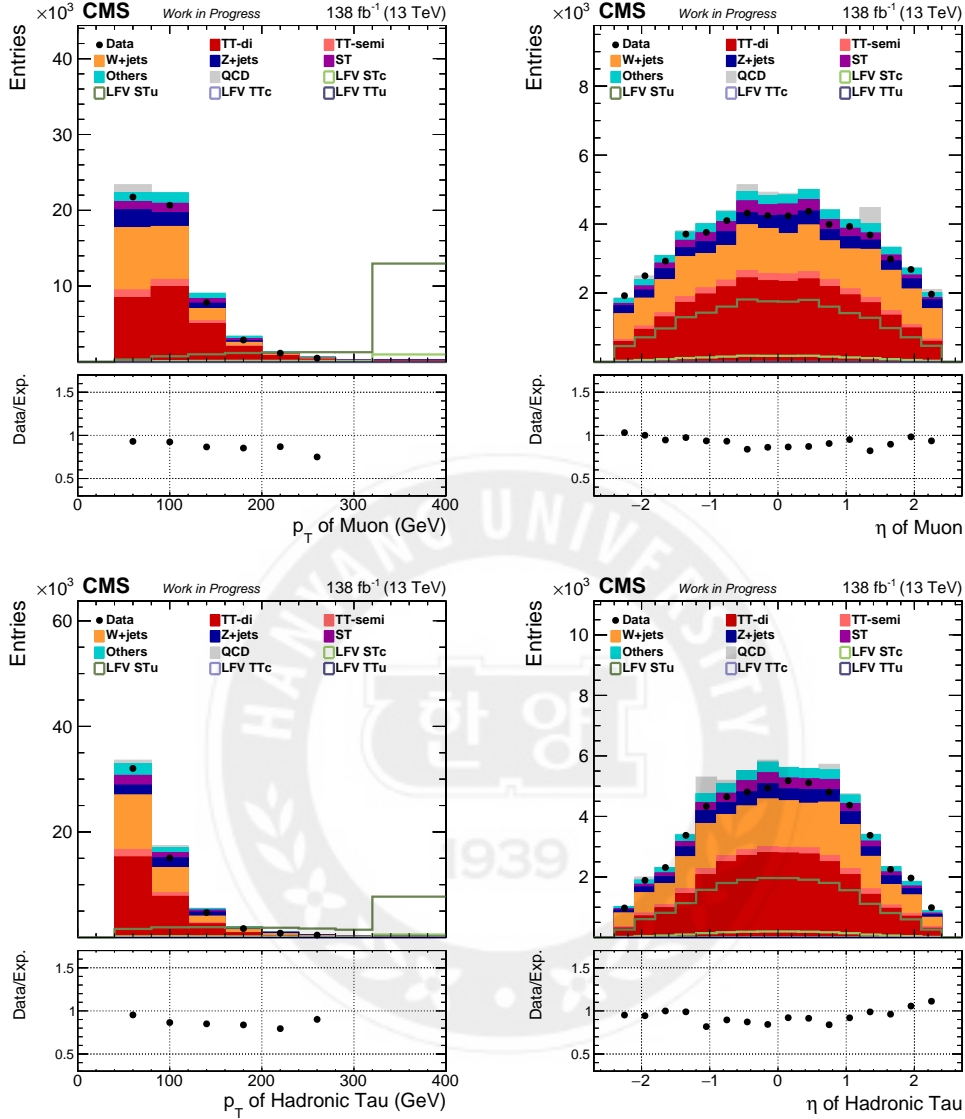


Figure 48: Control plots for p_T (left column) and η (right column) of selected muon (upper row) and tau (lower row)(S3) in the category 1.

Step 3

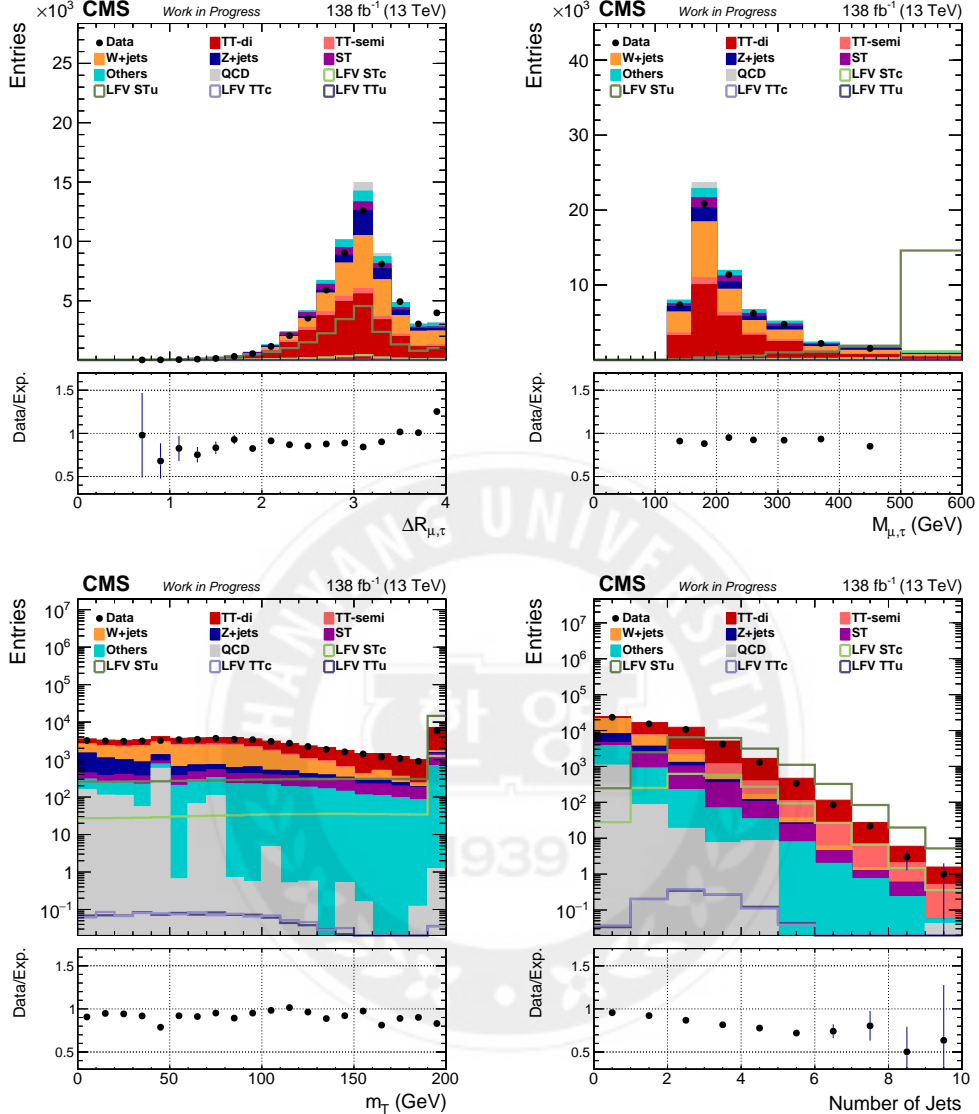


Figure 49: Control plots for ΔR (upper left) and mass (upper right) reconstructed with the selected muon and tau (S3) in the category 1. Plots of m_T reconstructed with the selected muon and MET (lower left) and the number of jets (lower right) (S3) in the category 1.

Step 4

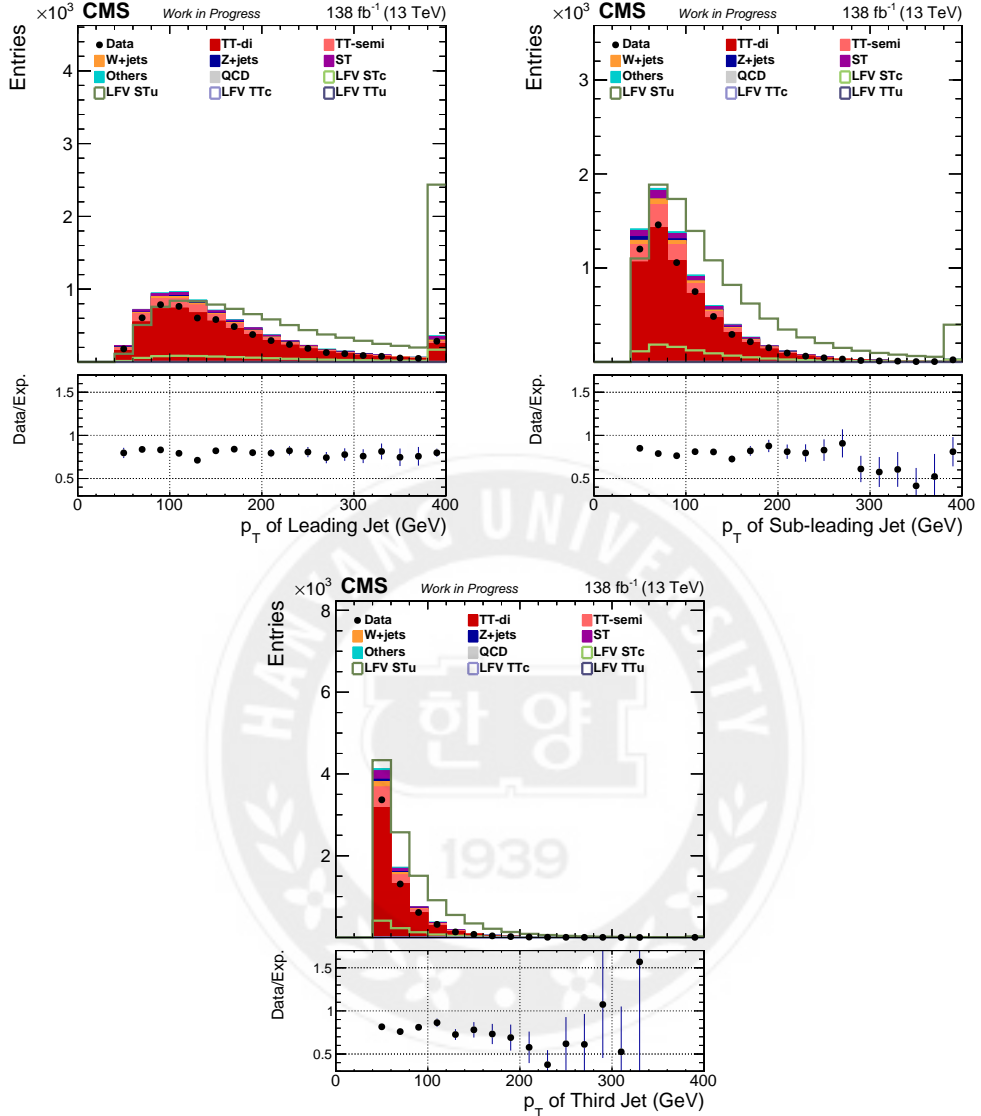


Figure 50: Control plots for p_T of the leading (upper left), sub-leading (upper right), and third jets (lower) (S4) in the category 1.

Step 4

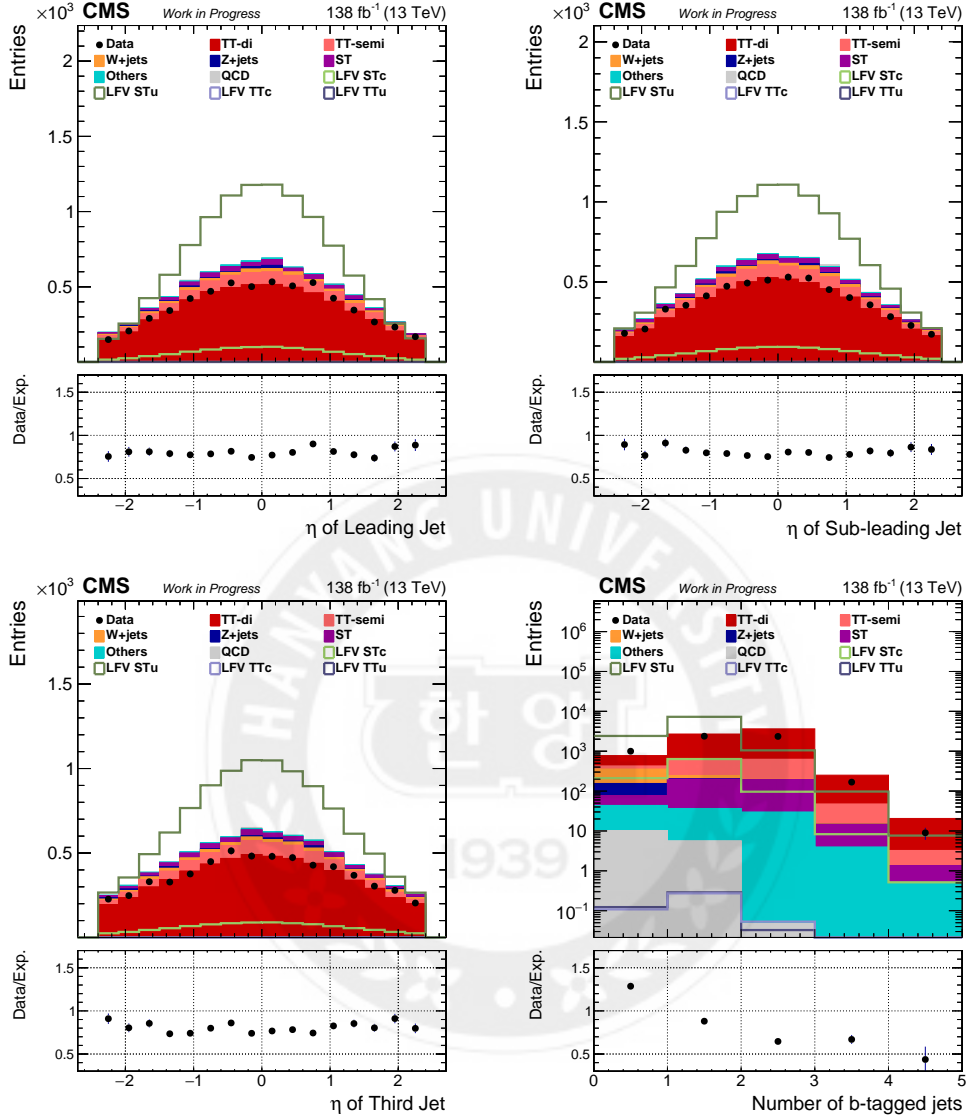


Figure 51: Control plots for η of the leading (upper left), sub-leading (upper right), and third jets (lower left), and the number of b-tagged jet (lower right) (S4) in the category 1.

Step 5 (Final)

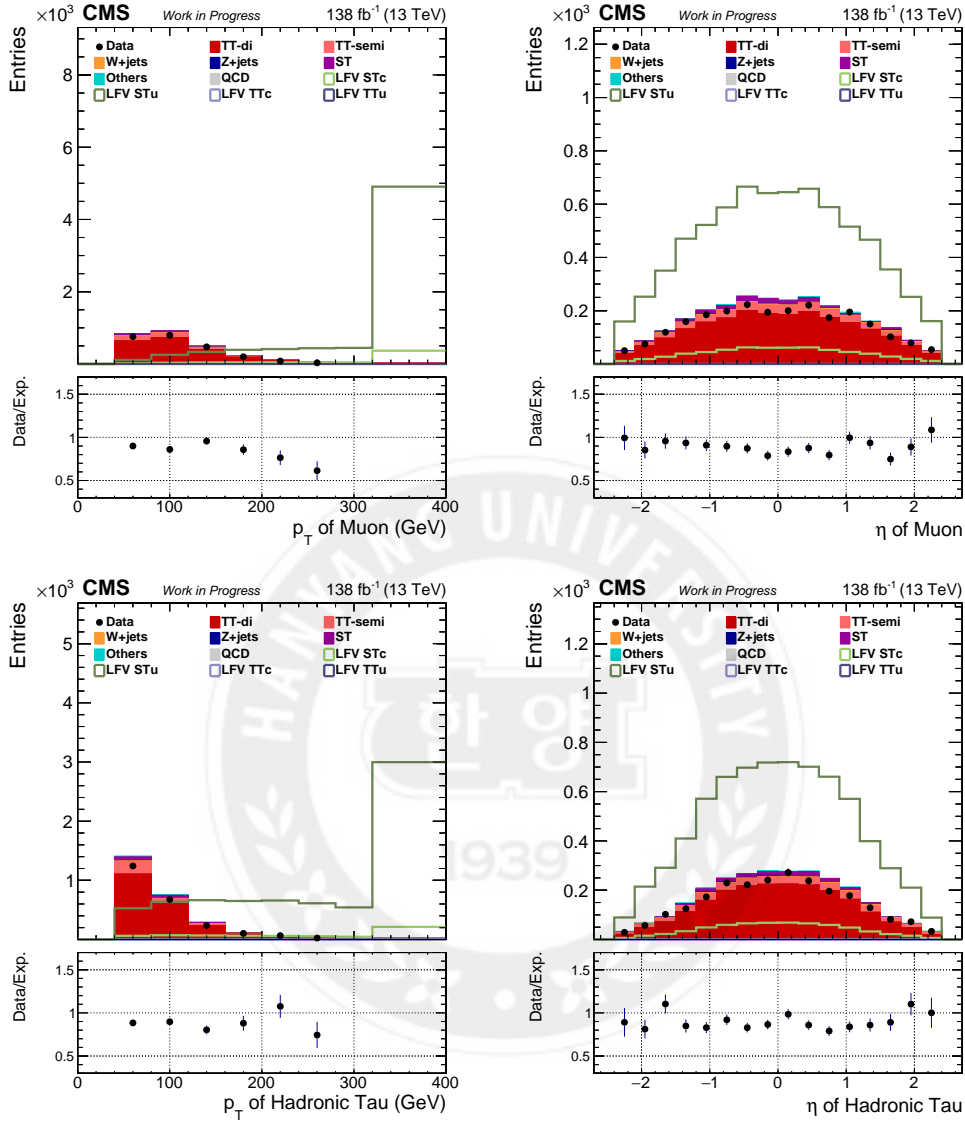


Figure 52: Control plots for p_T (left column) and η (right column) of selected muon (upper row) and tau (lower row) (S5) in the category 1.

Step 5 (Final)

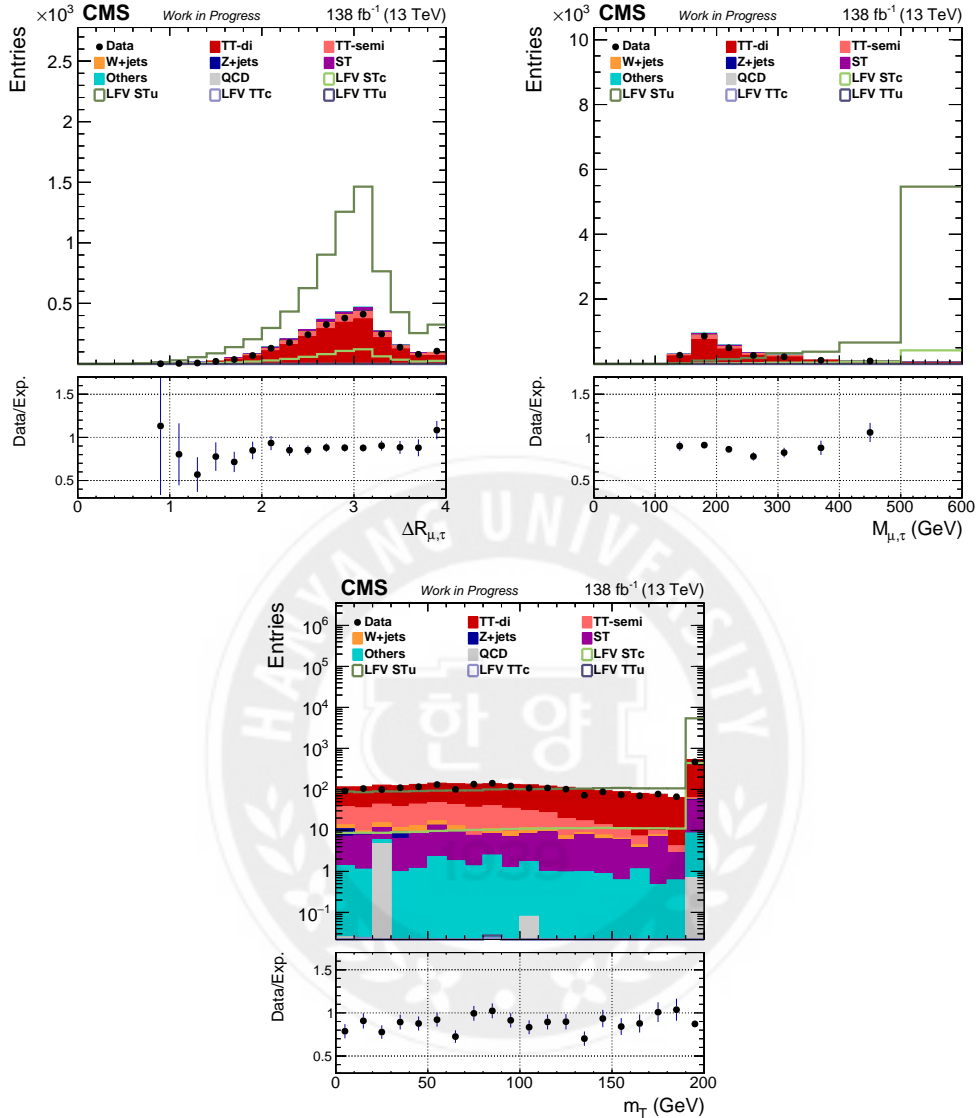


Figure 53: Control plots for ΔR (upper left) and mass (upper right) reconstructed with the selected muon and tau and m_T (lower) reconstructed with the selected muon and MET (S5) in the category 1.

Step 5 (Final)

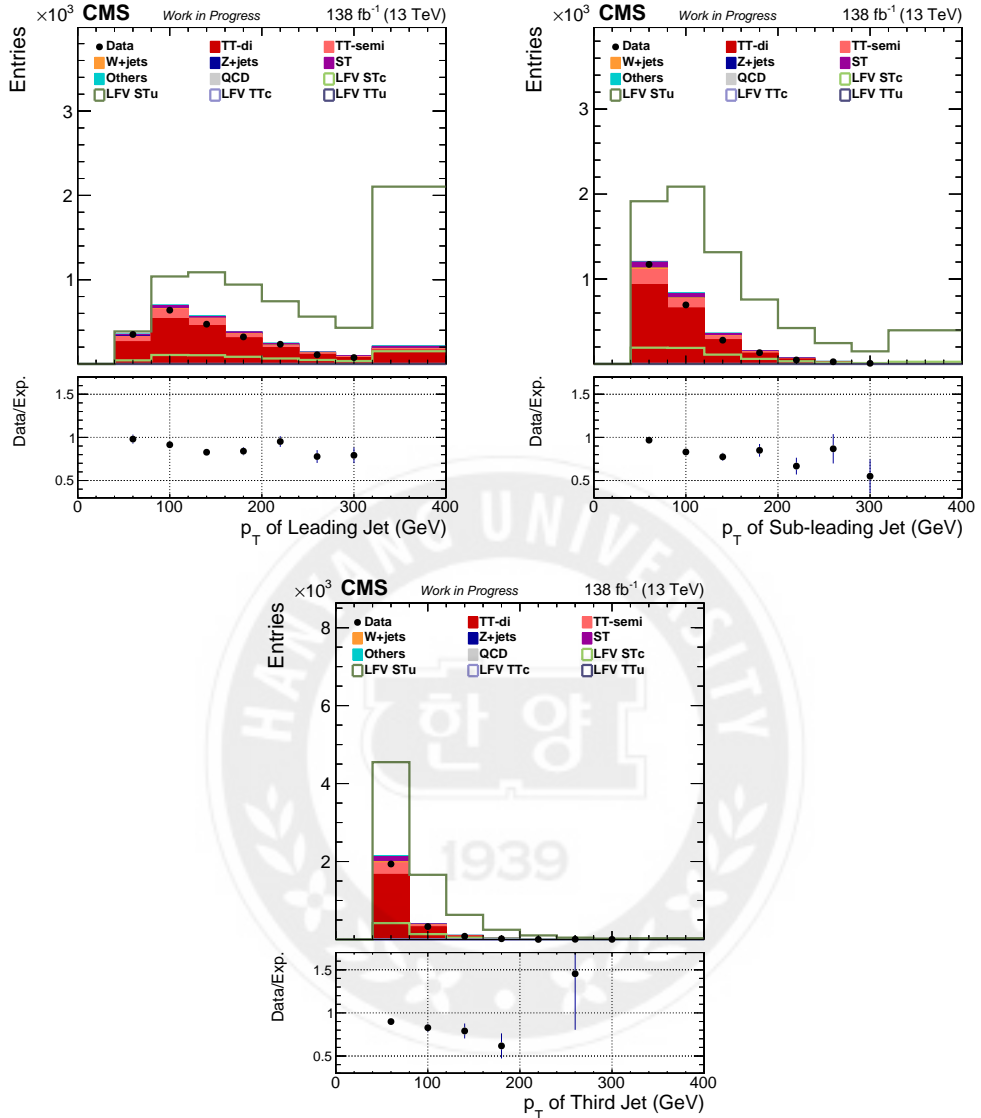


Figure 54: Control plots for p_T of the leading (upper left), sub-leading (upper right), and third jet (lower) (S5) in the category 1.

Step 5 (Final)

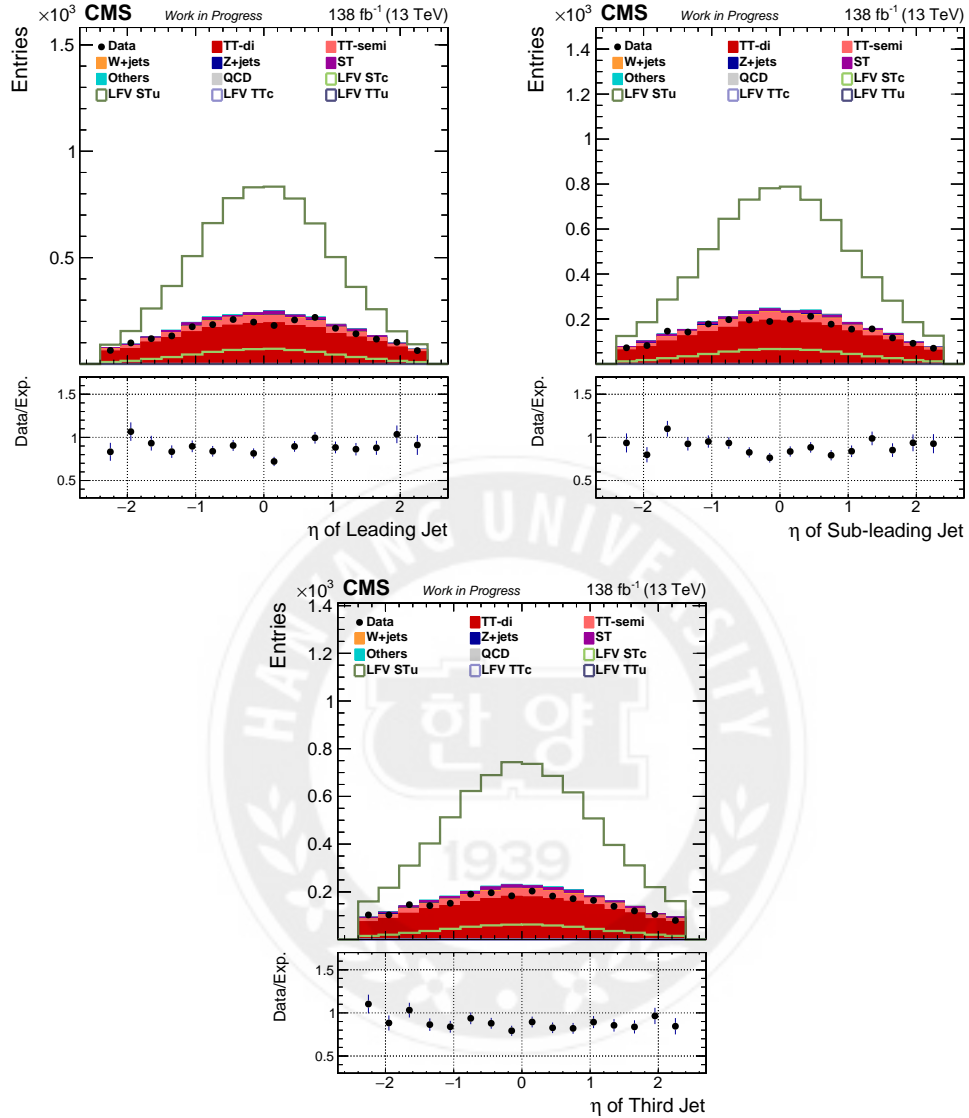


Figure 55: Control plots for η of the leading (upper left), sub-leading (upper right), and third jet (lower) (S5) in the category 1.

Step 5 (Final)

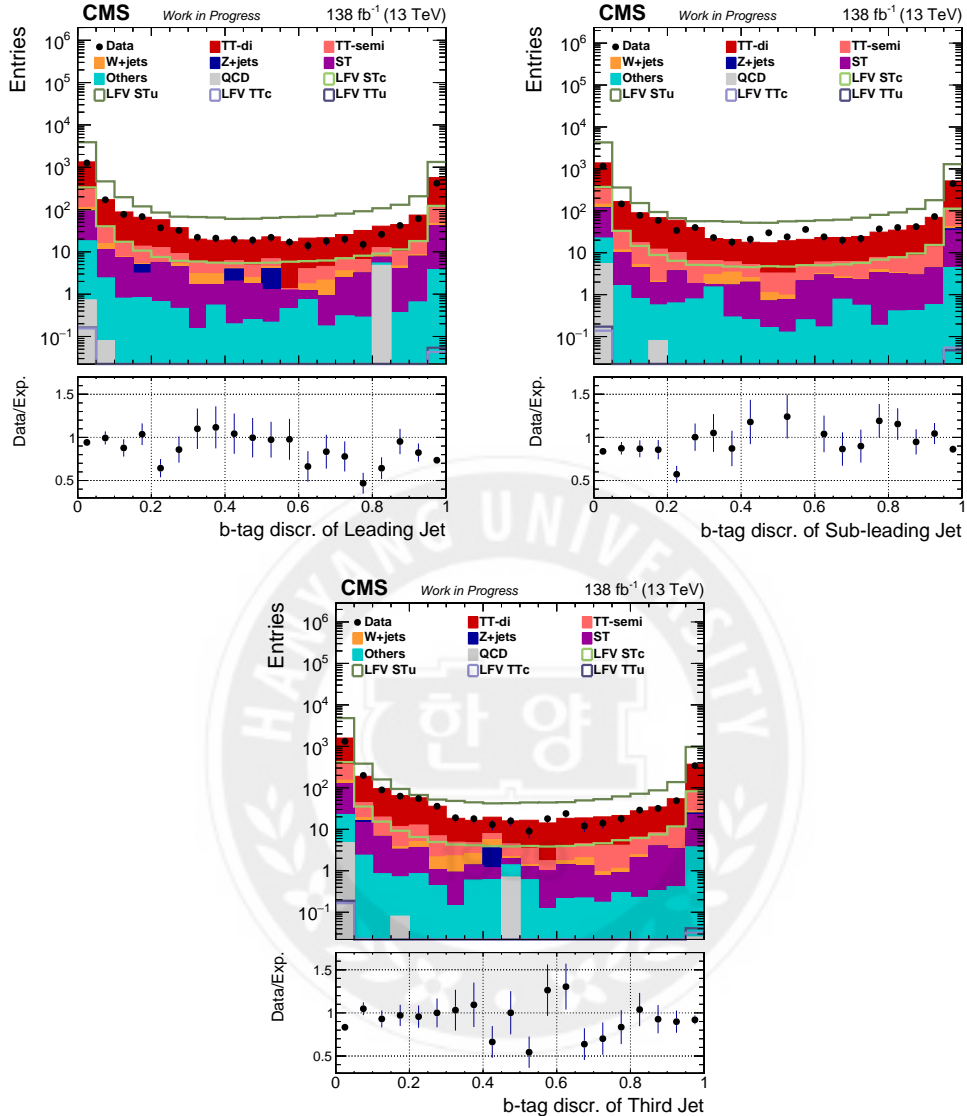


Figure 56: Control plots for b-tagging discriminator of the leading (upper left), sub-leading (upper right), and third jet (lower) (S5) in the category 1.

Step 5 (Final)

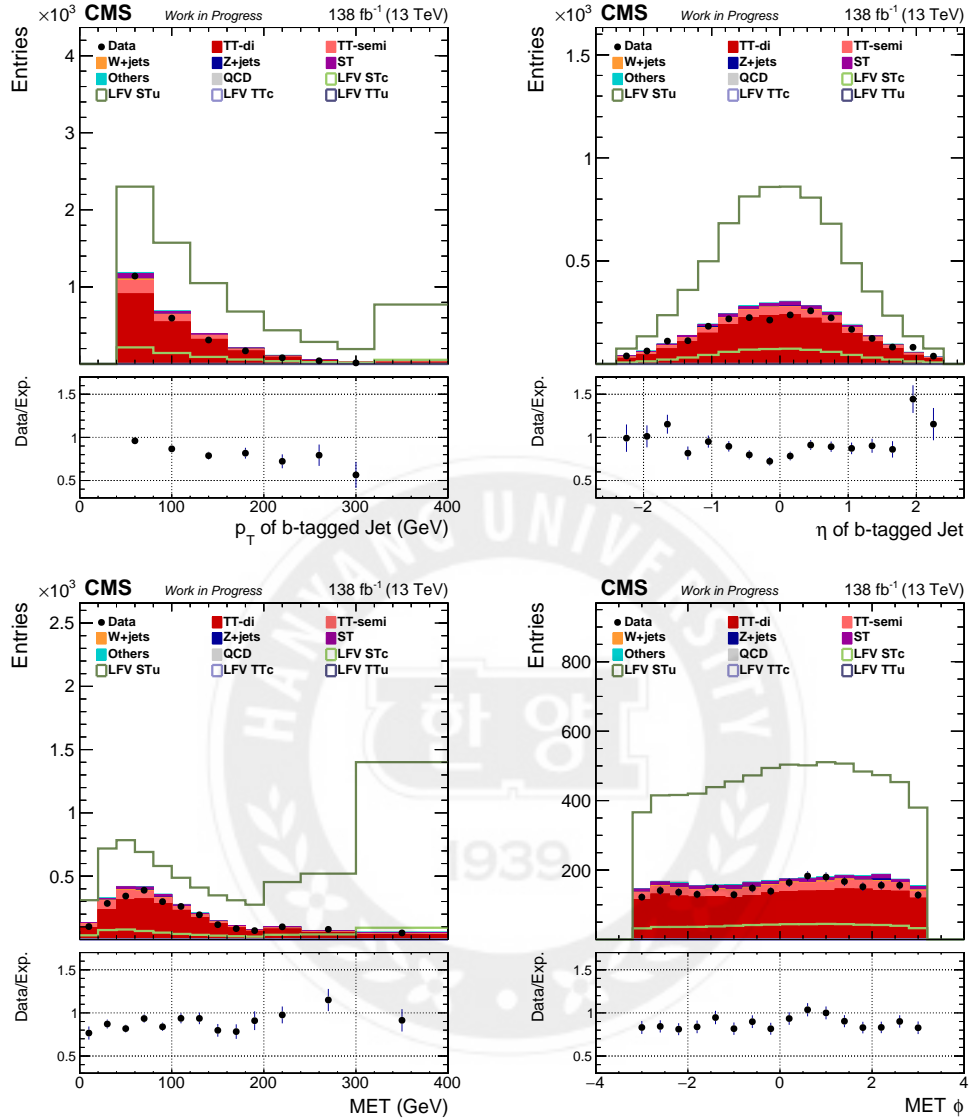


Figure 57: Control plots for p_T (upper left) and η (upper right) of the b-tagged jet, and MET (lower left) and ϕ of MET (lower right) (S5) in the category 1.

Category 2

Step 1

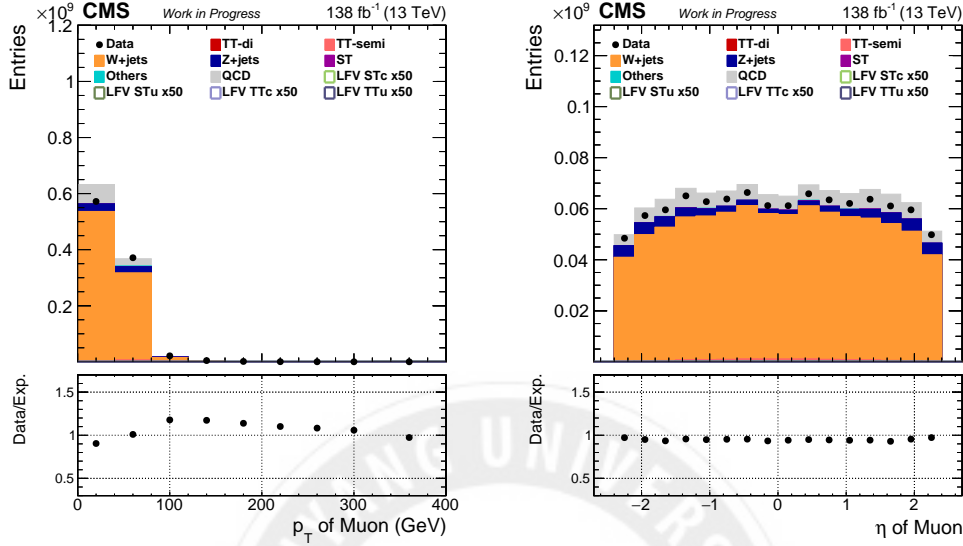


Figure 58: Control plots for p_T (left) and η (right) of selected muon (S1) in the category 2.

Step 2

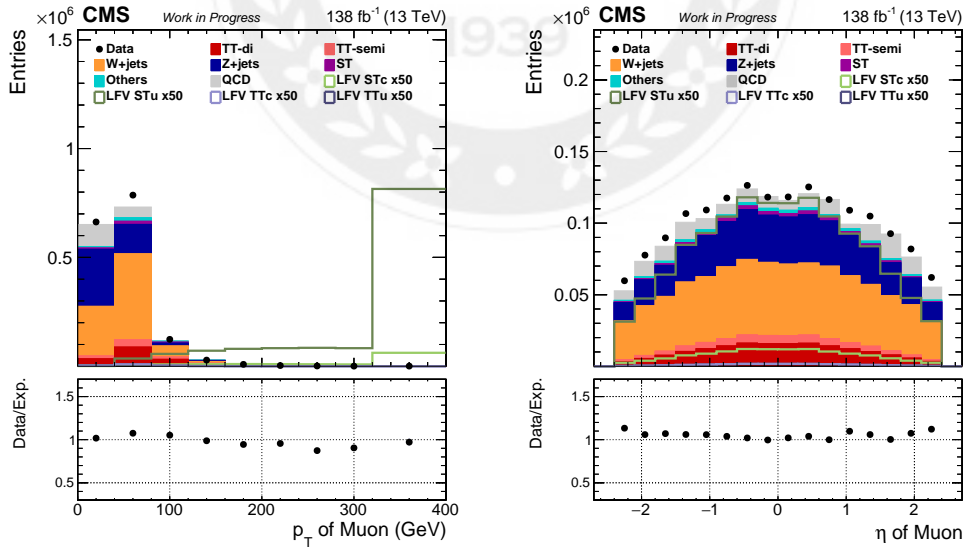


Figure 59: Control plots for p_T (left) and η (right) of selected muon (S2) in the category 2.

Step 2

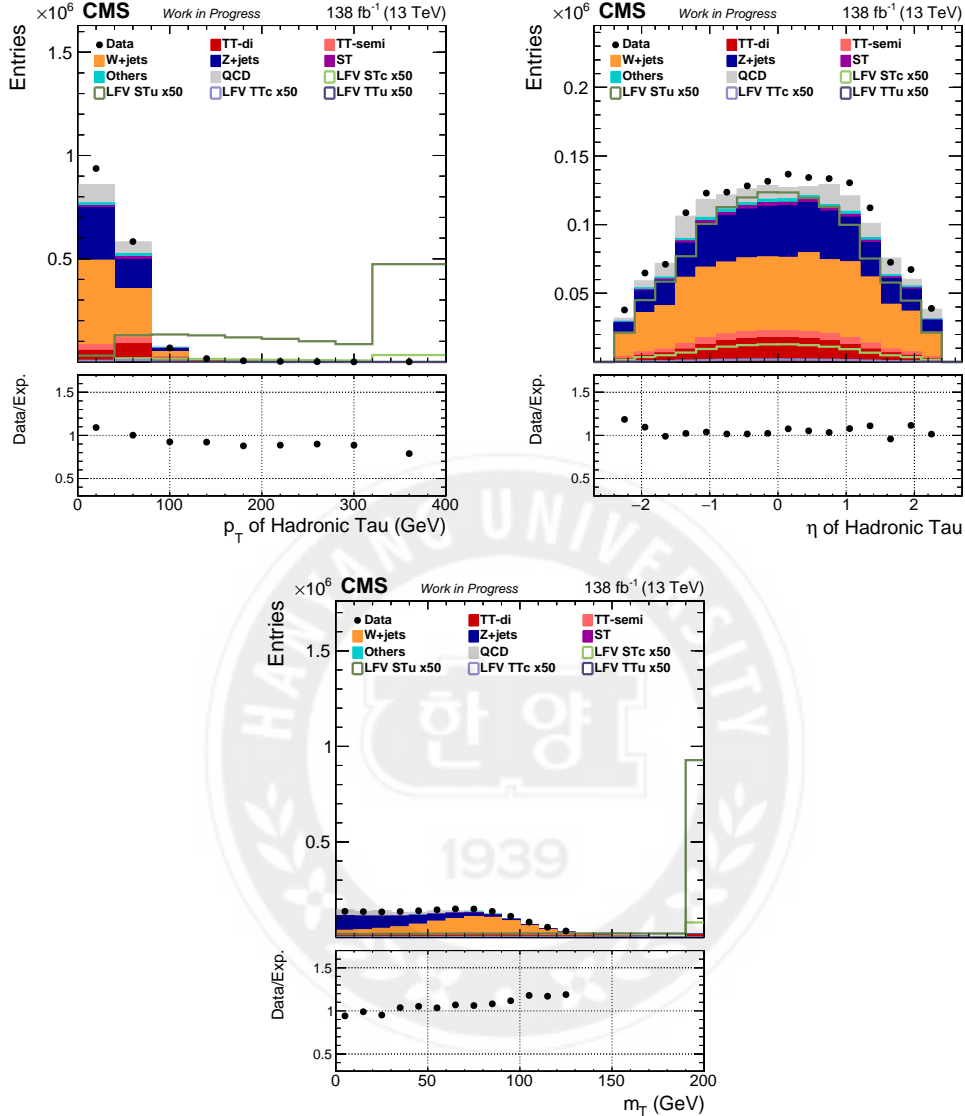


Figure 60: Control plots for p_T (upper left) and η (upper right) of the selected tau, and m_T (lower) reconstructed with the selected muon and MET (S2) in the category 2.

Step 3

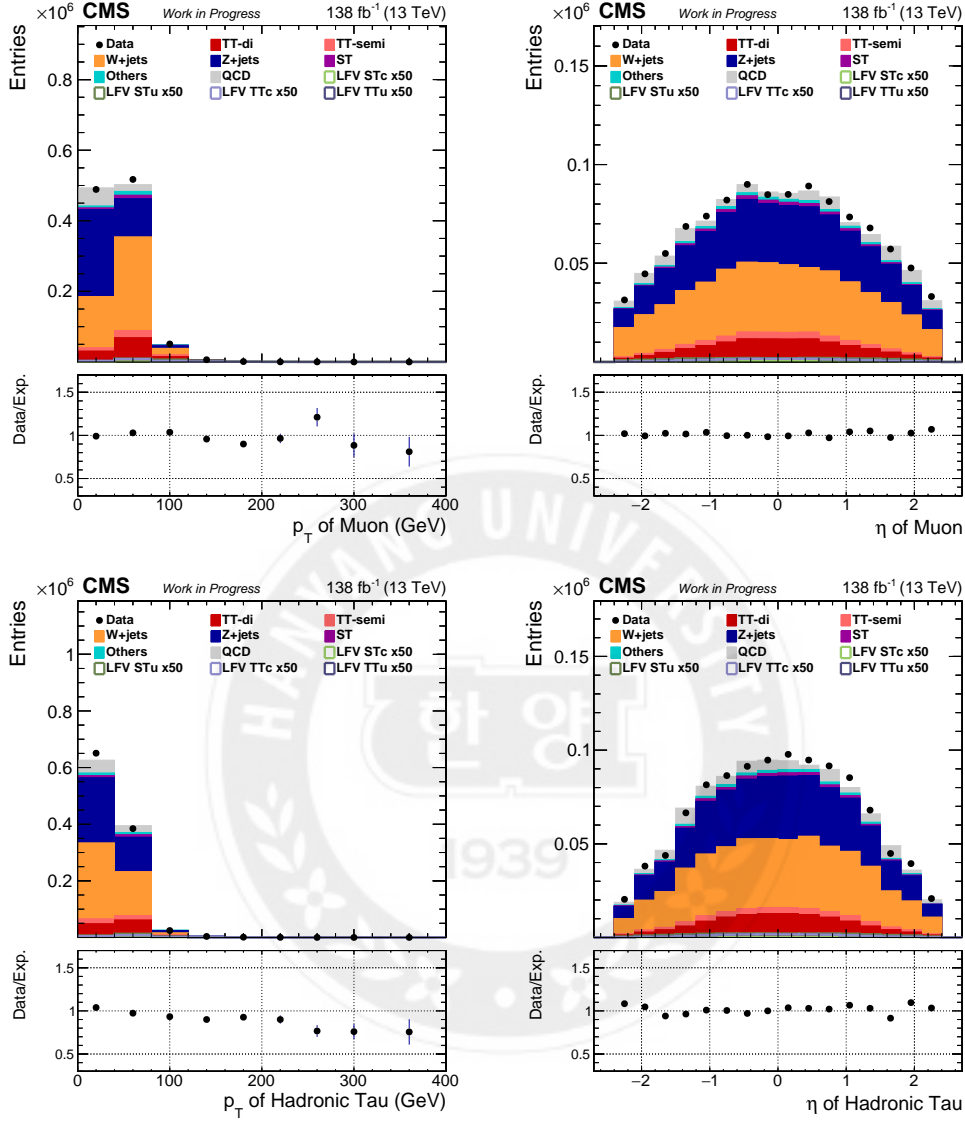


Figure 61: Control plots for p_T (left column) and η (right column) of selected muon (upper row) and tau (lower row) (S3) in the category 2.

Step 3

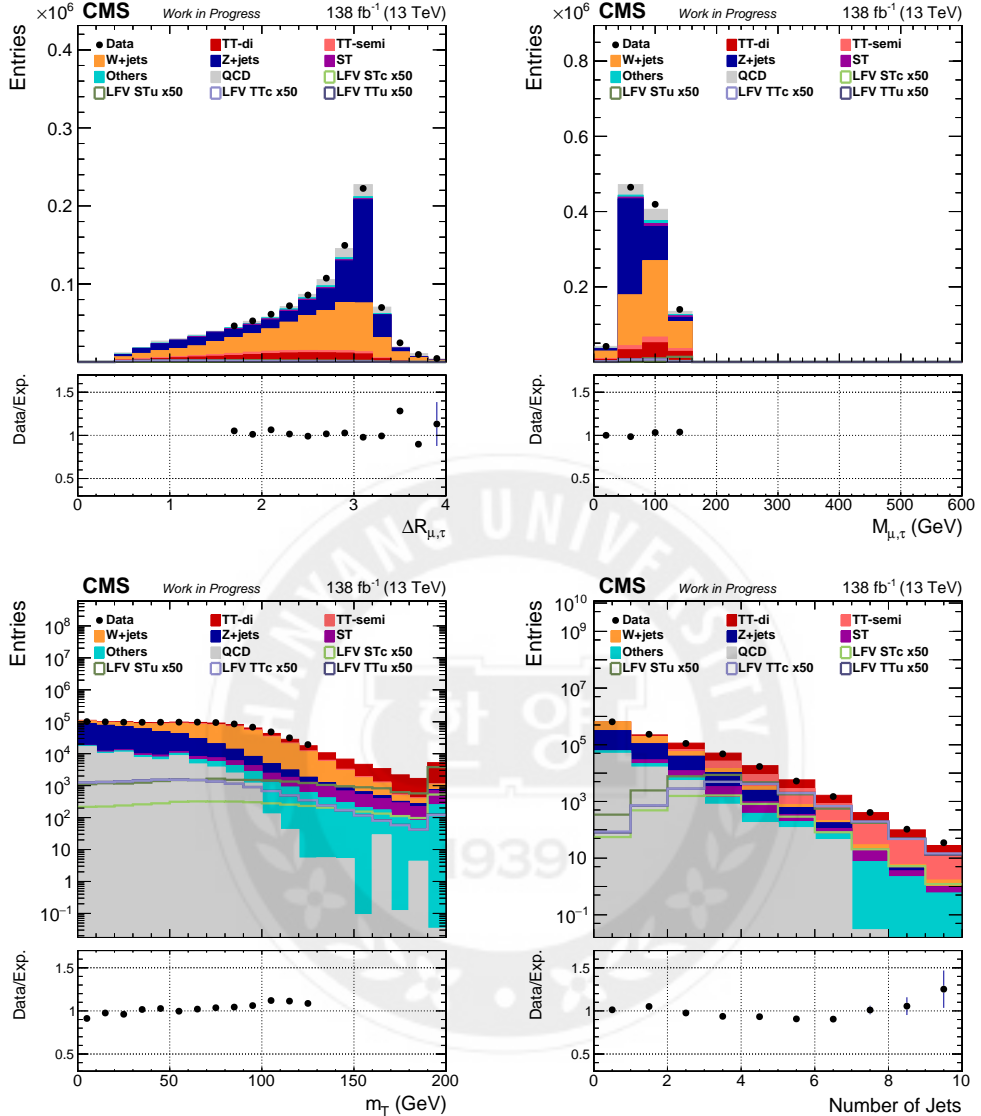


Figure 62: Control plots for ΔR (upper left) and *mass* (upper right) reconstructed with the selected muon and tau (S3) in the category 2. Plots of m_T (lower left) reconstructed with the selected muon and MET and the number of jets (lower right) (S3) in the category 2.

Step 4

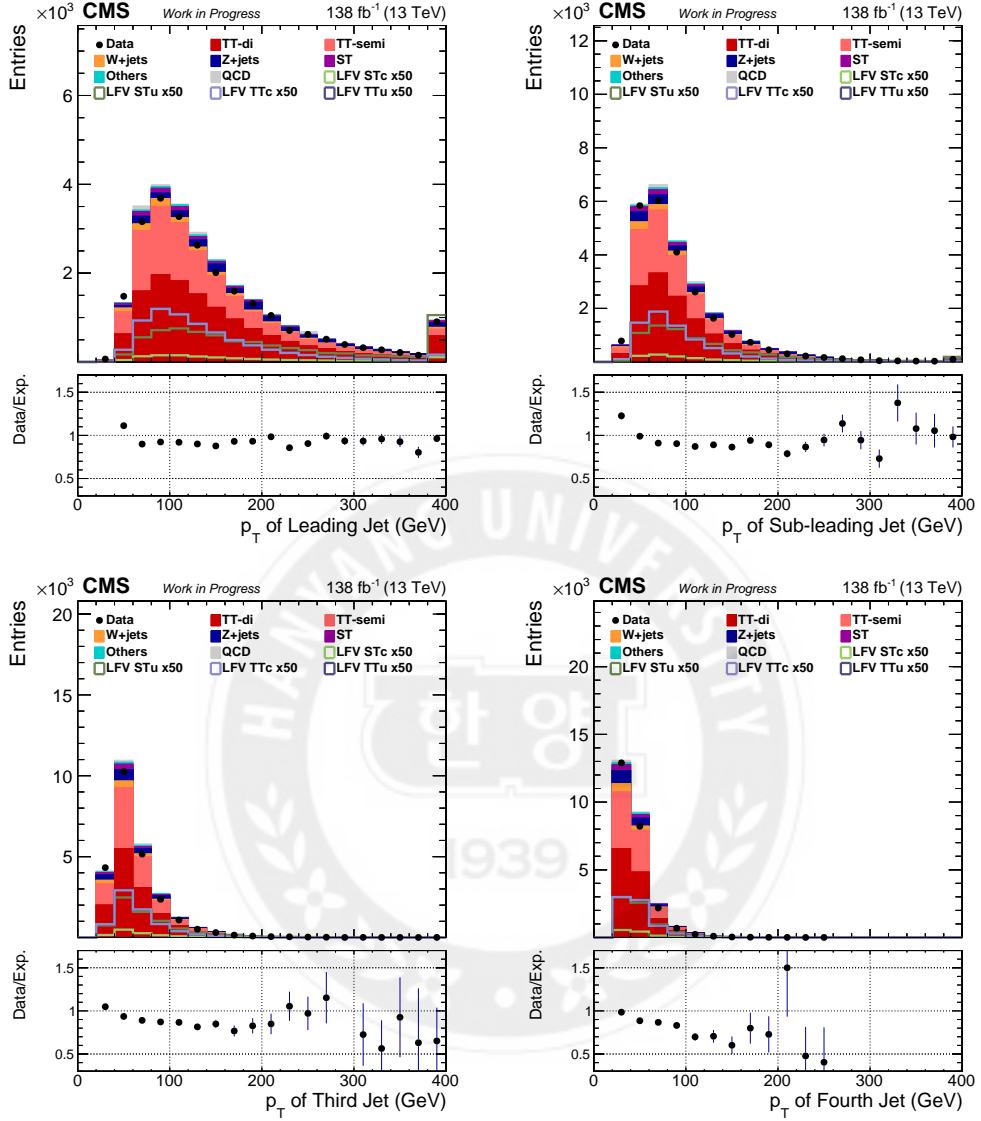


Figure 63: Control plots for p_T of the leading (upper left), sub-leading (upper right), third (lower left), and fourth (lower right) jets (S4) in the category 2.

Step 4

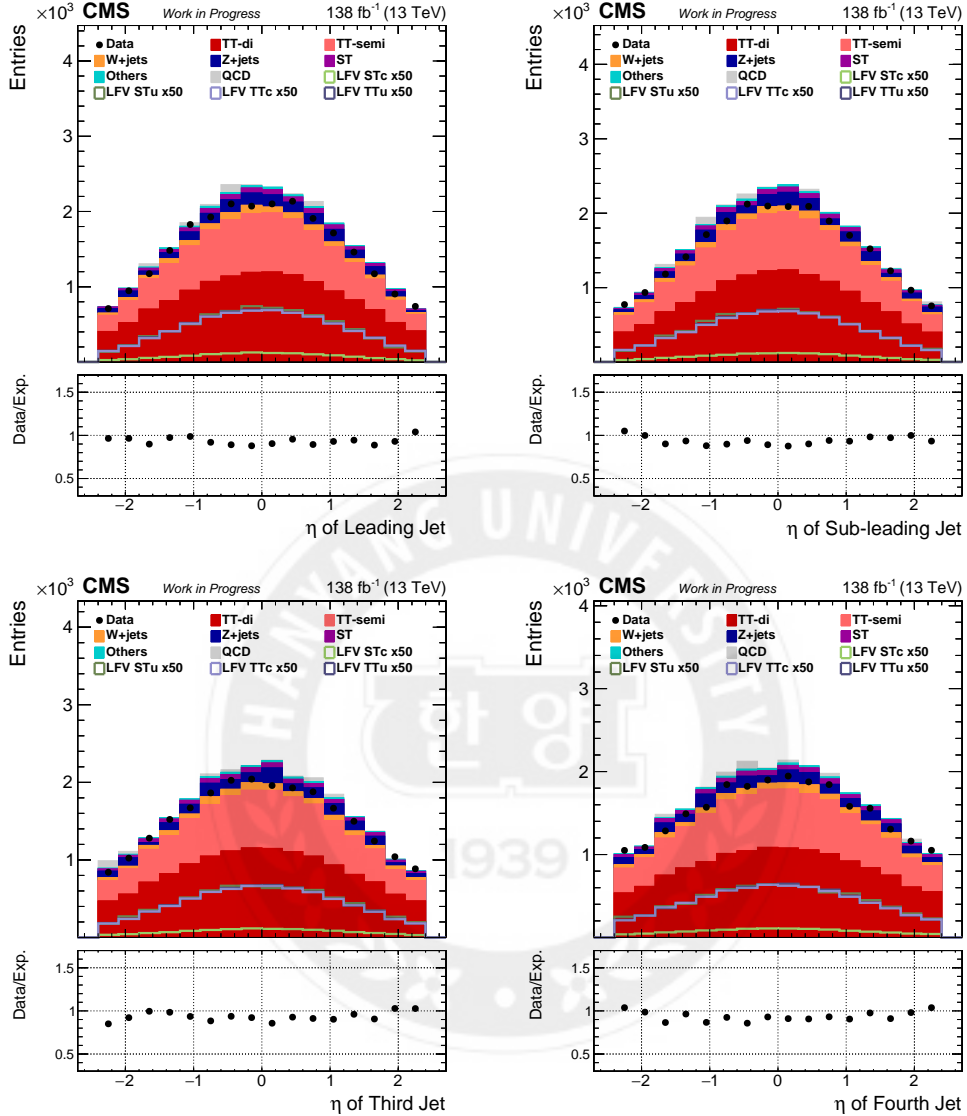


Figure 64: Control plots for η of the leading (upper left), sub-leading (upper right), third (lower left), and fourth (lower right) jets (S4) in the category 2.

Step 5

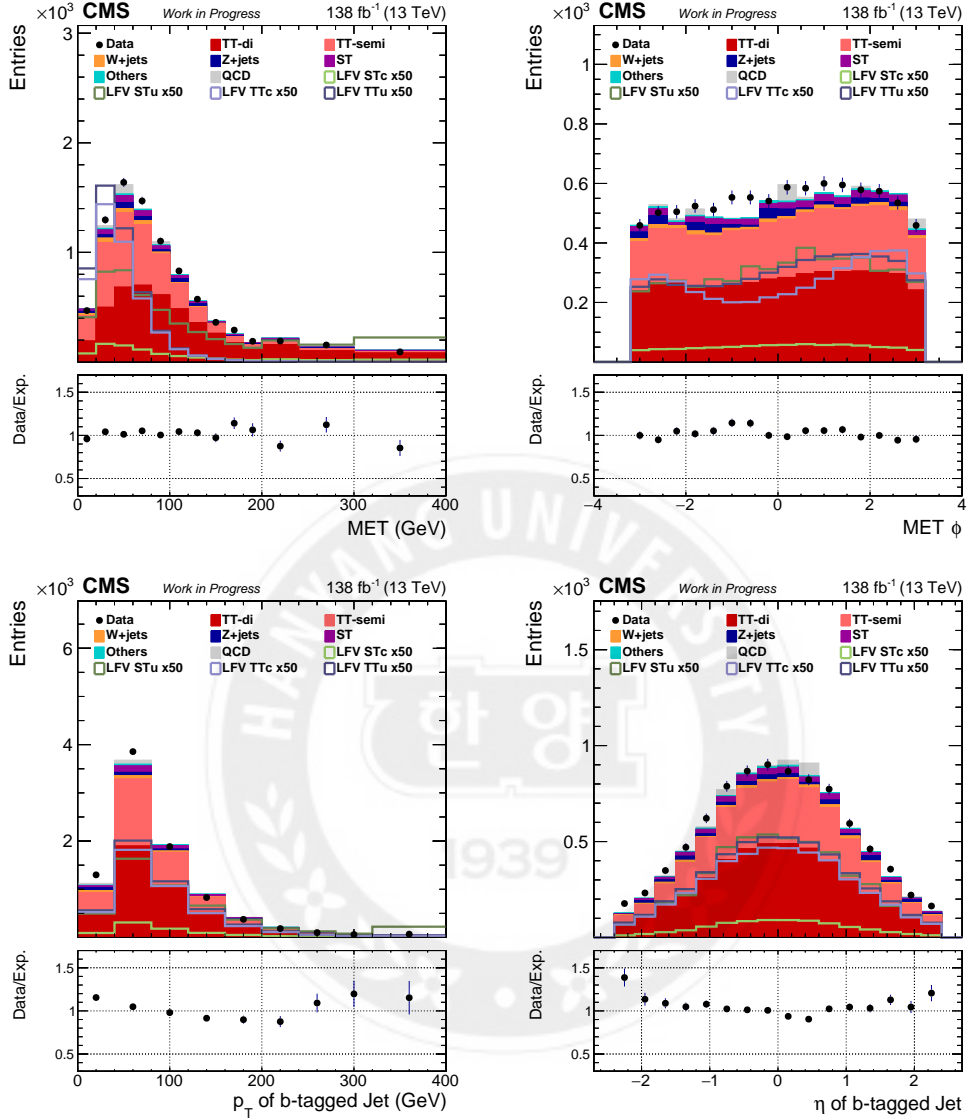


Figure 65: Control plots for MET (upper left), ϕ of MET (upper right), p_T (lower left) and η (lower right) of b-tagged jet (S5) in the category 2.

Step 6 (Final)

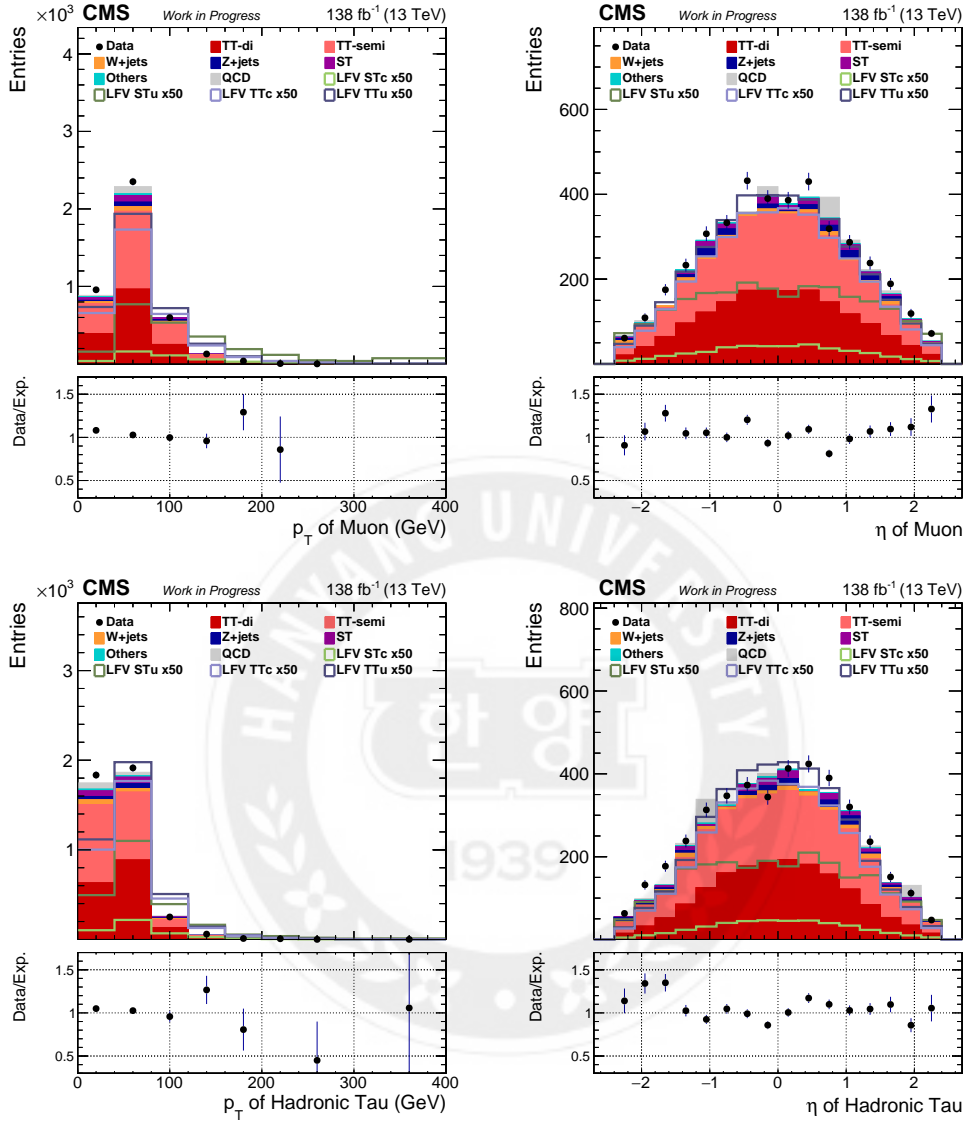


Figure 66: Control plots for p_T (left column) and η (right column) of selected muon (upper row) and tau (lower row) (S6) in the category 2.

Step 6 (Final)

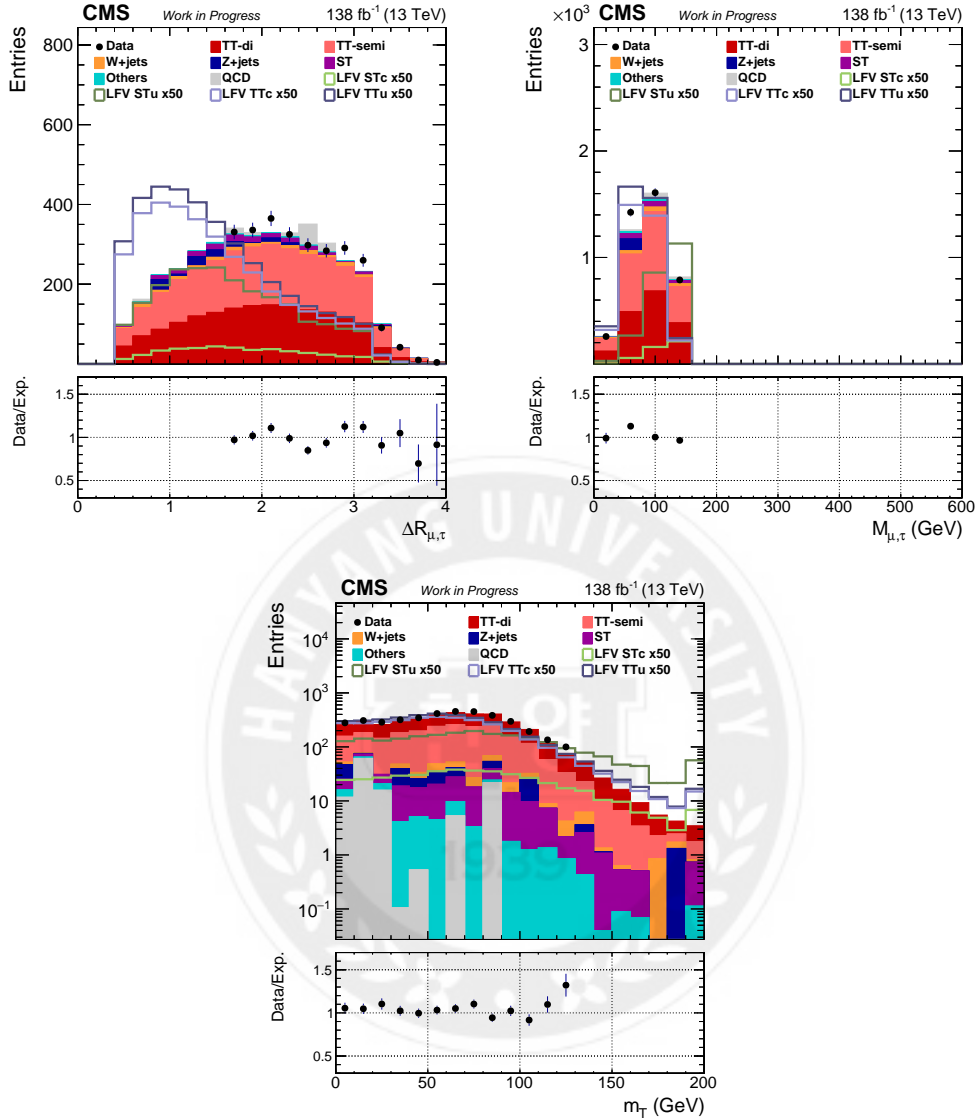


Figure 67: Control plots for ΔR (upper left) and mass (upper right) reconstructed with the selected muon and tau, and m_T (lower) reconstructed with the selected muon and MET (S6) in the category 2.

Step 6 (Final)

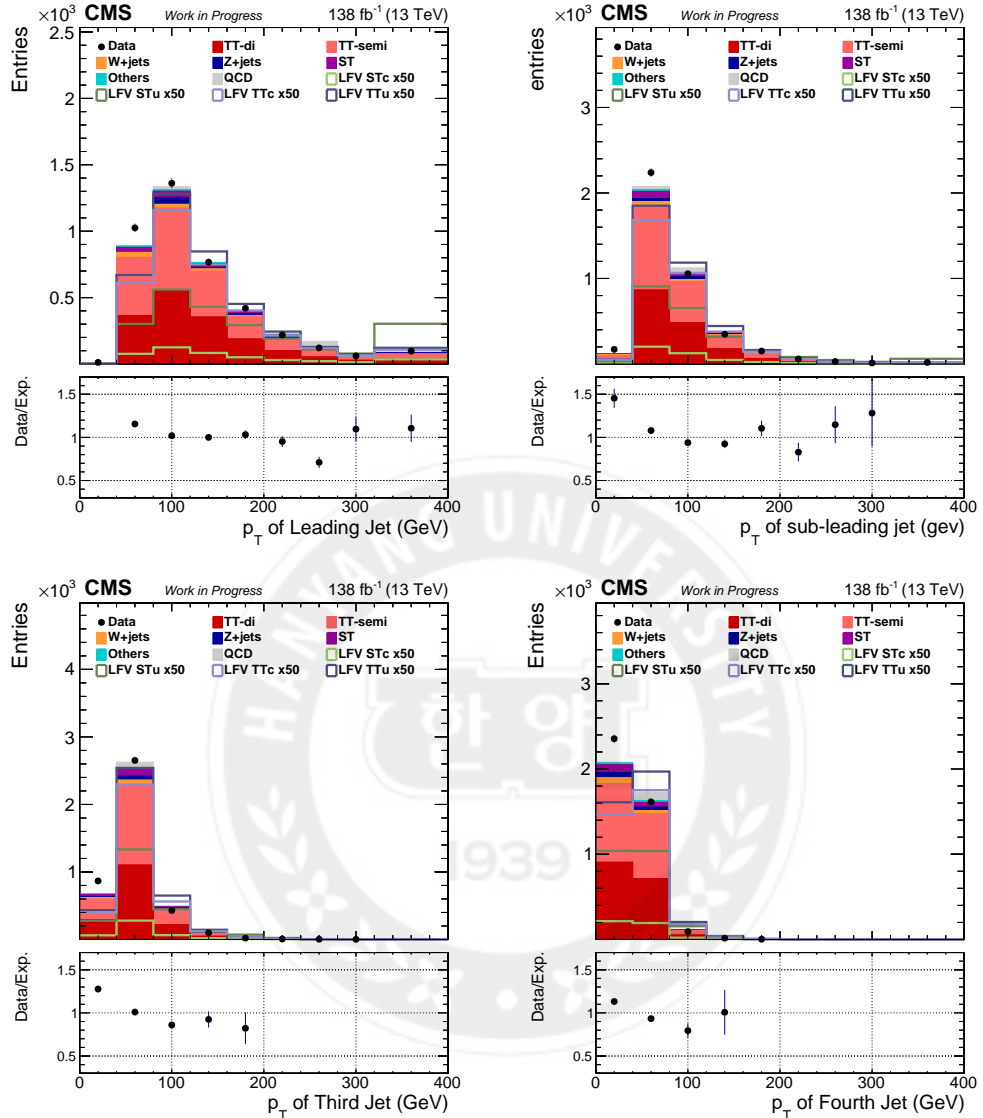


Figure 68: Control plots for p_T of the leading (upper left), sub-leading (upper right), third (lower left), fourth (lower right) (S6) in the category 2.

Step 6 (Final)

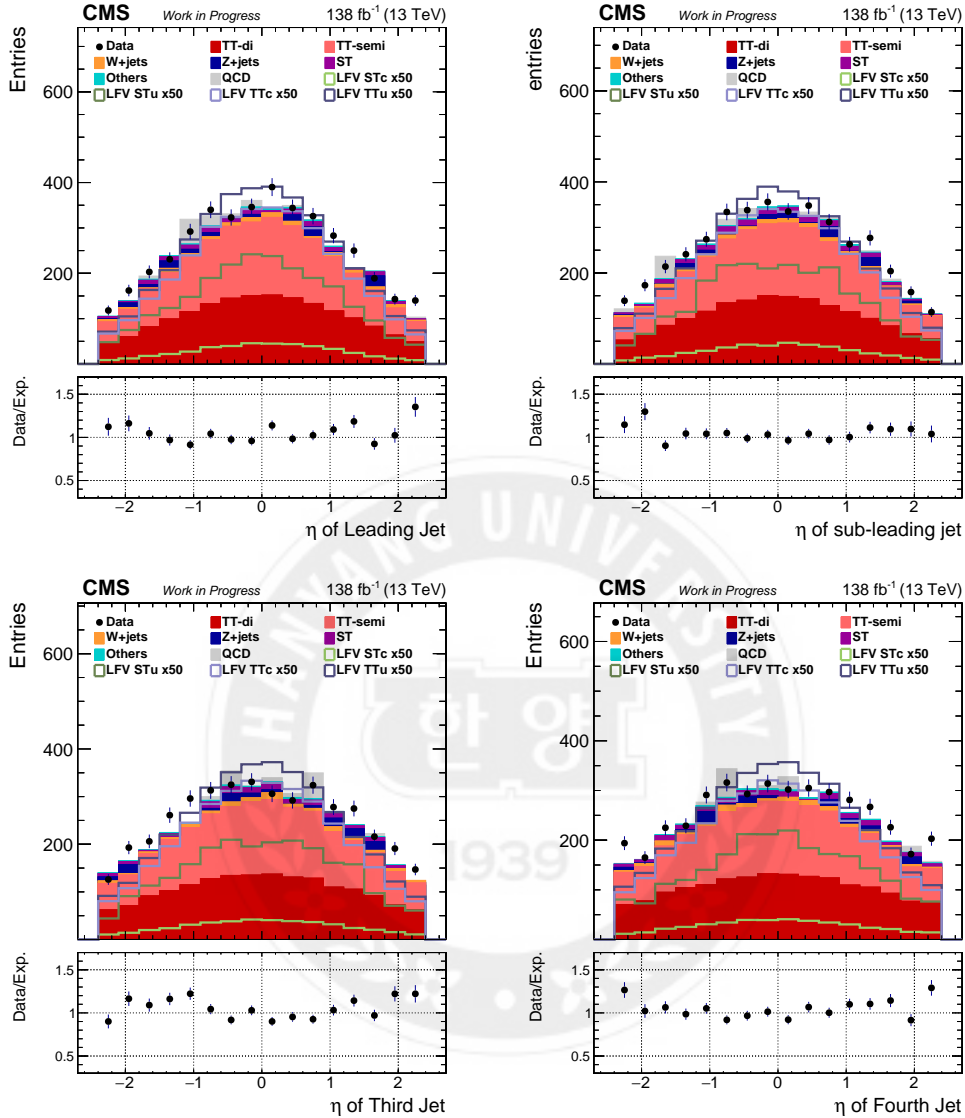


Figure 69: Control plots for η of the leading (upper left), sub-leading (upper right), third (lower left), fourth (lower right) (S6) in the category 2.

Step 6 (Final)

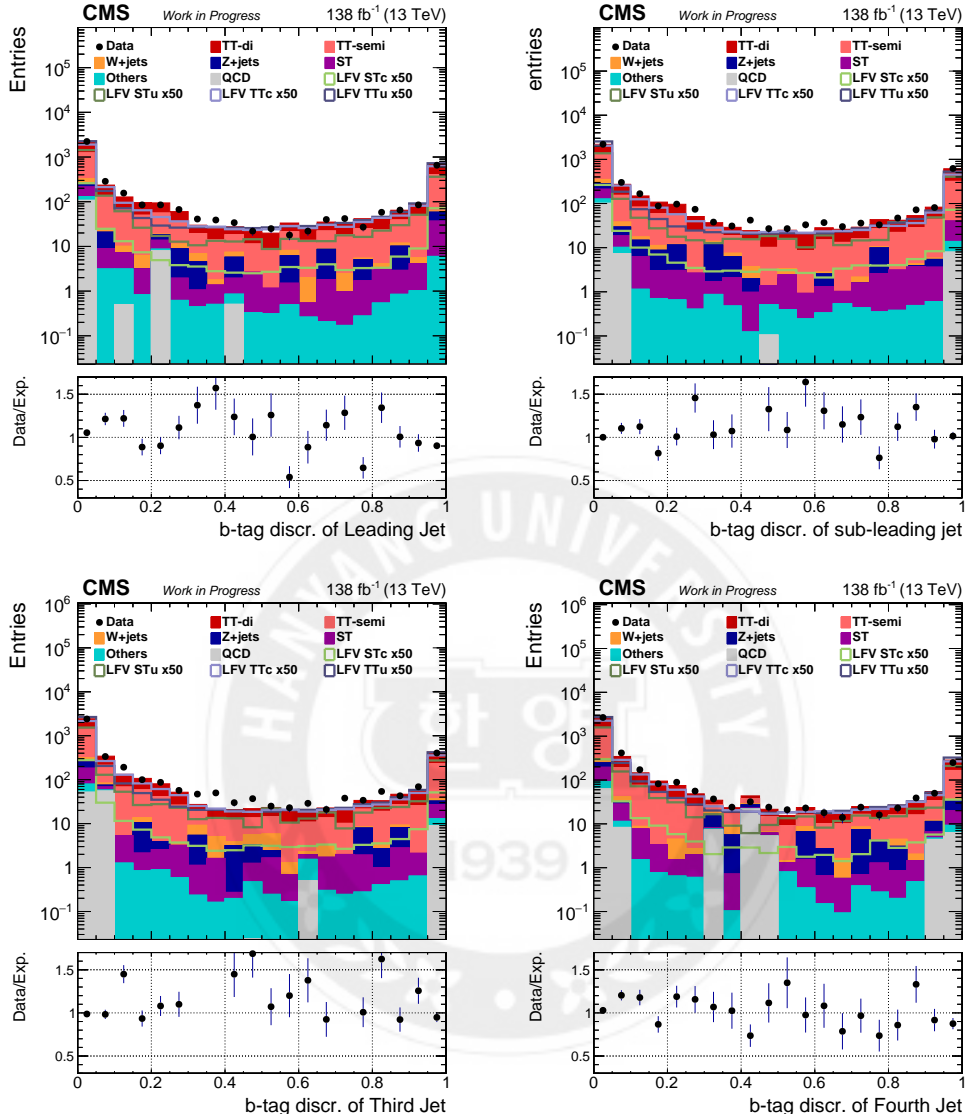


Figure 70: Control plots for b-tagging discriminator of the leading (upper left), sub-leading (upper right), third (lower left), fourth (lower right) (S6) in the category 2.

Step 6 (Final)

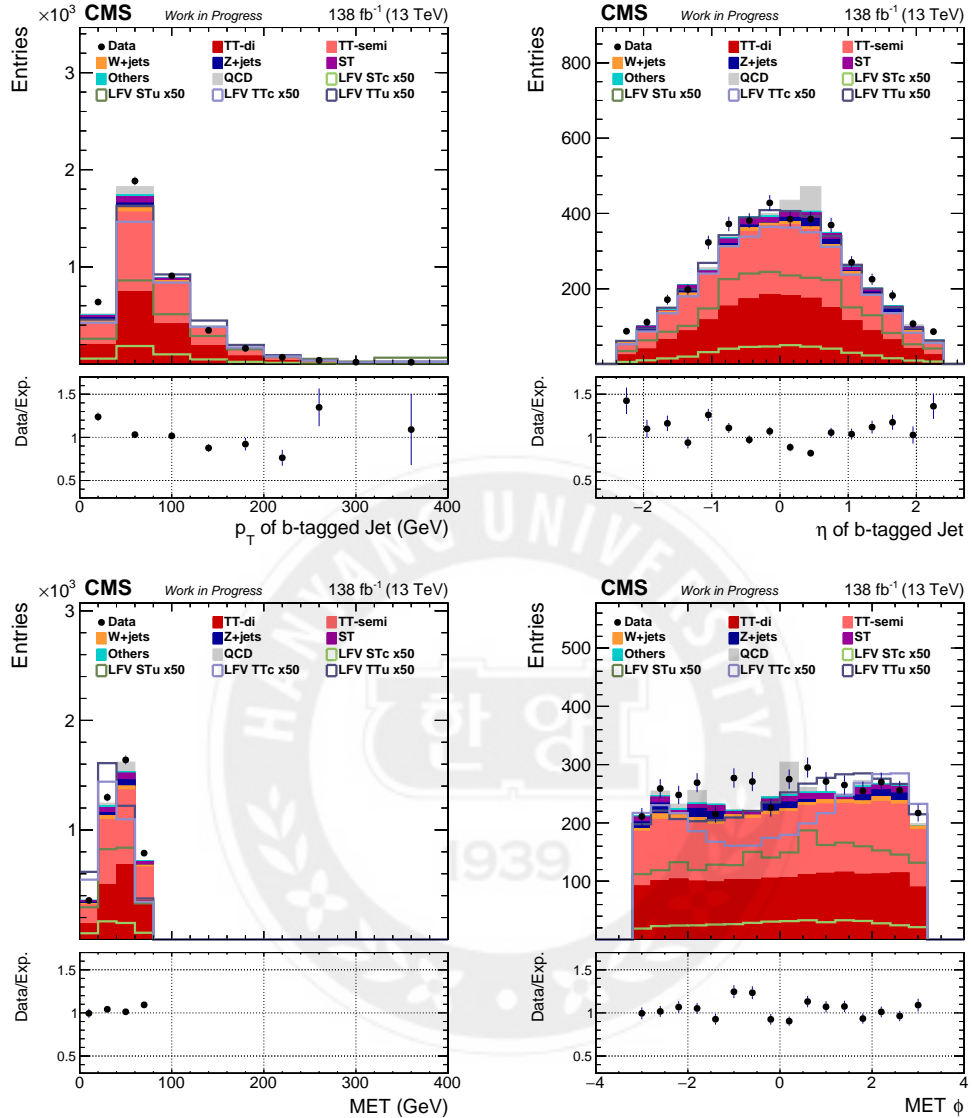


Figure 71: Control plots for p_T (upper left) and η (upper right) of the b-tagged jet, and MET (lower left) and ϕ of MET (lower right) (S6) in the category 2.

Appendix II. DNN Train Results – Accuracy and Loss

Train Accuracy

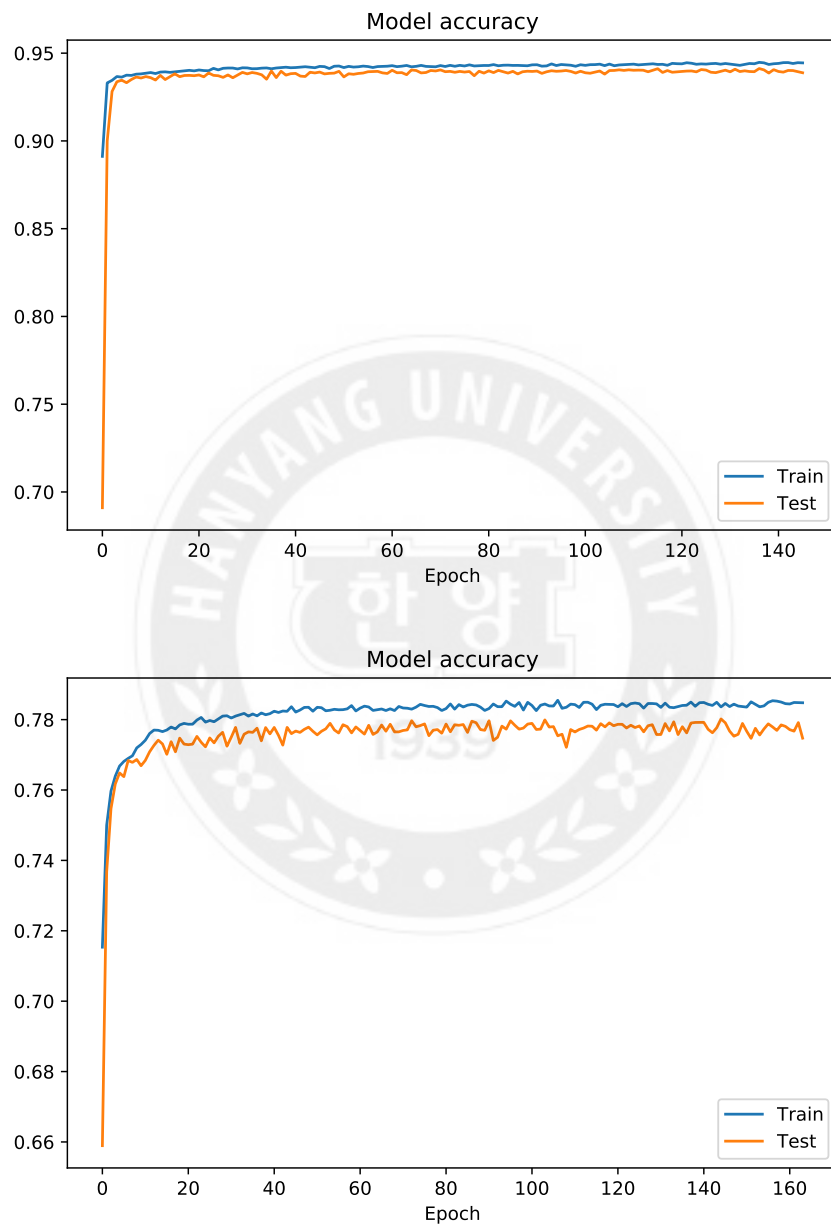


Figure 72: Accuracy per epoch distributions when training for the category 1 (upper) and 2 (lower).

Train Loss

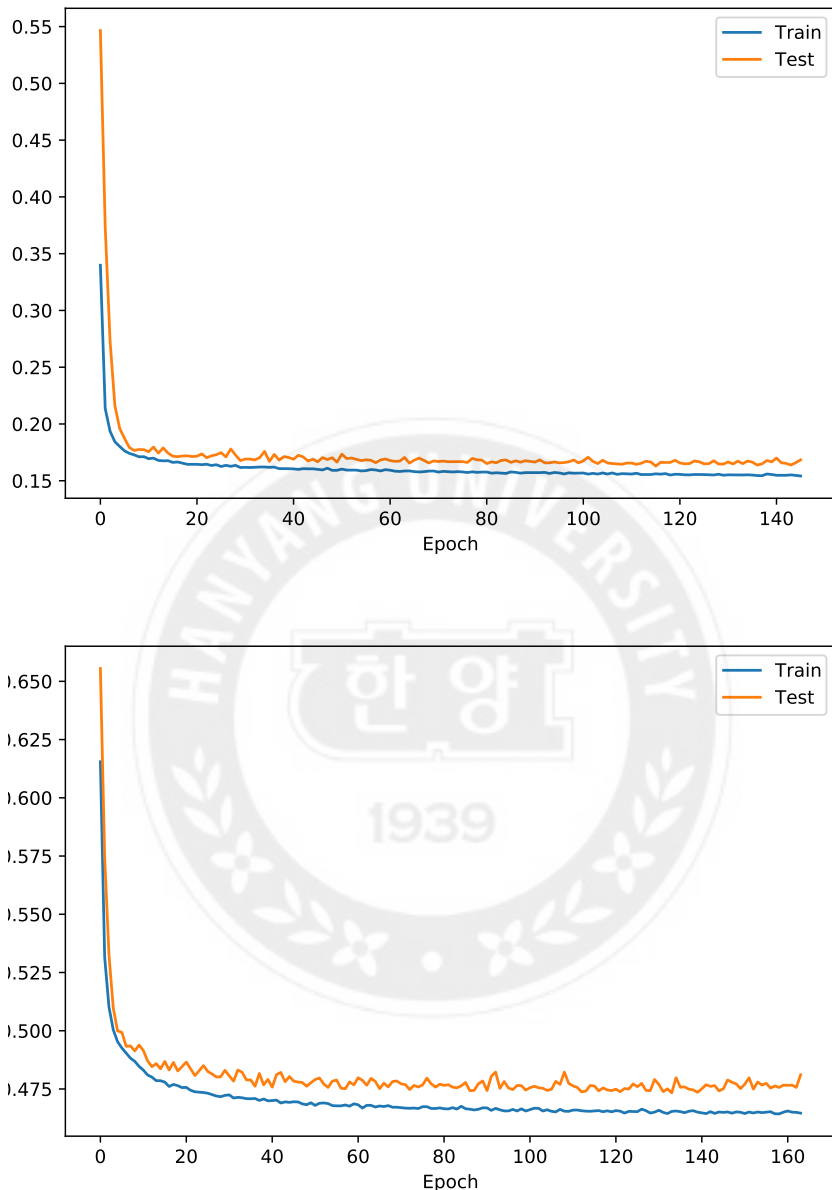
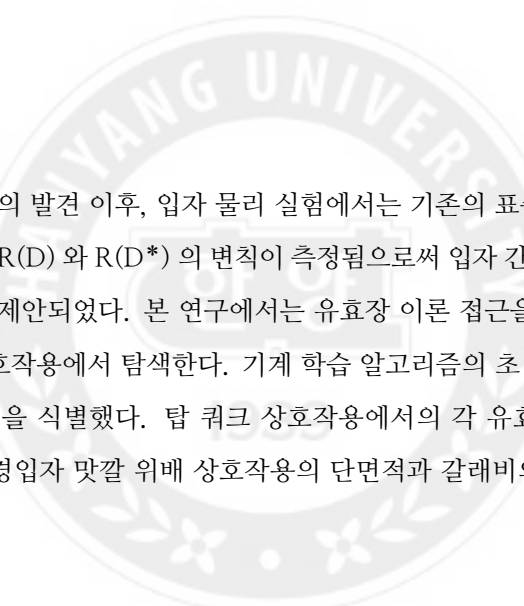


Figure 73: Loss per epoch distributions when training for the category 1 (upper) and 2 (lower).

국문요지



2012년 힉스 입자의 발견 이후, 입자 물리 실험에서는 기존의 표준 모형을 벗어난 새로운 물리 현상을 찾아왔다. $R(D)$ 와 $R(D^*)$ 의 변칙이 측정됨으로써 입자 간의 상호 작용에서 경입자 맷깔의 위배 가능성이 제안되었다. 본 연구에서는 유효장 이론 접근을 통한 경입자 맷깔 위배 현상을 탑큐크와의 상호작용에서 탐색한다. 기계 학습 알고리즘의 초 매개 변수를 최적화하여 경입자 맷깔 위배 사건을 식별했다. 탑 큐크 상호작용에서의 각 유효 연산자의 월슨 계수의 상한값을 설정하면서 경입자 맷깔 위배 상호작용의 단면적과 갈래비의 예측 상한값을 신뢰도 95%에서 설정했다.

Acknowledgement

I would like to acknowledge and express gratitude to my advisor Tae Jeong Kim. His delicate advice and guidance led me to complete my master's degree successfully. In the fall of 2018, I came into the lab as an undergraduate researcher and learned a lot about particle physics experiments under the guidance of my professor for about 4 years.

Also, I would like to thank Professors Hang Bae Kim and Byung Gu Cheon, the thesis committees, for helping me complete the master's degree. I want to thank Professor Su Yong Choi, Korea University, who has participated in this analysis and provided valuable comments. I would like to express my gratitude to the professors and researchers of the Korea CMS Group, who gave me the opportunity to consistently present the analysis status and receive feedback during the research process. I would like to thank Soo Hyun Yoon, Ece Asilar, Yeon Su Ryou, Jieun Choi, and Juhee Song for their direct assistance in conducting this research in the laboratory.

Declaration of Ethical Conduct in Research

I, as a graduate student of Hanyang University, hereby declare that I have abided by the following Code of Research Ethics while writing this dissertation thesis, during my degree program.

"First, I have strived to be honest in my conduct, to produce valid and reliable research conforming with the guidance of my thesis supervisor, and I affirm that my thesis contains honest, fair and reasonable conclusions based on my own careful research under the guidance of my thesis supervisor.

Second, I have not committed any acts that may discredit or damage the credibility of my research. These include, but are not limited to : falsification, distortion of research findings or plagiarism.

Third, I need to go through with Copykiller Program(Internet-based Plagiarism-prevention service) before submitting a thesis."

JUNE 12, 2022

Degree : Master

Department : DEPARTMENT OF PHYSICS

Thesis Supervisor : KIM TAE JEONG

Name : Lim Jongwon


(Signature)

연구 윤리 서약서

본인은 한양대학교 대학원생으로서 이 학위논문 작성 과정에서 다음과 같이 연구 윤리의 기본 원칙을 준수하였음을 서약합니다.

첫째, 지도교수의 지도를 받아 정직하고 엄정한 연구를 수행하여 학위논문을 작성한다.

둘째, 논문 작성시 위조, 변조, 표절 등 학문적 진실성을 훼손하는 어떤 연구 부정행위도 하지 않는다.

셋째, 논문 작성시 논문유사도 검증시스템 "카피킬러"등을 거쳐야 한다.

2022년06월12일

학위명 : 석사

학과 : 물리학과

지도교수 : 김태정

성명 : 임종원



한 양 대 학 교 대 학 원 장 귀 하